PRECISION ROTATION SENSING USING ATOM INTERFEROMETRY

A DISSERTATION
SUBMITTED TO THE DEPARTMENT OF PHYSICS
AND THE COMMITTEE ON GRADUATE STUDIES
OF STANFORD UNIVERSITY
IN PARTIAL FULFILLMENT OF THE REQUIREMENTS
FOR THE DEGREE OF
DOCTOR OF PHILOSOPHY

Todd Lyndell Gustavson
February 2000

I certify that I have read this dissertation and that in my opinion it is fully adequate, in scope and quality, as a dissertation for the degree of Doctor of Philosophy.
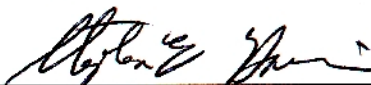
Mark Kasevich
(Principal Adviser)

I certify that I have read this dissertation and that in my opinion it is fully adequate, in scope and quality, as a dissertation for the degree of Doctor of Philosophy.

Steven Chu
(Physics and Applied Physics)

I certify that I have read this dissertation and that in my opinion it is fully adequate, in scope and quality, as a dissertation for the degree of Doctor of Philosophy.

Stephen Harris
(Applied Physics and Electrical Engineering)

Approved for the University Committee on Graduate Studies:

iii

Abstract

A rotation-rate sensor was developed using atom interferometry and the Sagnac effect for matter waves. This device has a short-term sensitivity of 6×10^{-10} rad/sec for a 1 second integration time, which is the best publicly reported value to date. It has high intrinsic accuracy because it relies on interactions between atoms and laser light that is stabilized to an atomic transition. Long-term stability is promising and characterization is currently underway. Potential applications include inertial navigation, geophysical studies, and general relativity tests such as verification of the Lense-Thirring and geodetic effects.

The principle of operation is as follows: A thermal cesium atomic beam crosses three laser interaction regions where two-photon stimulated Raman transitions between cesium ground states transfer momentum to atoms and divide, deflect, and recombine the atomic wavepackets. Rotation induces a phase shift between the two possible trajectories and causes a change in the detected number of atoms with a particular internal state. Counterpropagating atomic beams form two interferometers using shared lasers for common-mode rejection, and the rotation phase shifts have opposite sign since the phase shift is proportional to the vector velocity of the atoms. Therefore, subtracting or adding the interferometer signals discriminates between rotation and transverse acceleration summed with laser arbitrary phase. Furthermore, in the inertial reference frame of the atoms, rotations Doppler-shift the Raman lasers. Adding Raman frequency shifts to cancel these Doppler-shifts allows operation at an effective zero rotation rate, improving sensitivity and bandwidth. Modulating these frequency shifts facilitates sensitive lock-in detection readout techniques.

Acknowledgments

I am indebted to my adviser, Mark Kasevich, for the invaluable guidance, wisdom, and suggestions that he has generously provided over the course of this work. I am fortunate to have worked with Arnaud Landragin during his recent postdoc and appreciate his help and insights. My thanks also to Philippe Bouyer for his contributions during his postdoc in the formative years of the experiment. I also thank the following people who contributed to the gyroscope project: Dallin Durfee has smoothly taken over running the experiment during the writing of this thesis. Adam Hecht helped with characterizing long-term stability. Quentin Besnard was a visiting student who calculated the interferometer phase shifts for experimentally interesting cases. Aaron Noble was responsible for the design and construction of the initial vacuum system and setting up several diode laser assemblies. Frédéric Bouyer and Elsa Joo were visiting students who calculated the effect of Raman laser misalignments and multiple photon transitions, respectively. Funding for this work has been provided by NASA, ONR, NIST, and the NSF. I particularly acknowledge my colleagues, Brian Anderson, Jeff McGuirk, and Mike Snadden, who helped make my stay in New Haven very enjoyable after we moved with Mark in July 1997 upon Mark's accepting a position at Yale. I worked with Brian on a lithium apparatus during my first year at Stanford, and I am grateful to him for his assistance and camaraderie since then. I also acknowledge my Stanford colleagues for many helpful discussions, particularly Heun-Jin Lee, Achim Peters, Kengyeow Chung, Brent Young, and Joel Hensley. I thank Wolfgang Jung for instruction in the machine shop, and Ken Sherwin for his frequent assistance. My thanks to Kurt Gibble at Yale for his helpful suggestions. Finally, I am thankful for the support of my parents, sister, and grandparents.

Contents

List of Tables

List of Figures

Chapter 1

Introduction

1.1 Rotation measurements

A gyroscope is an instrument that can be used to measure rotation relative to an inertial reference frame. This dissertation describes a gyroscope with unprecedented sensitivity that is based on atom interferometry. Such devices may be useful for navigation, geophysics, and general relativity. These applications are briefly described below and discussed in detail in Chapter 2.

For inertial navigation, one must continually monitor angular orientation and accelerations to calculate the current position relative to a known starting point, without reference to external landmarks such as coastlines, the horizon, or celestial observations. Navigation by dead reckoning requires accurate gyroscopes and accelerometers, as small measurement errors quickly become large position errors.

Geophysicists are interested in precise rotation sensors for studying rotational motion of tectonic plates during seismic events. In addition, improved models of the Earth's composition and dynamics may result from studying variations in the Earth's rotation rate, which are on the order of $\sim 10^{-8} \Omega_{\mathrm{E}}$ on time-scales of a few days. Here $\Omega_E \simeq 7.292 \times 10^{-5}$ is the rotation rate of the Earth about its axis.[1]

---

[1]When calculating Ω_E, we must include the effect of the Earth's motion around the sun, namely that the Earth rotates slightly more than 2π in 24 hours. The sidereal day is the time for the Earth to rotate by 2π, and is equal to 23 hours, 56 minutes, and 4.1 sec.

In general relativity, gyroscopes are important because they may provide a means to explore subtleties in the curvature of space-time near a massive rotating body such as the Earth. In particular, the work of Lense and Thirring [1, 2] indicates that a gyroscope in the gravitational field of a rotating massive body will experience a precession relative to a frame defined by the distant stars. An experiment to measure the Lense-Thirring effect, or dragging of inertial frames, could prove to be one of only a few tests of general relativity that are within experimentally achievable limits.

Many different gyroscope mechanisms have been devised, and below we will distinguish between the two primary styles of gyroscopes: mechanical gyroscopes based on inertia or resonance effects, and interferometric devices based on the Sagnac effect. For a review of both types of instruments, excluding atom interferometers, see [3].

1.1.1   Mechanical gyroscopes

The first gyroscope was invented in 1852 by the French physicist Foucault as an extension of his work one year earlier when he used a pendulum to demonstrate the Earth's rotation. Mechanical gyroscopes like Foucault's use a mass spinning rapidly with its angular momentum vector along its axis of symmetry, and conservation of angular momentum keeps the direction of the rotation axis constant in the absence of applied torques. Low friction gimbal mounts with one or more degrees of freedom are typically used to support the gyroscope against gravity and attach it to a support platform such as an aircraft bulkhead. The gyro's large angular momentum greatly increases its immunity to unwanted perturbations.

Depending on the design, the gyroscope may be intrinsically sensitive to either angular displacements or to rotation rates. (Our atom-interferometer measures rotation rates, as will be seen in section 1.1.2.) For example, to use a gyro for measuring angular displacements, one could simply measure the angle between the gyro rotation axis and the support platform. A rate gyro might add a spring so angular displacement is proportional to angular velocity. Or, electrical windings could be used as a magnetic pickup coil such that the gyroscope is only sensitive to changes in angle, analogous to a generator.

One axis or single degree of freedom gyroscopes have been carefully optimized during their widespread use in the aerospace industry for the past several decades, particularly since World War II. Nonetheless, they are mechanical devices with moving parts and are subject to calibration changes due to wear, temperature, etc. Acceleration may cross-couple into rotation if the force is not transmitted exactly to the center of mass, or because of flexing of the mounting hardware. Mechanical gyros in field use are typically compensated for various systematic effects based on detailed modeling done at a test lab.

1.1.2 Sagnac effect gyroscopes

The Sagnac effect was originally conceived as a rotation dependent phase shift in an optical interferometer [4]. We briefly describe the Sagnac effect below, and a similar treatment is given in [5]. To understand the basic idea of the Sagnac effect, imagine a loop of fiber with radius r rotating with angular velocity Ω about an axis that is perpendicular to the plane of the loop and passing through its center, as shown in Fig. 1.1a. Suppose light is coupled into the fiber in both directions using a beamsplitter at point B. Now consider the time required for light traveling along the clockwise and counter-clockwise paths to reach a detector at point D (the point on the loop instantaneously opposite point B). If the loop were not rotating, the times would be the same, by symmetry. For a rotating loop, light traveling opposite the rotation direction will arrive first (at time t_1), because the detector is moving toward the propagating light, shortening the path that the light must travel to reach the detector. Conversely, light traveling in the direction of rotation will arrive later (at time t_2) because the detector is moving away from the propagating light, lengthening the path the light must travel. A similar argument holds for a loop traversed by massive particles. For a photon or particle moving with velocity v around a loop with radius r and angular velocity Ω, the times to traverse the loop are given by:

$$
\begin{aligned}
vt_1 &= \pi r - \Omega r t_1 \\
vt_2 &= \pi r + \Omega r t_2 \,,
\end{aligned}
\tag{1.1}
$$
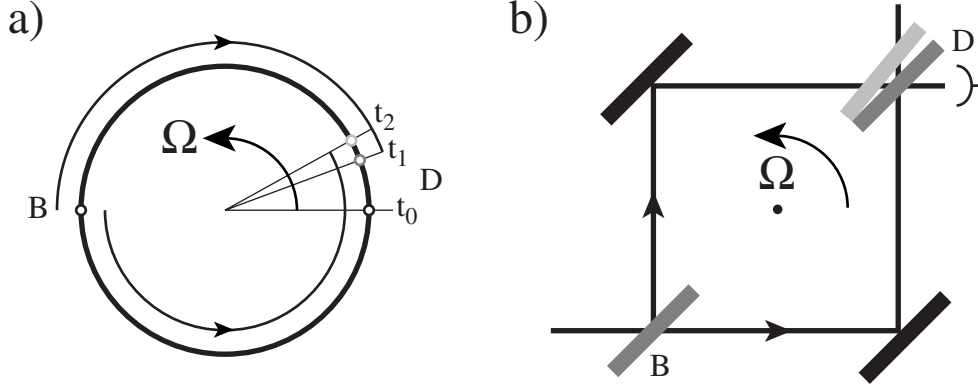
Figure 1.1: The Sagnac effect. The phase shift can be written in a general form as: $\Delta\Phi = \dfrac{4\pi\boldsymbol{\Omega}\cdot\boldsymbol{A}}{\lambda v}$ a) Particles leaving a beamsplitter at B and traversing a loop in opposite directions until detection at D (moving with the loop) at times t_1 and t_2 depending on the direction of travel. b) Here the Sagnac effect is illustrated using a Mach-Zehnder type interferometer (analogous to our interferometer configuration). The optics shown in gray are beamsplitters. For clarity, only the motion of the final beamsplitter has been shown (in light gray).

leading to a time difference of:

$$\Delta t = t_2 - t_1 \simeq \frac{2\boldsymbol{\Omega}\cdot\boldsymbol{A}}{v^2}, \tag{1.2}$$

where $\boldsymbol{A}$ is the area enclosed by the loop.[2] Using the usual relationship between phase and time, $\phi = \omega t$, we can write the phase shift between the two paths as:

$$\Delta\Phi = \frac{4\pi\boldsymbol{\Omega}\cdot\boldsymbol{A}}{\lambda v}. \tag{1.3}$$

Here λ is the wavelength, which for a massive particle is the de Broglie wavelength $\lambda_{dB} = h/mv$ (h is Planck's constant and m is the mass of the particle). The phase shift depends on the enclosed area $\boldsymbol{A}$ of the loop but is independent of its shape. Another example is shown in Fig. 1.1b, which illustrates the Sagnac effect for a Mach-Zehnder interferometer analogous to our atom interferometer configuration.

---

[2]This expression is valid for small rotation rates such that $r\Omega \ll v$.

For massive particles, Equation 1.3 is more commonly written as

$$\Delta\Phi = \frac{2m\mathbf{\Omega} \cdot \mathbf{A}}{\hbar} \, . \tag{1.4}$$

Note that Equations 1.3 and 1.4 are for a half-circuit around a loop, and therefore the phase shift is half that of the full loop geometry originally considered by Sagnac. Gyroscopes based on the Sagnac effect are rate gyros, since the phase shift is proportional to the rotation rate Ω, which has units of rad/sec. The atom interferometer phase shift will be discussed in detail in Chapter 4.

Comparing the phase shifts between light-based and atom-based interferometers with the same area, one finds that the ratio of the phase shifts scales with the energies of the interfering particles and is equal to $mc^2/\hbar\omega$. The phase shift for cesium atoms is 6×10^{10} larger than the phase shift for a HeNe laser, motivating the atom interferometry approach described here. However, the atom interferometer's advantage in intrinsic sensitivity is diminished by the much larger areas currently achievable with a light-based interferometer. This is because better beamsplitters are available for light than for atoms, and high finesse mirrors in a ring-laser gyro or multiple fiber turns in a fiber-optic gyro can increase the effective area. Eventually, advances in atom optics are likely to result in much larger enclosed areas for atom interferometers. A specific comparison between an active ring-laser gyro and our atom interferometer is presented in section 2.4.

1.2 History of laser manipulation of atoms

For atom interferometry to be a viable approach to inertial sensing, we require bright sources of atoms and methods to manipulate atoms in ways that are analogous to the optics used for light. In fact, various methods have been developed for cooling and manipulating neutral atoms using lasers, and many advances have been made in this area in recent years. Of particular importance are techniques for cooling atoms to achieve brighter atomic sources and development of atom optics elements such as beamsplitters and mirrors with which to form an interferometer. A brief and

necessarily incomplete history of some of these developments that are relevant to our gyroscope experiment follows. For a more general history of atomic physics, see [6].

1.2.1 Laser cooling

Laser cooling of neutral atoms[3] was originally proposed in 1975 by Hänsch and Schawlow [8]. Doppler cooling was first achieved by Chu *et al.* in 1985 [9], who cooled a gas of neutral sodium atoms to ~ 240 μK, the theoretical minimum for pure Doppler cooling. An experiment by Phillips *et al.* measured a temperature of ~ 43 μK, lower than the Doppler limit [10], and this lower temperature was soon confirmed by Chu *et al.* This led to further theoretical investigation, and Cohen-Tannoudji and Chu independently developed models that explained the sub-Doppler cooling mechanisms in terms of polarization gradients [11, 12]. Tight confinement of atoms in a trap was achieved by Chu and Pritchard *et al.* [13] in 1987 by adding appropriate magnetic field gradients in conjunction with 3-D Doppler cooling, called a magneto-optical trap (MOT). For their advances in laser cooling and trapping, Chu, Cohen-Tannoudji, and Phillips were awarded the 1997 Nobel Prize in physics.

1.2.2 Atom interferometry

Ramsey demonstrated atom interference in 1950 using the method of separated oscillatory fields with rf transitions and an atomic beam source [14], establishing many important principles for experiments to come. However, because the rf photons give a small momentum kick, there is little spatial separation between the arms of the interferometer, and therefore low sensitivity to inertial effects. Neutron interferometer measurements of gravitational acceleration and the Earth's rotation were made in the 1970's [15, 16], utilizing Bragg diffraction off crystal planes of single-crystal silicon for beamsplitters. The idea to use neutral atom interferometry for inertial measurements and gravity gradient detection was first proposed by Altshuler and Frantz in

---

[3]Laser cooling of ions was proposed independently by Wineland and by Dehmelt in 1975 [7], and each demonstrated this in 1978.

1973 [17]. Clauser, in 1988, proposed several possible atom interferometer configurations for inertial measurements [18]. Also in 1988, Pritchard *et al.* developed laser beamsplitters appropriate for atom interferometry experiments, and demonstrated Bragg scattering of atoms from a standing wave [19]. The first atom interferometers with separated spatial trajectories were demonstrated in 1991 by four groups with quite different approaches: a Young's double-slit experiment [20], a Mach-Zehnder interferometer using three nanofabricated mechanical gratings [21], a Sagnac effect measurement using optical excitation with four traveling waves (the Ramsey-Bordé geometry) [22], and a gravity measurement using stimulated two-photon Raman transitions with three laser pulses in a $\frac{\pi}{2} - \pi - \frac{\pi}{2}$ configuration [23, 24].

Since these first experiments, a number of atom interferometers have been developed. A few experiments of particular interest to this work are listed below, and a review of many topics in the field can be found in [25]. Atom interferometry has been used for a precision measurement of $\hbar/m$ for cesium, yielding the fine structure constant α [26, 27]. An experiment directly comparing absolute gravitational acceleration measurements made with an atom interferometer (atom as proof mass) versus with an optical interferometer (falling corner-cube as proof mass) is described in [28, 29]. A gravity gradiometer has also been developed [30].

1.2.3 Bose-Einstein condensation and atom-lasers

Bose-Einstein condensation (BEC) occurs when many particles with integer spin (bosons) are cooled until they occupy the same ground state in a potential well. BEC in a dilute gas was achieved in 1995 using rf-assisted evaporative cooling, achieved first with rubidium [31], then followed shortly by condensation in lithium [32, 33], and sodium [34]. For a review of BEC, see, for example, [35]. Research in this field has been progressing at an extremely rapid pace, and notably for the present experiment, techniques have been developed to extract atoms from the BEC, forming a coherent source of atoms analogous to a laser. Various atom-laser configurations have been demonstrated; for example, pulsed [36], mode-locked [37], and quasi-continuous [38]. Atom-lasers can potentially provide extremely bright sources of coherent atoms, and

they will undoubtedly play an important role in future interferometry experiments.

1.3   Overview of this dissertation

Chapter 2 discusses applications for sensitive gyroscopes and compares the performance of our apparatus with that of various other instruments. Chapter 3 reviews the principal methods of manipulating atoms with lasers used in this experiment. This includes techniques used for transverse cooling of the atomic beam, state preparation, detection, and Raman transitions used to construct the interferometer. Chapter 4 discusses atom interferometry theory, outlines the calculation and interpretation of the Sagnac phase shift, and presents a theoretical model of the gyroscope signal for our experiment. Chapter 5 contains a detailed description of the experimental apparatus. Chapter 6 first presents the most fundamental interferometry results and then describes refinements to the apparatus, such as dual atomic beams, Raman beam detuning control, and data acquisition techniques. Chapter 7 discusses noise, systematic errors, and long-term performance of the instrument. A few modifications to the apparatus to improve long-term stability are described here as well. Chapter 8 summarizes the current status of the experiment and discusses the outlook for the future.

Chapter 2

Applications

This chapter gives an overview of three applications for high precision gyroscopes, and compares the current state-of-the-art performance of various types of gyroscopes.

2.1 Inertial navigation

Inertial navigation requires monitoring rotation and acceleration sensor data over time to compute current position relative to a known starting point, and has important practical applications for a variety of platforms. These include: aircraft (for attitude control, flying during poor visibility conditions, and to supplement radio beacons and the Global Positioning System, hereafter GPS), submarines (covert operation may preclude use of external references), rockets, ships, autonomous vehicles, oil-well drilling, and automobiles. For many navigation applications, cost and size issues may take precedence over ultimate performance. However, the cost and size of atom interferometers are likely to decrease rapidly as new techniques are developed.

In general, an inertial navigation system needs three accelerometers and three gyroscopes – one for each axis. The accelerometers can be integrated to determine velocity and, in the absence of other accelerations, they can be used to determine tilt based on the projection of gravitational acceleration onto each axis. However, a nearby mountain could change the local gravitational acceleration direction slightly and lead to an error. Corrections can be made for these errors if gravity gradients

are measured to determine components of the gravitational field curvature tensor. In fact, gravity maps of some areas have been made for navigational purposes, and a robust, sensitive gradiometer that could be used from an aircraft would benefit this endeavor. See section 8.3.3 for a discussion of a possible atom interferometer configuration similar to the gyroscope apparatus described in this work that would have a two axis readout for rotation, acceleration, and gravity gradient measurements.

GPS consists of a constellation of 24 satellites carrying atomic clocks. Each satellite broadcasts a unique sequence of data, and a receiver can determine its position from the relative phase of the packets and the known satellite positions, which are also broadcast. Standard GPS can determine position to within a few meters, though this accuracy is typically degraded for civilian use to as much as 100 m by military "selective ability." More sophisticated receivers achieve better accuracy by utilizing an additional frequency band, which is also broadcast by the satellites. Differential GPS can measure position relative to a local transmitter to < 1 cm. GPS receivers are not sensitive to angular orientation or rotation rate, so gyroscopes are still required for many applications. The primary GPS transmission frequency is ~ 1.6 GHz, and the signals are weak enough that use under heavy tree-cover is problematic, and therefore it is generally unusable indoors, underwater (submarines), underground (drilling or tunneling), etc. Furthermore, the military considers GPS to be vulnerable because the signals could be easily jammed. Therefore, there is a demand for other types of devices to supplement GPS for navigation systems.

Accelerometers and gyroscopes must be extremely accurate if good position accuracy is to be maintained over long periods of time. However, in many cases, occasional position fixes can be obtained independently (for example, with GPS), reducing the problem of drift. A small accelerometer bias error of Δa (meaning that with no acceleration, the accelerometer falsely reads Δa) leads to a position error that is quadratic in elapsed time T, namely $\frac{1}{2}\Delta a T^2$. A constant offset in heading angle $\Delta\theta$ leads to a position error approximately equal to $\Delta\theta v T$, increasing linearly with time and velocity. A rotation rate bias error $\Delta\Omega$ causes a heading angle error $\Delta\theta = \Delta\Omega T$, and a position error of approximately $\Delta\Omega v T^2$.

2.1.1 Gyroscope units

We typically refer to our gyroscope sensitivity in units of $(\text{rad/sec})/\sqrt{\text{Hz}}$. These units signify a rotation rate (rad/sec) measurement that is presumed to be limited by shot-noise. Shot-noise processes obey Poisson statistics with standard deviation equal to $\sqrt{N}$ of the number of particles, and the total number of particles in the signal increases linearly with time. Therefore, a shot-noise-limited signal improves like $\sqrt{t}$ with integration time t. Dividing by $\sqrt{\text{Hz}}$ normalizes the result by the measurement bandwidth, yielding the sensitivity in 1 second. To find the minimum rotation rate measurable (rotation rate sensitivity) achievable after 1 hr of integration, one divides $(\text{rad/sec})/\sqrt{\text{Hz}}$ by $\sqrt{3600 \text{ sec}}$. Rate gyroscopes (such as our device) have white noise spectral density $(\Delta\Omega)$ if shot-noise-limited, and exhibit a random walk in angle that diverges like $\Delta\Omega\sqrt{t}$. The units are often given in $\text{deg}/\sqrt{\text{hr}}$ or equivalently, in $(\text{rad/sec})/\sqrt{\text{Hz}}$, which can be interpreted as the angle random walk in 1 second. As an example, to convert from a gyroscope sensitivity of 6×10^{-10} $(\text{rad/sec})/\sqrt{\text{Hz}}$ to $\text{deg}/\sqrt{\text{hr}}$, one should multiply by $\sqrt{3600\frac{\text{sec}}{\text{hr}} \times \frac{180}{\pi}\frac{\text{deg}}{\text{rad}}}$, yielding 2×10^{-6} $\text{deg}/\sqrt{\text{hr}}$.

2.2 Geophysics

Length of day fluctuations

The Earth rotation rate and the length-of-day (LOD) fluctuate over time on the order of a few parts in 10^8. The main mechanism responsible for the fluctuations is oceanic tidal angular momentum. Solar and lunar tides change the mass distribution of the oceans and, to conserve angular momentum, the Earth rotation rate changes accordingly [39, 40]. The tides also induce circulating water currents, which similarly affect the Earth rotation rate. Since the tidal bulge lags slightly, tidal forces apply torque, directly changing the Earth rotation rate; however, Lambeck [41] claims this effect is much smaller, at only 7×10^{-22} rad/sec^2 ($3 \times 10^{-8}\Omega_E$/century, accounting for most of the total slowing of the Earth rotation rate). The variations in UT1, the name for the clock defined by the spinning Earth, can be measured quite accurately by very long baseline interferometry (VLBI), as shown in Fig. 2.1. Fluctuations
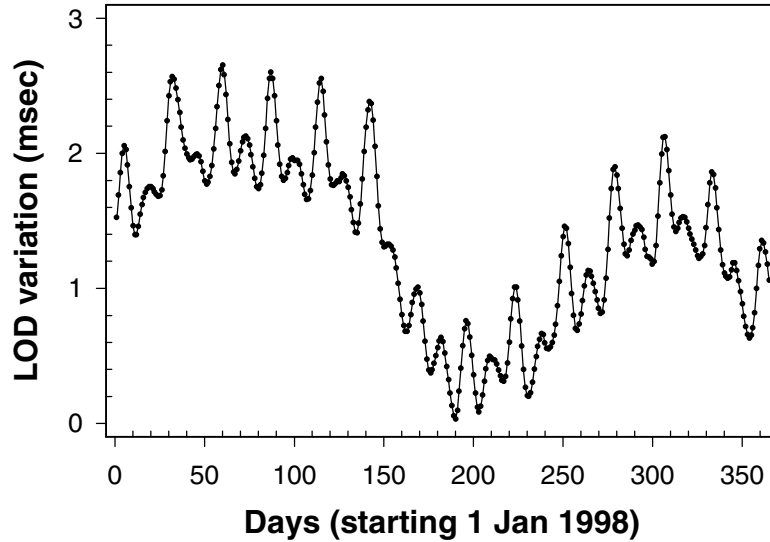
Figure 2.1: Length-of-day variation as measured by VLBI. Each point represents 1 day. The peak-to-peak (semi-annual) fluctuation shown corresponds to $\sim 3 \times 10^{-8}\Omega_{\rm E}$. Data source: National Earth Orientation Service Bulletin (International Earth Orientation Service Bulletin A), available from the U.S. Naval Observatory.

occurring on < 1 day time scales are not shown in the figure, but twice-daily tidal effects corresponding to 100 μsec or $1.1 \times 10^{-9}\Omega_{\rm E}$ peak-to-peak variation have also been measured with VLBI [39]. Nonetheless, measurements with $< 1 \times 10^{-9}\Omega_{\rm E}$ sensitivity or < 1 hr time scales would be of interest, and are a promising application for more sensitive gyroscopes. Improved data could result in better understanding of the Earth's composition and dynamics by providing a stricter test of theoretical models [41, 42].

Seismic monitoring

Seismic events may be an important area for study with sensitive gyroscopes. Little information about the rotational spectrum of earthquakes currently exists. (See Stedman [43] for further discussion of gyroscope applications for seismic and other geophysical applications.) Gyroscopes have an advantage over VLBI for this application, because they can be used to make local measurements; for example, near a particular earthquake fault. In contrast, VLBI measures the net rotation of a large

region, is inherently non-portable, and requires complex data reduction involving collaboration among multiple international sites. The effect of earthquakes on global rotation rates is essentially negligible.

Torsion pendulum G measurements

Torsion pendulum measurements of the gravitational constant G may ultimately be limited by knowledge of local rotational noise from seismic and cultural sources [44]. Pendulum periods are typically long, in the range of 100 to 1000 seconds, and rotational noise at the oscillation frequency will give a systematic offset in the value for G. To set a scale for the angular sensitivities in torsion pendulum experiments, the deflection angle changes due to thermal noise and tilts are typically ~ 1 nrad (for 0.1 mK temperature regulation and 20 nrad rms tilts). A measurement of the rotational noise at the oscillation frequency could establish an upper limit on the systematic error, and ultimately could be used to correct the data and improve the result. Our gyroscope appears promising for measurements at this frequency and sensitivity range.

2.3   General relativity

Lense and Thirring predicted in 1918 [1, 2] that a satellite orbiting a rotating body would experience a precession of its orbit due to the rotating mass. The Lense-Thirring effect can be obtained in the limit of weak gravitational fields by considering the relativistic field equations in the linear approximation, and leads to off-diagonal terms in the metric. The effect on nearby space-time is similar to the behavior of a viscous fluid surrounding a rotating sphere, and is sometimes called the dragging of inertial frames. In 1960, Schiff published an analysis of the precession of a gyroscope that included the Lense-Thirring and geodetic precessions [45]. For a gyroscope

orbiting the earth, Schiff found a precession rate of:

$$\boldsymbol{\Omega} \;=\; \boldsymbol{\Omega}_{\text{geo}} + \boldsymbol{\Omega}_{\text{LT}} \tag{2.1}$$

$$\boldsymbol{\Omega}_{\text{geo}} \;=\; \frac{3}{2}\frac{GM}{c^2 r^3}(\boldsymbol{r} \times \boldsymbol{v}) \tag{2.2}$$

$$\boldsymbol{\Omega}_{\text{LT}} \;=\; \frac{GI}{c^2 r^3}\left[\frac{3\boldsymbol{r}}{r^2}(\boldsymbol{\omega}\cdot\boldsymbol{r}) - \boldsymbol{\omega}\right], \tag{2.3}$$

where $\boldsymbol{r}$ and $\boldsymbol{v}$ are the current position and velocity of the gyroscope; M, I, and $\boldsymbol{\omega}$ are the mass, moment of inertia, and rotation rate of the Earth. The term $\boldsymbol{\Omega}_{\text{geo}}$ is the geodetic term, and arises from parallel propagating a vector through space-time that is curved due to the mass of the Earth, independent of its rotation. The term $\boldsymbol{\Omega}_{\text{LT}}$ is the Lense-Thirring precession arising from the rotation of the Earth. For a 650 km polar orbit around the Earth, one finds $\Omega_{\text{geo}} = 6.6$ arcsec/yr $= 1 \times 10^{-12}$ rad/sec, and $\Omega_{\text{LT}} = 44$ marcsec/yr $= 6.45 \times 10^{-15}$ rad/sec. For a ground-based test, the geodetic effect is reduced to 0.4 arcsec/yr.

A good introduction to general relativity and the Lense-Thirring and geodetic effects in particular is given by Ohanian and Ruffini [46]. For a more exhaustive description, see Misner, Thorne and Wheeler [47]. Bordé *et al.* [48] have done a general relativistic calculation for a matter-wave interferometer in which they have obtained the usual Sagnac and Lense-Thirring effects.

Schiff's work led to the Stanford/NASA Gravity Probe B (GPB) collaboration [49], which is planning a satellite gyroscope test designed to measure the geodetic effect to 1 part in 10^4 and the Lense-Thirring effect to within 2%. This experiment is based on precision spinning superconducting spheres in a cryogenic environment within a drag-free satellite gyroscope system and is scheduled for launch in Fall 2000. Note that torques due to tidal effects vanish for a sphere.

The Lense-Thirring effect has recently been measured in the LAGEOS experiment by Ciufolini *et al.* [50], yielding a result of 1.1 ± 0.2 vs 1.0 predicted by general relativity. This measurement used laser ranging to monitor the orbital parameters of two satellites in polar orbits, and data reduction required detailed modeling of the Earth's mass distribution and gravitational field. The Lense-Thirring effect shifts

the satellite orbit by 2 m/yr or an angle of 31 marcsec/yr, while the quadrupole gravitational field of the Earth shifts the orbit by 45 marcsec/yr. Nonetheless, a three percent measurement may be possible using the LARES satellite [51].

Verification of either the Lense-Thirring or geodetic effects provides an important test of gravitational theory since neither effect can be explained by a simple extension of special relativity or the equivalence principle. Very few tests of general relativity are currently experimentally accessible, therefore a successful gyroscope precession experiment has particular significance. See Will [52] for a discussion of the current experimental foundations of general relativity. Furthermore, verification of these effects with an atom interferometer gyroscope would still be of interest. Such a test would demonstrate that the precession is due to a property of the reference frame and not due to details of the gyroscope construction or its spin. (However, the precession rate is often derived using a spinning gyroscope for conceptual convenience.) Because the atom gyro sensitivity scales like the squared length of the apparatus (L^2), a ground-based test might be feasible [53]. Many technical challenges would need to be overcome, for example the problem of accurately determining the gyroscope orientation relative to the distant stars, despite atmospheric perturbations. In addition, a Sagnac gyroscope might be used to explore the connection between quantum mechanics and gravity as well as topological phase shifts such as the analog of the Aharonov-Bohm effect [54] with gravitational fields.

2.4 Gyroscope performance comparison

Table 2.1 summarizes the performance of our instrument compared to some competing technologies. Note that numbers quoted reflect performance achieved to date and do not necessarily reflect the fundamental limits of particular technologies. For the acceleration comparison, it should be noted that the fountain has much better accuracy than our device, since it uses a single beam of light pulsed in the time domain, whereas in our case, dimensional stability must be maintained between the three light beams in the interferometer region since arbitrary-phase drift is not easily distinguished from acceleration. For information about a variety of types of gyroscopes

Rotation	Short term sensitivity $(\text{rad/sec})/\sqrt{\text{Hz}}$	Comparison
This work (S/N=33,000)	$\mathbf{6 \times 10^{-10}}$ $(8 \times 10^{-6}\Omega_E/\sqrt{\text{Hz}})$	1
Ring laser gyro (1 m^2) [43, 55]	1.3×10^{-9}	2.2
Superfluid helium [56, 57]	2×10^{-7}	333
Fiber optic gyro (commercial) [3]	$\sim 3 \times 10^{-7}$	500
Nanofabricated gratings [58]	3.6×10^{-6}	6000
Moiré classical fringes [59]	3.6×10^{-5}	60000
Acceleration	**Short term sensitivity** $g/\sqrt{\text{Hz}}$	**Comparison**
This work (estimated)	$\mathbf{3.5 \times 10^{-8}}$	1
Atomic fountain [60, 28]	2.3×10^{-8}	0.66

Table 2.1: Gyroscope performance comparison.

and accelerometers including many not mentioned here, see [3]. Though the electro-statically levitated gyro (ESG) is often used in high performance inertial guidance systems, performance figures are classified and therefore unavailable. See [43, 3, 61] to review ring laser and fiber optic gyros. The Sagnac effect has also been demonstrated with electrons [62].

2.4.1   Ring-laser gyro

Since the ring-laser gyroscope (RLG) is currently the best performing type of optical gyro, we will briefly discuss how its short-term sensitivity may be estimated. The active ring-laser gyro consists of a high Q optical cavity containing a helium-neon laser gain medium. Lasing occurs in both directions around the loop, but must satisfy the boundary condition that the path length be divisible by an integral number of

wavelengths. Stedman shows in [43] that the difference in path lengths due to the Sagnac effect (presented here in section 1.1.2) causes a frequency splitting between the counterpropagating modes equal to:

$$\delta f = \frac{4\boldsymbol{A} \cdot \boldsymbol{\Omega}}{\lambda P},$$ (2.4)

where P is the perimeter of the ring. Stedman gives the short-term rotation rate sensitivity as:

$$\Delta \Omega = \frac{cP}{4AQ} \sqrt{\frac{hf_0}{P_o T}},$$ (2.5)

where $\Delta \Omega$ has units of rad/sec (minimum detectable for T sec integration), Q is the quality factor of the cavity, and P_o is the total output power. (The Q factor arises in expressing the shot-noise limited determination of $\delta f / f_0$.) Note that optical gyros must be biased to a non-zero rotation rate (for example, with a mechanical dither) or light back-scatter can cause the modes to lock together. This is potentially a significant advantage for atom interferometers over the RLG.

As a specific example, consider Stedman's active ring-laser, C_{II}, with the following characteristics (as of 1997): $P_o = 400$ pW, $Q = 3 \times 10^{12}$, $A = 1$ m^2, and $P = 4$ m. With these numbers, Equation 2.5 gives a short-term rotation rate sensitivity of $\Delta \Omega = 3 \times 10^{-9}$ (rad/sec)/$\sqrt{\mathrm{Hz}}$, which has since been improved to 1.3×10^{-9} (rad/sec)/$\sqrt{\mathrm{Hz}}$. Note that RLGs used for inertial navigation (for example, in aircraft) have $A < 0.02$ m^2 and have correspondingly worse performance than this large research instrument.

2.4.2 Gravity Probe B

It is interesting to compare the performance of our gyroscope with GPB. Because the superconducting London moment readout used in GPB is sensitive to the angle of orientation between the spinning sphere and the readout loop, it is intrinsically sensitive to rotation angles, whereas a Sagnac gyroscope is intrinsically sensitive to rotation rates. Since the GPB readout is expected to be limited by electrical current
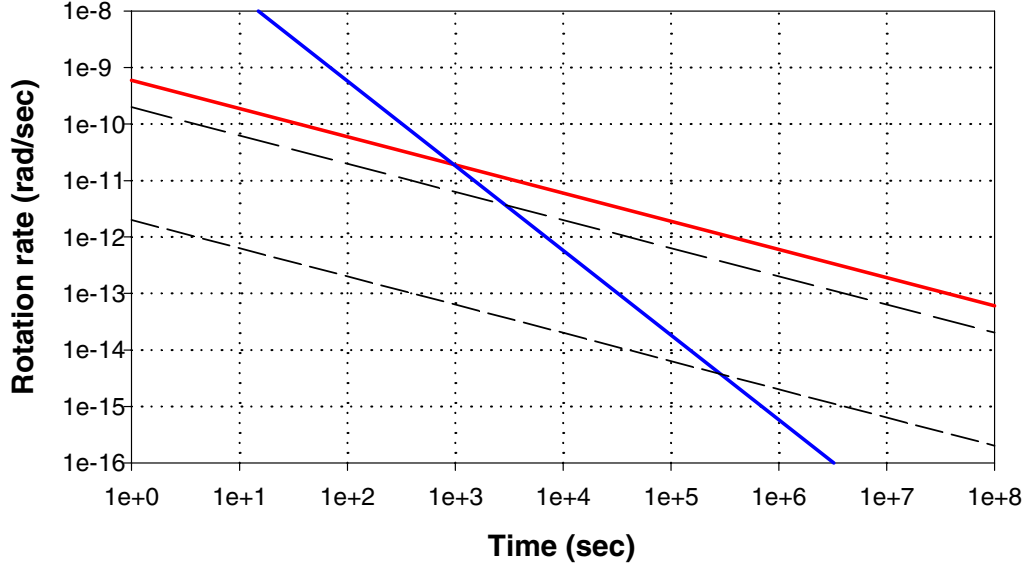
Figure 2.2: Sensitivity scaling relative to Gravity Probe B. GPB rotation rate measurement (steepest slope) improves as $t^{\frac{3}{2}}$, whereas the atom interferometer gyro rotation rate measurement (solid) should improve as $t^{\frac{1}{2}}$. The dashed lines denote the shot-noise limit expected for our current apparatus, and the anticipated performance if the apparatus were scaled to 20 m length.

shot-noise in the super-conducting quantum interference device (SQUID) used for the readout, its ability to determine angle improves like $t^{\frac{1}{2}}$. However, if the instrument is used to measure a constant rotation rate, then the angular displacement increases linearly with time. This leads to a rotation rate measurement that improves like $t^{\frac{3}{2}}$ for GPB, in contrast to the $t^{\frac{1}{2}}$ scaling of a shot-noise-limited Sagnac gyroscope. This scaling behavior is shown graphically in Fig. 2.2. To get a feeling for the different scaling with time, consider the following example. GPB has an expected sensitivity of 1 marcsec (4.85×10^{-9} rad) in a 4 hour integration [63]. That implies an angle measurement of 5.8×10^{-7} rad in 1 sec (or $\simeq 5.8 \times 10^{-7}$ rad/sec), which is 970 times worse than our atom interferometer gyro, but in 4 hours, GPB achieves 3.4×10^{-13} rad/sec, which is 15 times better than the scaled atom interferometer performance. Note that our apparatus is currently a factor of ~ 3 from the shot-noise limit, and long-term drifts prevent us from integrating for the extreme times shown in Fig. 2.2. GPB is anticipated to have outstanding long term drift rates of 8×10^{-18} rad/sec.

Chapter 3

Laser manipulation of atoms

The goal of this chapter is to describe the most important principles of laser cooling and laser manipulation of atoms that have been used in this experiment. The abridged treatment given here attempts to outline the relevant theory, summarize the primary results, and cite references where the full derivations can be found. A good introduction to these topics can be found in the textbook *Laser Cooling and Trapping*, by Metcalf and van der Straten [64].

3.1 Two-level atoms

We will exclusively make use of the cesium D_2 transition between the $6S_{1/2}$ and $6P_{3/2}$ manifolds. There are two ground states corresponding to $6S_{1/2}$, labeled $F = 3$ and $F = 4$. $F = I + J$ is the total angular momentum, the sum of nuclear angular momentum $I = 7/2$ and the electron angular momentum $J = L + S$ including orbital angular momentum and spin. The $6P_{3/2}$ excited states include levels $F' = 2$, $F' = 3$, $F' = 4$, and $F' = 5$, where the prime denotes an excited state. Each F level has $2F+1$ Zeeman m_F sublevels, with degeneracy broken by the presence of a magnetic field. For a review of atomic structure, see [65] and [66, ch. 2]. Despite the large number of levels, the frequency spacings between energy levels and polarization dependent selection rules are such that only two levels need be considered in some cases. For example, the $F = 4 \rightarrow F' = 5$ transition is called a *closed* or *cycling* transition because an

atom excited to the $F' = 5$ state is prohibited by selection rules from decaying to anything other than the $F = 4$ state, where it can undergo another cycle. This cycling transition is used for cooling and detection, and can be approximated as a two-level system. More specifically, circular polarization is used, which means that atoms cycle between the $F = 4, m_F = \pm 4$ and $F' = 5, m_F = \pm 5$ states.

We will consider a stationary two-level atom in an electromagnetic field to illustrate the important concepts of Rabi oscillations and ac Stark shifts. Spontaneous emission is neglected and the light is treated as a classical field. The Hamiltonian for this system can be written as:

$$\hat{H} = \hbar\omega_e \, |e\rangle \, \langle e| + \hbar\omega_g \, |g\rangle \, \langle g| - \boldsymbol{d} \cdot \boldsymbol{E} \,. \tag{3.1}$$

The final term is the interaction between the atom and the light, where $\boldsymbol{d} = e\boldsymbol{r}$ is the dipole moment operator (electron charge times displacement from the nucleus) and

$$\boldsymbol{E} = \boldsymbol{E}_0 \cos(\omega t + \phi) \tag{3.2}$$

represents the electric field. The matrix element of the interaction term can be written in terms of the Rabi frequency, Ω_{eg}:

$$\Omega_{eg} \equiv -\frac{\langle e| \, \boldsymbol{d} \cdot \boldsymbol{E} \, |g\rangle}{\hbar} \,, \tag{3.3}$$

which is the frequency of oscillation between the ground and excited state for light tuned to resonance.

One must solve the Schrödinger equation,

$$i\hbar \frac{\partial}{\partial t} \, |\Psi\rangle = \hat{H} \, |\Psi\rangle \,. \tag{3.4}$$

where $|\Psi\rangle$ is a superposition of $|e\rangle$ and $|g\rangle$. The solution for this simple system, given in [27], is straight-forward, but more involved than we wish to present here. After invoking the rotating wave approximation and making appropriate coordinate transformations, the Hamiltonian can be transformed into a time independent form.

In the limit of large detuning, $\delta \gg \Omega_{eg}$, the eigenvalues and eigenvectors of the new coordinates can be related to the original states. In this case, one can find the ac Stark shift of the original ground and excited states due to the off-resonant light field:

$$\Delta E_g = -\Delta E_e \simeq \frac{\hbar \Omega_{eg}^2}{4\delta} \,. \tag{3.5}$$

For red detuned light ($\delta < 0$), the ground state energy level shifts lower.[1] In the limit of $\delta = 0$, one can show that the probability for an atom to be in the excited state after applying the light field for a time τ is given by:

$$P_e = \frac{1}{2}[1 - \cos(\Omega_{eg}\tau)] \,, \tag{3.6}$$

and hence the atom oscillates between states at frequency Ω_{eg}. For non-zero detuning, the oscillation occurs at the generalized Rabi frequency, $\Omega_r \equiv \sqrt{\Omega_{eg}^2 + \delta^2}$. If the intensity and duration of the pulse are adjusted so that $\Omega_{eg}\tau = \pi$, the atom will be transferred completely to the excited state. If $\Omega_{eg}\tau = \pi/2$, the atom is put in a 50/50 superposition of the ground and excited states. These are called π and $\pi/2$ pulses, respectively, and the same idea applies to the Raman transitions considered in section 3.5.

3.2 Laser cooling

To treat the problem of an irradiated two level atom including spontaneous emission from the upper level, a density matrix approach is appropriate. A solution can be obtained using the optical Bloch equations, a vector model analogous to the treatment used for magnetic resonance. To determine the scattering rate and force on the atom, the steady-state solution is sufficient. This solution is derived in detail in [67, ch. 5] and elsewhere, and therefore we have only summarized key results here. For additional information on the density matrix and optical Bloch equation approaches, see, for example, [68, ch. 4] and [66].

---

[1]Including spontaneous emission changes the ac Stark shift expression, but Equation 3.5 is still valid in the limit of large detuning.

The time between photon scattering events (the inverse of the scattering rate) is proportional to $\tau_n = 1/\Gamma$, the natural lifetime of the state, and inversely proportional to P_e, the probability for an atom to be in the excited state, or:

$$\tau_{scat} = \frac{\tau_n}{P_e} \,. \tag{3.7}$$

Cesium has a natural linewidth of $\Gamma = 2\pi \times 5.18$ MHz, corresponding to $\tau_n \simeq 30$ nsec. The steady-state probability of finding an atom in the excited state is equal to:

$$P_e = \frac{1}{2} \left[\frac{I/I_{sat}}{1 + I/I_{sat} + 4(\delta/\Gamma)^2} \right] \,, \tag{3.8}$$

where I/I_{sat} is a dimensionless ratio of the laser intensity, I, and the saturation intensity, I_{sat}. In the high intensity limit, P_e reaches a maximum of $1/2$, since in this case, the atom oscillates between the two states, spending equal time in each. We wish to define I_{sat} such that $I = I_{sat}$ gives $P_e = 1/4$ when the detuning $\delta = \omega_L - \omega_{eg} = 0$, and therefore we require:

$$\frac{I}{I_{sat}} = 8 \frac{|\Omega_{eg}|^2}{\Gamma^2} \,. \tag{3.9}$$

The saturation intensity can be also be written as:[2]

$$I_{sat} = \frac{\hbar \omega \Gamma k^2}{12\pi} \,. \tag{3.10}$$

For cesium, $I_{sat} \simeq 1.1$ mW/cm^2.

Atoms absorb photons with a particular k-vector given by the laser propagation direction, but the photons scattered by spontaneous emission when the atom relaxes to the ground state are emitted randomly in all directions. Therefore, the atom acquires a net momentum kick from absorbed photons, but the momentum recoil from spontaneously emitted photons averages over all directions and gives no net momentum transfer. The scattering force exerted on the atom corresponding to this

---

[2]We have used the relations $\Gamma = \frac{4}{3\hbar} k^3 |\boldsymbol{d}|^2$ from [69] and $I = \frac{c}{4\pi} \langle |E|^2 \rangle$.

process is given by:

$$\boldsymbol{F}_{scat} = \frac{\hbar \boldsymbol{k}}{\tau_{scat}} = \frac{\hbar \boldsymbol{k} \Gamma}{2} \left[\frac{I/I_{sat}}{1 + I/I_{sat} + 4(\delta/\Gamma)^2} \right] . \tag{3.11}$$

3.2.1 Doppler cooling

If counterpropagating laser beams that are both red-detuned by δ irradiate an atom with velocity $\boldsymbol{v}$, then the atom sees the frequency of the laser opposing its velocity Doppler shifted toward resonance by $|\boldsymbol{k} \cdot \boldsymbol{v}|$, whereas the frequency of the other laser is Doppler shifted away from resonance by the same amount. (We assume that $|\delta| \geq |\boldsymbol{k} \cdot \boldsymbol{v}| \neq 0$.) The Doppler shift modifies δ in the $4(\delta/\Gamma)^2$ term in the denominator of Equations 3.8 and 3.11, and a greater number of photons are absorbed from the laser that opposes the motion of the atom since that laser is shifted closest toward resonance. This creates a force imbalance between the two beams that reduces the velocity of atoms along the cooling beams.[3] The force on the atoms can be written in the form $\boldsymbol{F}_{cool} = -\alpha \boldsymbol{v}$. The two beams described here only provide cooling in one dimension, but additional pairs of beams can be added to cool in two or three dimensions. The cooling temperature is limited by a competing heating process, since momentum kicks from the emitted photons cause the atom to undergo a diffusive random-walk. An analysis of these competing processes yields a lower limit on temperature called the Doppler limit, first predicted in [70] and given by:

$$k_B T_D = \frac{\hbar \Gamma}{2} . \tag{3.12}$$

For cesium, $T_D \simeq 125 \ \mu$K. Because the Doppler cooling light effectively forms a viscous medium for the atoms, this configuration is known as *optical molasses*.

3.2.2 Sub-Doppler cooling

As mentioned previously (see references in section 1.2.1), separate sub-Doppler cooling mechanisms have also been discovered. These mechanisms rely on ac Stark shifts,

---

[3]The action of the two beams can only be considered independently for low intensity.

multi-level atomic structure, finite pumping time, and polarization gradients. If an atom is irradiated with light of a particular polarization, it will eventually be optically pumped into the lowest allowed energy state. This generally requires multiple cycles of light absorption and spontaneous emission, and each cycle takes a time τ_{scat}. Suppose that red-detuned counterpropagating lasers are used with crossed-linear polarizations (crossed-circular also works). In this case, a standing wave is formed with polarizations alternating from circular (σ_+), to linear, to circular (σ_-), changing every $\lambda/8$ distance along the standing wave. If an atom pumped into the lowest energy state for one polarization (i.e. σ_+), were suddenly irradiated with the opposite polarization (σ_-) instead, it would no longer be in the state with minimum energy, because the ac Stark shifts depend on polarization. Due to the finite time required to pump the atoms from one state to another, an atom with non-zero velocity continually moves towards regions where it has higher internal potential energy, and in perpetually climbing potential hills, it loses kinetic energy. Polarization gradient cooling mechanisms can be used to cool cesium atoms to temperatures of about 2 μK.

3.3   Optical pumping

3.3.1 $F = 3$

The $F = 4 \rightarrow F' = 5$ cycling transition mentioned in section 3.1 is not perfectly closed, because there is a small probability of off-resonant excitation into the $F' = 4$ state. Atoms excited to $F' = 4$ can decay to the $F = 3$ state, where they will no longer be addressed by the $F = 4 \rightarrow F' = 5$ laser, so eventually all the atoms would be optically pumped to $F = 3$. To counteract this, one adds a weak *repumper* laser that is tuned to the $F = 3 \rightarrow F' = 4$ transition. The repumper kicks optically pumped atoms back up to the $F' = 4$ state where they may decay to the $F = 4$ state and once again undergo cycling transitions. Atoms can be efficiently pumped into the $F = 3$ state by using $F = 4 \rightarrow F' = 4$ light.

3.3.2 $m_F = 0$

It is also possible to optically pump atoms into the $m_F = 0$ Zeeman sublevel, the state used for the interferometer. This can be done using light tuned to the $F = 4 \rightarrow F' = 4$ transition with π polarization, namely linear polarization with the electric field along the quantization axis defined by the magnetic bias field. In this case, the $F = 4, m_F = 0$ state does not couple to the light due to selection rules, and atoms accumulate in that state. An $F = 3 \rightarrow F' = 4$ repumper (also π polarized) is also required. This problem has been studied theoretically in [71] and experimentally in [72]. We achieved $\sim 95\%$ efficiency with this technique (using the polarizations above, which [71] reported to be optimal) and used it for our single atomic beam apparatus, but it was abandoned due to complications with detection in the counterpropagating atomic beam setup. Rather than pumping into the $m_F = 0$ state, we now simply select those atoms already in that state, which only results in $\sim 1/6$ as many atoms.

3.4 Detecting atoms

We detect atoms that pass through a detection beam resonant with the $F = 4 \rightarrow F' = 5$ transition by imaging fluorescence from spontaneous emission onto a photo-diode. A laser excites atoms in the $F = 4$ state to the $F' = 5$ state and each relaxes back to $F = 4$ after scattering a photon in a random direction due to spontaneous emission. This cycle repeats and on average each atom scatters a photon every $\tau_{scat} = 2/\Gamma \simeq 60$ nsec, for $I > I_{sat}$. The number of photons collected per atom depends on the time it spends in the probe beam, which is inversely proportional to its velocity. The number of atoms/sec in the beam can be calculated from the fluorescence signal by using the scattering rate, the velocity distribution of the beam, and the imaging and detector efficiencies. Atoms exiting the interferometer may be in a superposition of two states, in which case the measurement procedure projects the state onto the $F = 4$ state.

Figure 3.1: Stimulated Raman transition level diagram. For the cesium transition used, $|g\rangle$ and $|e\rangle$ are the $F = 3$ and $F = 4$ ground state, respectively, with hyperfine splitting frequency difference $\omega_{\text{hfs}} = 9.2$ GHz, the cesium clock transition.

3.5   Stimulated Raman transitions
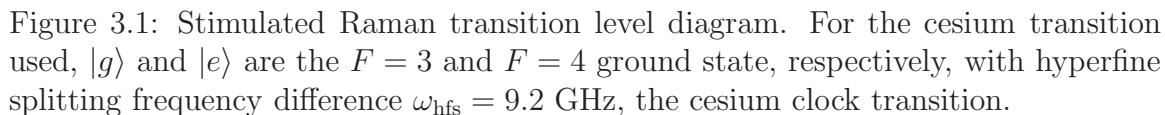
Two-photon stimulated Raman transitions are used in this experiment to form the interferometer by coherently manipulating atomic wavepackets. A cesium energy level diagram for Raman transitions is given in Fig. 3.1. Consider a three level atom with levels $|g\rangle$ and $|e\rangle$ coupled by an intermediate level $|i\rangle$, and illuminate it with two laser beams with frequencies ω_1 and ω_2 such that $\omega_1 - \omega_2 = \omega_{eg}$, and ω_1 and ω_2 are detuned from the $|g\rangle \rightarrow |i\rangle$ and $|e\rangle \rightarrow |i\rangle$ transitions by Δ. Then an atom originally in state $|g\rangle$ can absorb a photon with frequency ω_1 and undergo stimulated emission due to the laser with frequency ω_2, putting the atom in state $|e\rangle$. (The converse is true for atoms initially in state $|e\rangle$.) If Δ is large enough that spontaneous emission from the state $|i\rangle$ can be neglected, then $|i\rangle$ can be adiabatically eliminated, and the system behaves like a two-level system. The solution can be obtained by solving the Schrödinger equation, following a similar procedure to that outlined above for a two-level atom. The analysis of two-photon stimulated Raman transitions has been done in detail elsewhere, in [27, 73, 74, 75]. Therefore, we will omit the derivation and merely give the result, which will be useful for the interferometry theory and signal

modeling in Chapter 4. We have adopted the notation and procedure of [27].

For this two-photon problem, we can write the electric field (now including spatial dependence) as follows:

$$\boldsymbol{E} = \boldsymbol{E}_1 \cos(\boldsymbol{k}_1 \cdot \boldsymbol{x} - \omega_1 t + \phi_1) + \boldsymbol{E}_2 \cos(\boldsymbol{k}_2 \cdot \boldsymbol{x} - \omega_2 t + \phi_2) \,, \qquad (3.13)$$

where ϕ is the arbitrary phase at a chosen origin, and we define

$$\phi_{\mathrm{eff}} \equiv \phi_1 - \phi_2 \,. \qquad (3.14)$$

The Raman transition results in a momentum transfer of:

$$\boldsymbol{k}_{\mathrm{eff}} \equiv \hbar(\boldsymbol{k}_1 - \boldsymbol{k}_2) \,, \qquad (3.15)$$

which is $\simeq 2\hbar\boldsymbol{k}_1$ for counterpropagating lasers, and $\simeq 0$ for copropagating lasers. The momentum kick in the counterpropagating case corresponds to a recoil velocity of $v \simeq 7$ mm/sec. The transition produces a one-to-one correspondence between momentum and internal energy states, so if an atom is initially in the state $|g, \boldsymbol{p}\rangle$, we can use the basis states $|g, \boldsymbol{p}\rangle$ and $|e, \boldsymbol{p} + \hbar\boldsymbol{k}_{\mathrm{eff}}\rangle$ to describe its state after the transition. Factoring out the time evolution due to the energy allows the state to be written in terms of slowly varying amplitudes $c_{g,\boldsymbol{p}}$ and $c_{e,\boldsymbol{p}+\hbar\boldsymbol{k}_{\mathrm{eff}}}$ as follows:

$$|\Psi(t)\rangle = c_{e,\boldsymbol{p}+\hbar\boldsymbol{k}_{\mathrm{eff}}}(t) e^{-i\left(\omega_e + \frac{|\boldsymbol{p}+\hbar\boldsymbol{k}_{\mathrm{eff}}|^2}{2m\hbar}\right)t} |e, \boldsymbol{p} + \hbar\boldsymbol{k}_{\mathrm{eff}}\rangle + c_{g,\boldsymbol{p}}(t) e^{-i\left(\omega_g + \frac{|\boldsymbol{p}|^2}{2m\hbar}\right)t} |g, \boldsymbol{p}\rangle \,.$$
$$(3.16)$$

Since the de Broglie wavelength of atoms in the atomic beam in our apparatus is much shorter than an optical wavelength, we treat the position of the atom classically but use quantum mechanics to determine the evolution of the atom's internal state. If a Raman pulse (with constant amplitude envelope) is turned on from time t_0 until time $t_0 + \tau$, one can relate the state population coefficients before and after the pulse by the following equations:

$$c_{e,\boldsymbol{p}+\hbar\boldsymbol{k}_{\text{eff}}}(t_0 + \tau) = e^{-i(\Omega_e^{\text{AC}}+\Omega_g^{\text{AC}})\tau/2}e^{-i\delta_{12}\tau/2}\left\{c_{e,\boldsymbol{p}+\hbar\boldsymbol{k}_{\text{eff}}}(t_0)\left[\cos\left(\frac{\Omega_r'\tau}{2}\right)\right.\right.$$
$$\left.\left. - i\cos\Theta\sin\left(\frac{\Omega_r'\tau}{2}\right)\right] + c_{g,\boldsymbol{p}}(t_0)e^{-i(\delta_{12}t_0+\phi_{\text{eff}})}\left[-i\sin\Theta\sin\left(\frac{\Omega_r'\tau}{2}\right)\right]\right\} \quad (3.17)$$

$$c_{g,\boldsymbol{p}}(t_0+\tau) = e^{-i(\Omega_e^{\text{AC}}+\Omega_g^{\text{AC}})\tau/2}e^{i\delta_{12}\tau/2}\left\{c_{e,\boldsymbol{p}+\hbar\boldsymbol{k}_{\text{eff}}}(t_0)e^{i(\delta_{12}t_0+\phi_{\text{eff}})}\left[-i\sin\Theta\sin\left(\frac{\Omega_r'\tau}{2}\right)\right]\right.$$
$$\left. + c_{g,\boldsymbol{p}}(t_0)\left[\cos\left(\frac{\Omega_r'\tau}{2}\right) + i\cos\Theta\sin\left(\frac{\Omega_r'\tau}{2}\right)\right]\right\} \quad (3.18)$$

where the following definitions apply:

$$\delta_{12} = (\omega_1 - \omega_2) - \left(\omega_{eg} + \frac{\boldsymbol{p}\cdot\boldsymbol{k}_{\text{eff}}}{m} + \frac{\hbar|\boldsymbol{k}_{\text{eff}}|^2}{2m}\right) \quad (3.19)$$

$$\Omega_e^{\text{AC}} \equiv \frac{|\Omega_e|^2}{4\Delta}, \quad \Omega_g^{\text{AC}} \equiv \frac{|\Omega_g|^2}{4\Delta} \quad (3.20)$$

$$\Omega_e \equiv -\frac{\langle i|\,\boldsymbol{d}\cdot\boldsymbol{E}_2\,|e\rangle}{\hbar}, \quad \Omega_g \equiv -\frac{\langle i|\,\boldsymbol{d}\cdot\boldsymbol{E}_1\,|g\rangle}{\hbar} \quad (3.21)$$

$$\Omega_r' \equiv \sqrt{\Omega_{\text{eff}}^2 + (\delta_{12} - \delta^{\text{AC}})^2} \quad (3.22)$$

$$\Omega_{\text{eff}} \equiv \frac{\Omega_e^*\Omega_g}{2\Delta}e^{i\phi_{\text{eff}}} \quad (3.23)$$

$$\delta^{\text{AC}} \equiv (\Omega_e^{\text{AC}} - \Omega_g^{\text{AC}}) \quad (3.24)$$

$$\sin\Theta = \Omega_{\text{eff}}/\Omega_r', \quad \cos\Theta = -(\delta_{12} - \delta^{\text{AC}})/\Omega_r', \quad 0 \le \Theta \le \pi \quad (3.25)$$

Note that the detuning in Equation 3.19 contains the Doppler shift, $\boldsymbol{p}\cdot\boldsymbol{k}/m$, as well as a recoil shift term, $\hbar|\boldsymbol{k}_{\text{eff}}|^2/2m$, due to conservation of energy (see section 4.5). The ac Stark frequency shifts are given in Equation 3.20. The two-photon effective Rabi frequency is denoted Ω_{eff}, and Ω_r' is the generalized Rabi frequency for non-zero detuning.

With the optical injection locking technique we use to obtain the Raman laser frequencies, Δ is varied by changing the Raman master laser frequency, and δ_{12} may

be varied by changing the rf synthesizer frequency as well as by Doppler shifts. The implementation of the Raman laser system is discussed in detail in section 5.8.

Raman transitions have several useful features for our purposes. First of all, the Raman process is sensitive to the frequency *difference* between the lasers, which can be established precisely with an rf synthesizer and does not require highly stable individual lasers. Spontaneous emission can be avoided because the transition is between long-lived ground states, and both Raman lasers may be detuned far from the excited state. By adjusting the pulse area, one can achieve either π pulses (mirrors) or $\pi/2$ pulses (beamsplitters). The excitation geometry can be adjusted for counterpropagating transitions (velocity sensitive, the atom gets a momentum kick), or copropagating transitions (velocity insensitive, no momentum kick). The linewidth of the transition depends on the duration of the pulse, τ, so shorter pulses with higher intensity can be used to address a broader velocity distribution of atoms, increasing the number of atoms that participate in the signal. The ac Stark shift of the ground state energy level difference can be made to cancel by adjusting the intensity ratio of the two Raman beams. Finally, the phase and frequency of the Raman beams can be adjusted, which is convenient for interferometer data acquisition and rotation bias.

Compared to other techniques, Raman transition beamsplitters have some potential benefits. Light beamsplitters in general have the advantage over mechanical gratings that they do not aperture the atomic beam, and can not clog over time. Mechanical gratings are more difficult to vibrationally isolate, since they must be mounted inside the vacuum chamber. Also, mechanical gratings and Bragg beamsplitters do not change the internal state of the atom, and because the rotation phase shift depends on the area and therefore on the diffraction order, the atomic source must be highly collimated for good contrast. This collimation requirement on the atomic beam results in a lower usable flux than with Raman transitions.

Chapter 4

Atom interferometer theory

This chapter gives an overview of the theory necessary for understanding and calculating the gyroscope interferometer phase shift, and the calculation is performed to first order using various approaches. Section 4.1 presents a heuristic example of an optical acceleration measurement. Section 4.2 gives a schematic of our gyroscope interferometer configuration. Section 4.3 introduces the path integral method of calculating phase shifts due to propagation through the interferometer (either through free space or in an external potential). Phase shifts due to the Raman lasers are treated separately in section 4.4. In this section, the spatially separated cw Raman beams are treated as temporal pulses with duration given by the time of flight across each laser beam. Section 4.5 adopts the spatial domain viewpoint, in which the Raman beams are considered to be static, dictating stationary solutions and strict energy conservation. Section 4.6 summarizes several possible interpretations of the Sagnac effect, which can be ascribed to different physical causes depending on the viewpoint adopted in the analysis. Finally, a numerical model of the gyroscope signal is presented in section 4.7.

4.1   Laser acceleration measurement analogy

In the derivation of the Sagnac effect in Chapter 1, the phase shift arose due to a rotation-induced difference in path length between the two arms of the interferometer.
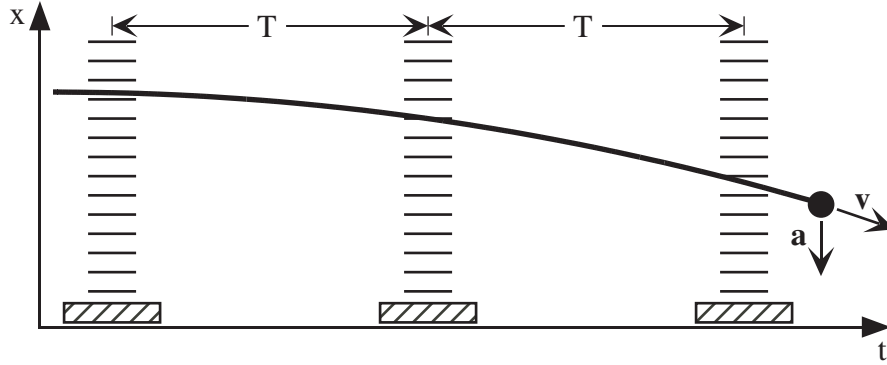
Figure 4.1: Laser acceleration measurement. Laser beams are used as fine rulers to measure the position of a freely falling test mass relative to an accelerating reference frame. Measurement at three points is sufficient to determine the acceleration. The light wavefronts are shown as short line segments in a standing wave configuration, reflecting from mirrors (hatched).

Another interpretation is possible, in which acceleration (linear or Coriolis) changes the light phase at the laser-atom interaction point by shifting the coordinate in space-time where the atom intercepts the light beam. To motivate this interpretation, let us consider an example of how an acceleration measurement might be made. Suppose one wishes to determine the relative acceleration between the inertial reference frame of a freely falling particle and the accelerated lab frame. The acceleration of the particle can be measured by monitoring its displacement relative to a fixed reference in the lab frame. A schematic for such a measurement is shown in Fig. 4.1. The acceleration can be uniquely determined by measuring the position of the particle at three times separated by T, since the expression for distance traveled, $x = \frac{1}{2}at^2 + vt$, has three unknowns. The three position measurements will have the following values:

$$
\begin{aligned}
x_1 &= \frac{1}{2}at_1^2 + v_x t_1 + x_0 \\
x_2 &= \frac{1}{2}a(t_1 + T)^2 + v_x(t_1 + T) + x_0 \\
x_3 &= \frac{1}{2}a(t_1 + 2T)^2 + v_x(t_1 + 2T) + x_0
\end{aligned}
\tag{4.1}
$$

Combining these measurements to compute a, one finds:

$$x_1 - 2x_2 + x_3 = aT^2 \,.\tag{4.2}$$

One way that such a measurement could be made is by interferometrically measuring the position of a falling corner cube reflector at three times. This is essentially the approach used in commercial gravimeters made by Micro-g Solutions. In our case, we use atoms as test particles (advantageous because they are all identical), and atomic physics processes record a function of the light phase at the three interaction points onto the atomic wavefunction. With either the atom or the corner cube approach, the wavelength of the laser light serves as a fine ruler to measure the position. The light phase yields position information, since $\phi = kx$. For our atom interferometer, the effective wavelength is $\simeq \lambda/2$ because k_{eff} is the relevant parameter for the Raman transition. Multiplying Equation 4.2 by k_{eff} yields:

$$\Delta\Phi = \phi_1 - 2\phi_2 + \phi_3 = k_{\text{eff}}aT^2 \,.\tag{4.3}$$

The procedure used in this example yields the same result as for the atom interferometer when the phase shifts acquired by atoms at the points of interaction with the Raman lasers are computed for curved trajectories in the lab frame, as described in section 4.4.

4.2 Gyroscope interferometer configuration

A schematic of the interferometer configuration used for the gyroscope is shown in Fig. 4.2. The geometry of our interferometer looks different than that of Fig. 4.1 because of the momentum recoil when the atoms interact with the Raman laser beams; however, the resulting phase shift is the same. Atoms in a thermal beam are pumped into the $F = 3$ state, and then pass through a sequence of three Raman laser beams. The first beam ($\pi/2$) puts the atoms in a coherent superposition of the $F = 3$ and $F = 4$ ground states. Due to conservation of momentum with the laser interactions, each internal state is associated with a particular transverse momentum.
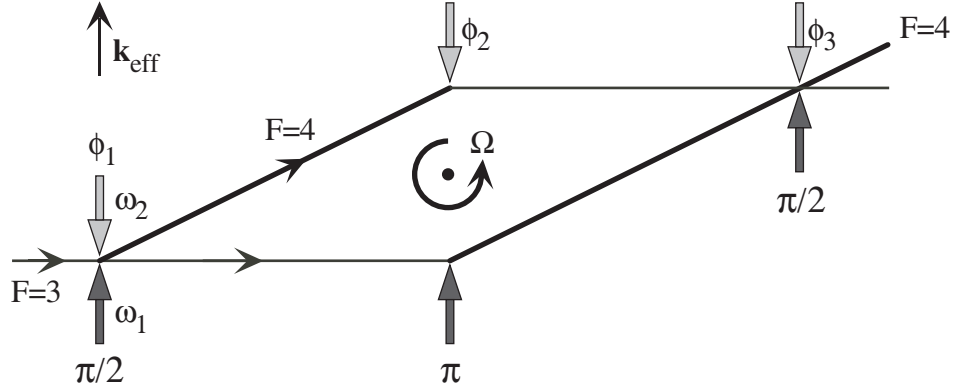
Figure 4.2: Gyroscope interferometer configuration.

(Interferometry with internal state labeling is discussed in [76].) This first pulse serves as a beamsplitter, causing the atomic wavepackets to divide into two trajectories. The second beam (π) acts as a mirror by exchanging the atomic states and momenta, deflecting the trajectories back towards each other. The third beam ($\pi/2$) acts as a beamsplitter that recombines the two trajectories so interference can occur. Rotation induces a relative phase-shift between the two paths of the interferometer, and the interference signal can be observed by measuring the number of atoms in the $F = 4$ state. Since atoms from the atomic beam have random relative phase, the interference effect is a single particle phenomenon with coherence length given by the de Broglie wavelength.

The general requirement for interference to occur is that a particle initially in a state $|\psi_0\rangle$ must evolve into a superposition of two (or more) intermediate states that are not uniquely distinguished by the measurement process:

$$|\psi_0\rangle \rightarrow |\psi_1\rangle + |\psi_2\rangle \ . \tag{4.4}$$

The probability of detecting the particle in a particular final state $|F\rangle$ is given by the expectation value of the projection operator, $|F\rangle\langle F|$. Defining $\psi(F) \equiv \langle F|\psi\rangle$, one finds:

$$P(F) = |\psi_1(F)|^2 + |\psi_2(F)|^2 + 2\operatorname{Re}\left\{\psi_1(F)\psi_2^*(F)\right\} \ . \tag{4.5}$$

The interference is due to the cross-term, which is sensitive to the relative phase acquired between the states.

4.3 Path integral approach

The Feynman path integral approach is a useful method for computing the phase shift as the atoms propagate through the interferometer. The phase shifts acquired during the interaction with the Raman lasers are treated separately in section 4.4. A path integral analysis of various interferometer configurations including ours has been performed by Storey and Cohen-Tannoudji [5], who also give rules for handling interactions with light pulses. A theoretical discussion of the rotation-induced phase shift in a Mach-Zehnder atom interferometer with light beamsplitters was first given in [77]. For additional discussion of the path integral formulation, see [78, 79], and see [80] for a review of Lagrangian mechanics.

In classical mechanics, Hamilton's principle of least action states that a particle moving in an external potential $V(\boldsymbol{r})$ will travel along the path for which the integral

$$S_\Gamma \equiv \int_{t_a}^{t_b} L[\boldsymbol{r}(t), \dot{\boldsymbol{r}}(t)] \mathrm{d}t \tag{4.6}$$

is stationary, where the Lagrangian is defined as $L[\boldsymbol{r}, \dot{\boldsymbol{r}}] \equiv \frac{1}{2}m\dot{\boldsymbol{r}}^2 - V(\boldsymbol{r})$, and S_Γ is the *action* along the path Γ. Stationary means that the integral is extremal with respect to small variations in the path, that is, $\delta S_\Gamma = 0$. The classical action is denoted

$$S_{\mathrm{cl}} \equiv S_{\mathrm{cl}}(\boldsymbol{r}_b, t_b; \boldsymbol{r}_a, t_a), \tag{4.7}$$

and represents the action evaluated along the classical path between the endpoints a and b, depending only on the endpoints.

In quantum mechanics, Feynman's path integral method can be used to compute the probability of a particle at point a ending up at point b by summing the amplitudes of all paths from a to b. The phase acquired due to propagation along each path is $S_\Gamma/\hbar$, but in the limit of $S_\Gamma \gg \hbar$, the phase contributions away from the

classical path tend to oscillate rapidly and cancel. This classical limit is appropriate for interferometers with macroscopic spatial extent such as ours. The phase of the wavefunction at the final point b then depends on the initial wavefunction at a and the classical action, as follows:

$$|\Psi(\boldsymbol{r}_b, t_b)\rangle \propto e^{\left(iS_{\mathrm{cl}}/\hbar\right)} |\Psi(\boldsymbol{r}_a, t_a)\rangle \,. \tag{4.8}$$

The atom is treated classically with its position and velocity corresponding to the center of mass and group velocity of a spatially localized quantum mechanical wave-packet.

4.3.1 Perturbative limit

The phase shift due to a perturbation to the Lagrangian ΔL can be calculated to first order by integrating the perturbing potential over the unperturbed classical path, denoted Γ_0. Therefore, the phase difference between the two interferometer arms is given by:

$$\Delta\Phi = \frac{1}{\hbar} \oint_{\Gamma_0} \Delta L \, \mathrm{d}t \,. \tag{4.9}$$

This perturbative approach can be used to compute phase shifts from various sources, including accelerations and electromagnetic fields.

Rotating coordinate frames

To determine the appropriate perturbation to the Lagrangian for a rotating interferometer, consider an inertial coordinate frame (primed) and a frame rotating with angular frequency Ω (unprimed) with a common origin. The rate of change of a vector $\boldsymbol{r}$ describing the position of a particle in the rotating frame can be obtained in the inertial frame ($\boldsymbol{r}'$) via the following operator equation, derived in [81]:

$$\left(\frac{\mathrm{d}}{\mathrm{d}t}\right)_{\mathrm{inertial}} = \left(\frac{\mathrm{d}}{\mathrm{d}t}\right)_{\mathrm{rotating}} + \boldsymbol{\Omega} \times \tag{4.10}$$

or more specifically,

$$\frac{\mathrm{d}\boldsymbol{r}'}{\mathrm{d}t} = \frac{\mathrm{d}\boldsymbol{r}}{\mathrm{d}t} + \boldsymbol{\Omega} \times \boldsymbol{r}\,. \tag{4.11}$$

Similarly, one can compute the acceleration by applying Equation 4.10 twice:

$$\frac{\boldsymbol{F}}{m} = \frac{\mathrm{d}^2\boldsymbol{r}'}{\mathrm{d}t^2} = \frac{\mathrm{d}^2\boldsymbol{r}}{\mathrm{d}t^2} + 2\boldsymbol{\Omega} \times \frac{\mathrm{d}\boldsymbol{r}}{\mathrm{d}t} + \frac{\mathrm{d}\boldsymbol{\Omega}}{\mathrm{d}t} \times \boldsymbol{r} + \boldsymbol{\Omega} \times (\boldsymbol{\Omega} \times \boldsymbol{r})\,. \tag{4.12}$$

where $\boldsymbol{F}$ is an external force applied to the particle in the inertial frame. Then one can identify the familiar Coriolis and centripetal accelerations in the rotating frame:

$$\boldsymbol{a}_{\mathrm{Cor}} = -2\boldsymbol{\Omega} \times \boldsymbol{v} \tag{4.13}$$

$$\boldsymbol{a}_{\mathrm{cen}} = -\boldsymbol{\Omega} \times (\boldsymbol{\Omega} \times \boldsymbol{r})\,. \tag{4.14}$$

The Lagrangian is determined by the energy, and has the same value in both frames. For a free particle in the inertial frame,

$$L' = \frac{1}{2}mv'^2 \tag{4.15}$$

and rewritten using rotating frame coordinates, it is:

$$L' = L = \frac{1}{2}m(\boldsymbol{v} + \boldsymbol{\Omega} \times \boldsymbol{r})^2 \tag{4.16}$$

$$= \frac{1}{2}mv^2 + m\boldsymbol{\Omega} \cdot (\boldsymbol{r} \times \boldsymbol{v}) + \mathcal{O}(\Omega^2)\,. \tag{4.17}$$

In the rotating frame, Coriolis acceleration adds a perturbation $\Delta L = m\boldsymbol{\Omega} \cdot (\boldsymbol{r} \times \boldsymbol{v})$ to the free particle Lagrangian.

Now one can use Equation 4.9 to compute the phase shift due to this perturbation:

$$\Delta\Phi_\Omega = \frac{m\boldsymbol{\Omega}}{\hbar} \cdot \oint_{\Gamma_0} (\boldsymbol{r} \times \boldsymbol{v})\mathrm{d}t = \frac{m\boldsymbol{\Omega}}{\hbar} \cdot \oint_{\Gamma_0} (\boldsymbol{r} \times \mathrm{d}\boldsymbol{r})\,. \tag{4.18}$$

The integral is equal to $2\boldsymbol{A}$, where $\boldsymbol{A}$ is the area enclosed by the paths, since $\boldsymbol{r} \times \mathrm{d}\boldsymbol{r}$ is the area of a parallelogram with adjacent edges defined by vectors $\boldsymbol{r}$ and $\mathrm{d}\boldsymbol{r}$. This

results in the usual Sagnac phase shift expression:

$$\Delta\Phi_\Omega = \frac{2m}{\hbar}\boldsymbol{\Omega}\cdot\boldsymbol{A}\,. \tag{4.19}$$

4.4 Interaction rules for lasers and atoms

One can develop a simple set of rules to describe the interaction of atoms with the laser beamsplitters. From the stimulated Raman transition solutions given in Equations 3.17 and 3.18, one can compute the phase shift picked up by the atom at each point of interaction with the laser light. Then each interferometer trajectory can be treated separately, with appropriate multiplying factors at each laser interaction point. This prescription is commonly used in the literature, for example in [77, 82, 5, 83]. We neglect ac Stark shifts here for simplicity, since experimentally we optimize the intensity ratio between the Raman beams so they approximately cancel. One can represent atomic states using spinor notation, and write the Raman transition equations in matrix form. In this case, the state vector can be written in terms of amplitude coefficients in the momentum basis as follows:

$$|\Psi(t)\rangle = c_{e,\boldsymbol{p}+\hbar\boldsymbol{k}_{\mathrm{eff}}}(t)\,|e,\boldsymbol{p}+\hbar\boldsymbol{k}_{\mathrm{eff}}\rangle + c_{g,\boldsymbol{p}}(t)\,|g,\boldsymbol{p}\rangle = \begin{bmatrix} c_{e,\boldsymbol{p}+\hbar\boldsymbol{k}_{\mathrm{eff}}}(t) \\ c_{g,\boldsymbol{p}}(t) \end{bmatrix}. \tag{4.20}$$

The Raman transition equations are greatly simplified in the limit of small detuning,[1] $\delta_{12} \ll \Omega_{eg}$. Then for a $\pi/2$ pulse, one finds:

$$|\Psi(t_0+\tau)\rangle \simeq \frac{1}{\sqrt{2}} \begin{bmatrix} 1 & -ie^{-i(\delta_{12}t_0+\phi_{\mathrm{eff}})} \\ -ie^{i(\delta_{12}t_0+\phi_{\mathrm{eff}})} & 1 \end{bmatrix} |\Psi(t_0)\rangle\,. \tag{4.21}$$

---

[1]The small detuning limit is a reasonable approximation throughout this work, because $\delta_{12}/\Omega_{eg} \simeq 4\times10^{-4}$ for a detuning of $\delta_{12} \simeq 2\pi \times 110$ Hz, which corresponds to the Raman beam Doppler shift due to the Earth's rotation. Here $\Omega_{eg} \simeq \pi/\tau \simeq 2\pi \times 300$ kHz, since $\tau \simeq 1.7\times10^{-6}$ for a 0.5 mm Raman laser waist and a 300 m/sec atomic beam.

And for a π pulse, one finds:

$$|\Psi(t_0 + \tau)\rangle \simeq \begin{bmatrix} 0 & -ie^{-i(\delta_{12}t_0+\phi_{\text{eff}})} \\ -ie^{i(\delta_{12}t_0+\phi_{\text{eff}})} & 0 \end{bmatrix} |\Psi(t_0)\rangle \ . \qquad (4.22)$$

Instead of keeping track of both states at once, one can follow an atom along a particular path, and at each point where the atom interacts with a Raman pulse, multiply by an appropriate factor that depends on the input and output states and the pulse area. This approach is summarized by Table 4.1:

	$\|e(t_0 + \tau)\rangle$	$\|g(t_0 + \tau)\rangle$
$\|e(t_0)\rangle$	$\cos(\Omega_{eg}\tau/2)$	$-i\sin(\Omega_{eg}\tau/2)e^{i(\delta_{12}t_0+\phi_{\text{eff}})}$
$\|g(t_0)\rangle$	$-i\sin(\Omega_{eg}\tau/2)e^{-i(\delta_{12}t_0+\phi_{\text{eff}})}$	$\cos(\Omega_{eg}\tau/2)$

Table 4.1: Transition rules for atom interactions with light. Multiplicative factors connect initial states (rows) with final states (columns).

The detuning δ_{12} (Equation 3.19) contains a Doppler shift term that when multiplied by t_0 can be written $\boldsymbol{k}_{\text{eff}} \cdot \boldsymbol{v}t_0 = \boldsymbol{k}_{\text{eff}} \cdot \boldsymbol{x}$. Therefore the phase factors become

$$e^{\mp i(\delta_{12}t_0+\phi_{\text{eff}})} = e^{\pm i[\boldsymbol{k}_{\text{eff}} \cdot \boldsymbol{x} - (\omega_{\text{eff}}-\omega_{eg}-\omega_r)t_0 - \phi_{\text{eff}}]} , \qquad (4.23)$$

where $\omega_{\text{eff}} = \omega_1 - \omega_2$, $\omega_r = \hbar k_{\text{eff}}^2/2m$ is the recoil frequency, and the factor $e^{i\boldsymbol{k}_{\text{eff}} \cdot \boldsymbol{x}}$ corresponds to the momentum of the absorbed photon.

As an example, let us compute the phase shift due to the light for unperturbed trajectories in the lab frame, for which we previously computed the phase shift due to spatial propagation. Defining coordinates as shown in Fig. 4.3, we can compute the state probability amplitudes for the interfering paths, assuming perfect Raman pulse area and that initially $c_{g,\boldsymbol{p}} = 1$.
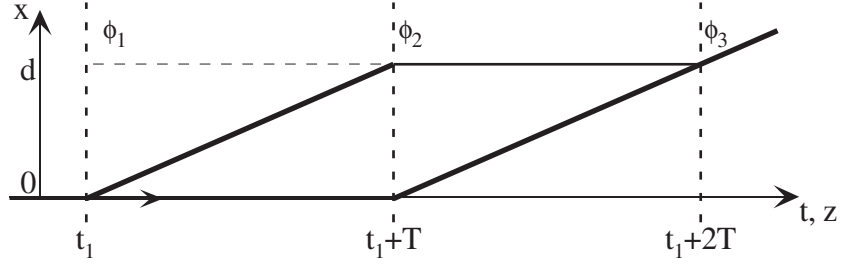
Figure 4.3: Phase shift computation coordinate system for unperturbed paths in the lab frame.

For the upper path shown in the figure, one finds:

$$c^{\uparrow}_{e,\boldsymbol{p}+\hbar\boldsymbol{k}_{\text{eff}}} = -\frac{i}{\sqrt{2}} \exp[i(k_{\text{eff}} \cdot 0 - \omega_{\text{eff}} t_1 - \phi_1)]$$

$$\times -i \exp[-i(k_{\text{eff}} \cdot d - \omega_{\text{eff}}(t_1 + T) - \phi_2)]$$

$$\times -\frac{i}{\sqrt{2}} \exp[i(k_{\text{eff}} \cdot d - \omega_{\text{eff}}(t_1 + 2T) - \phi_3)]. \quad (4.24)$$

Here ϕ_j represents the phase of Raman pulse j, defined relative to a common origin. For the lower path of the figure,

$$c^{\downarrow}_{e,\boldsymbol{p}+\hbar\boldsymbol{k}_{\text{eff}}} = \frac{1}{\sqrt{2}} \times -i \exp[i(k_{\text{eff}} \cdot 0 - \omega_{\text{eff}}(t_1 + T) - \phi_2)] \times \frac{1}{\sqrt{2}}. \quad (4.25)$$

The phase difference between the two paths due to the laser interactions is:

$$\Delta\Phi_L = \phi_1 - 2\phi_2 + \phi_3. \quad (4.26)$$

The probability of detecting an atom in the excited state ($F = 4$) is given by $P_e = \left| c^{\uparrow}_{e,\boldsymbol{p}+\hbar\boldsymbol{k}_{\text{eff}}} + c^{\downarrow}_{e,\boldsymbol{p}+\hbar\boldsymbol{k}_{\text{eff}}} \right|^2$, and by substituting for Equations 4.24 and 4.25 and adding in the spatial propagation phase shift from Equation 4.19, one finds the form of the interferometer signal in the limit of perfect contrast:

$$P_e = \frac{1}{2} \left[1 - \cos\left(\frac{2m}{\hbar} \boldsymbol{\Omega} \cdot \boldsymbol{A} + \phi_1 - 2\phi_2 + \phi_3 \right) \right]. \quad (4.27)$$

Similarly, one can compute the phase shifts due to spatial propagation and laser interactions along curved trajectories in the lab frame. In this case, the spatial propagation phase shift cancels, and $\Delta\Phi_\Omega$ arises from the laser interactions. This calculation is done in [5] for gravitational acceleration, but also applies for rotations, since to first order for small rotation rates, $\boldsymbol{a}_{\mathrm{Cor}}$ remains perpendicular to the direction of the initial velocity $\boldsymbol{v}$. For a general inertial acceleration, one finds a phase shift of:

$$\Delta\Phi = -\boldsymbol{k}_{\mathrm{eff}} \cdot \boldsymbol{a} T^2 + \phi_1 - 2\phi_2 + \phi_3 \,, \qquad (4.28)$$

where $T = L/v$ is the time of flight between Raman beams and $\boldsymbol{a}$ is linear or Coriolis acceleration.

4.5   Conservation of energy and momentum

Atom interferometers using light beamsplitters can be classified into two types: spatial domain and time domain. Our interferometer is the spatial domain type, meaning that atoms in the atomic beam interact with spatially separated Raman laser beams that are on continuously. In contrast, time domain interferometers use lasers pulsed in time that interact with the entire ensemble of atoms at once.

For the spatial interferometer viewed in the lab frame, the laser beams constitute stationary potentials (neglecting rapid oscillations at optical frequencies), and energy must be strictly conserved. Furthermore, stationary solutions with definite energy exist. The atomic wavefunction can be represented as a wave-packet in momentum space by a sum of plane-waves, each of which has infinite spatial extent. Friedberg and Hartmann showed that this stationary picture can be approximately transformed into the equivalent of a time-dependent Schrödinger equation with z/v playing the role of time, where z is in the direction of atomic beam propagation [82, app. B]. (This is a good approximation for the gyroscope apparatus [84].) In this view, the limited spatial extent of a Raman beam effectively results in a temporal pulse in the inertial frame of an atom in the atomic beam.

One can use conservation of energy to obtain a relationship between the Raman

difference frequency detuning and the Doppler shift due to the velocity of an atom relative to the Raman k-vector. We consider an atom initially in the $F = 3$ state with momentum $\boldsymbol{p}$, and equate the total energy of the atom plus laser fields before and after the Raman transition to find the following:

$$\hbar(\omega_1 + \omega_2) + \hbar\omega_g + \frac{\boldsymbol{p}^2}{2m} = 2\hbar\omega_2 + \hbar\omega_e + \frac{(\boldsymbol{p} + \hbar\boldsymbol{k}_{\text{eff}})^2}{2m} , \tag{4.29}$$

where $\hbar\omega_g$ and $\hbar\omega_e$ are the internal energies of the $F = 3$ and $F = 4$ states. Note that there are two photons with frequency ω_2 after stimulated emission. Rearranging, we find:

$$0 = (\omega_1 - \omega_2) - \left(\omega_{eg} + \boldsymbol{k}_{\text{eff}} \cdot \boldsymbol{v} + \frac{\hbar \boldsymbol{k}_{\text{eff}}^2}{2m}\right) \equiv \delta_{12} , \tag{4.30}$$

where $\omega_{eg} \equiv \omega_e - \omega_g$.

If one scans the Raman detuning frequency in the time (spatial) domain case, one finds that the transition has a linewidth given by the Fourier transform of the temporal (spatial) pulse shape. For example, if the intensity of a Raman pulse in the time domain is optimized for a π pulse when tuned on resonance, the transition probability as a function of detuning for a square pulse envelope is:

$$|c_e(t_0 + \tau)|^2 = \frac{\pi^2}{4} \text{sinc}^2 \left(\frac{1}{2}\sqrt{1 + \delta_{12}/\Omega_{\text{eff}}}\right) , \tag{4.31}$$

where $\text{sinc}(x) \equiv \sin(\pi x)/(\pi x)$. (This result can be obtained by squaring the transition probability amplitude given in Equation 3.17.) In the spatial domain case, the frequency linewidth is given by the spread of momentum k-vectors of the light, and the uncertainty in k is given by the spatial Fourier transform of the pulse. Further discussion of spatial and time domain interferometers can be found in [85, 84, 86, 87].

The Raman transition linewidth can also be understood in terms of the Heisenberg uncertainty principle. In the spatial domain case, the light beam must satisfy:

$$w_0 \Delta k \geq \frac{1}{2} , \tag{4.32}$$

where $w_0 = \Delta x$ is the Gaussian beam waist (defined as $1/e^2$ radius and currently equal to 0.4 mm). The k-vector spread in a Gaussian beam is illustrated in Fig. 4.4. For
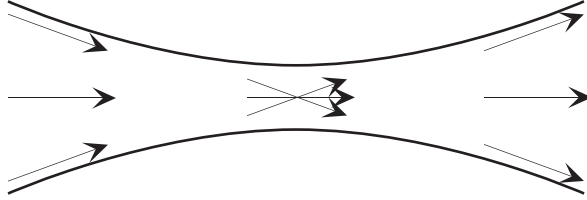
Figure 4.4: Schematic representation of the k-vector spread in a Gaussian beam.

a Gaussian beam, the transverse k-vector spread averages out at the waist, and the wavefront has infinite radius of curvature as expected. Due to diffraction, aperturing a plane-wave (or a large Gaussian beam) also results in a k-vector spread. If the Raman beam is not perfectly perpendicular to the atomic trajectory, an atom may still undergo a transition if the spread in k-vectors within the laser beams is large enough. In the case of single-frequency standing wave beamsplitters, single or multiple diffraction orders may be populated depending on the k-vector spread. For the Bragg scattering case [19], a thick beamsplitter is used and only one diffraction order is resonant since the k-vectors are well-defined. In the Kapitza-Dirac case [88], a thin beamsplitter with a large k-vector spread leads to multiple diffraction orders. For the time domain case, the finite Raman linewidth can be explained by the uncertainty relation $\Delta E \Delta t \geq \hbar$.

In the spatial domain case, if the Raman beams are tuned on the recoil-corrected resonance, $\delta \equiv \omega_1 - \omega_2 - (\omega_{eg} + \omega_r) = 0$, energy conservation requires that the Doppler shift $\boldsymbol{k}_{\mathrm{eff}} \cdot \boldsymbol{v} = 0$. (Before aligning our apparatus, we set the Raman rf frequency to compensate the recoil shift when using counterpropagating transitions, though alternatively this could be achieved by adjusting the angle of the Raman beams.)

In the case of non-zero Raman detuning, $\delta \equiv \omega_1 - \omega_2 - (\omega_{eg} + \omega_r) \neq 0$, a Doppler shift is required to satisfy the resonance condition, as Equation 4.30 shows. Since the k-vector of the resonant light is not perpendicular to the atomic trajectory, upon making a transition, an atom gets a longitudinal momentum kick (along the axis of

the initial momentum $\boldsymbol{p}$) equal to:

$$
\begin{aligned}
\Delta p &= \frac{\boldsymbol{p} \cdot (\hbar \boldsymbol{k}_{\text{eff}})}{p} \\
&= \frac{\hbar \delta}{v}
\end{aligned}
\tag{4.33}
$$

The path integral formalism can still be used, but the kinetic energy of the atom must be modified after interaction with the light. We use non-zero Raman detunings extensively for phase modulating the signal and for applying a rotation bias (discussed in section 5.8.3 and in Chapter 6), so this case has practical importance. Furthermore, the Sagnac shift can be viewed as arising from Raman detunings induced by Doppler shifts.

In an inertial (non-accelerated) frame,

$$
L = \frac{(\boldsymbol{p} + \Delta \boldsymbol{p})^2}{2m} \simeq \frac{p^2}{2m} + \Delta \boldsymbol{p} \cdot \boldsymbol{v} \, .
\tag{4.34}
$$

One can calculate the spatial propagation phase shift due to the change in longitudinal momentum by using the Lagrangian perturbation technique from section 4.3.1. In this case, integrating $\Delta L = \Delta \boldsymbol{p} \cdot \boldsymbol{v}$ yields:

$$
\Delta \Phi \simeq \frac{1}{\hbar} \int_0^{2T} \Delta \boldsymbol{p} \cdot \boldsymbol{v} \, \mathrm{d}t = \frac{1}{\hbar} \int_0^{2L} \Delta p \, \mathrm{d}z = \frac{\delta 2L}{v} .
\tag{4.35}
$$

(One may neglect ΔT in the upper limit of the integral, since $\Delta T \Delta p$ is second order.)

The difference in longitudinal momentum means that atoms traversing the upper and lower path differ in time of flight. If the two trajectories are to intersect at a particular point in space-time after the interferometer, they must start at slightly different points in space. Contrast is reduced if the difference in starting positions is a significant fraction of λ_{dB}, since we are considering single particle interference. Suppose the momentum increases by $|\Delta p|$ along the upper path. Then at the (common) starting time, atoms traversing the upper path must start at an earlier position $z_0 - |\Delta z|$, resulting in a phase shift of the form $\boldsymbol{k} \cdot \boldsymbol{z}$. The negative z displacement of the starting

coordinate results in a phase lag for the upper path of:

$$\Delta\Phi = 2\pi(-|\Delta z|)/\lambda_{dB}\,. \tag{4.36}$$

The overlap phase shift of Equation 4.36 cancels the spatial propagation phase shift of Equation 4.35.

Finally, the phase shift due to interactions with the laser light must be computed as in section 4.4, substituting the Doppler-shifted frequencies for ω_{eff}. The $\boldsymbol{k}_{\text{eff}}\!\cdot\!\boldsymbol{x}$ terms cancel in the inertial frame as they did for the unperturbed trajectories example, and have been omitted below. For the example above in which the first $\pi/2$ beam is blue-detuned by δ, the phase shift due to the detuning is equal to:

$$
\begin{aligned}
\Delta\Phi &= -(\omega_{\text{eff}} + \delta)(t_f - 2T') + \omega_{\text{eff}}(t_f - T') - (\omega_{\text{eff}} - \delta)t_f + \omega_{\text{eff}}(t_f - T) \\
&\simeq 2\delta T\,,
\end{aligned}
\tag{4.37}
$$

where t_f is the final time at which the paths interfere at a common point in space. T' and T are the times between pulses for the upper and lower paths, respectively. The laser arbitrary phase contributions ϕ_j have been omitted for simplicity. Equation 4.37 gives the net phase shift due to the Raman detuning, since Equation 4.36 and 4.35 cancel.

Conserving energy and satisfying the k-vector uncertainty relation given in Equation 4.32 implies a maximum detuning of $\delta_{\max} \sim v/2w_0$. However, due to the transverse velocity distribution of atoms in the atomic beam, a signal can be obtained over a broader range of detunings.

4.5.1 Rotation-induced Doppler shifts

In an inertial frame, rotation about the center of the π pulse appears as a Doppler shift of the $\pi/2$ beams equal to

$$\delta = \pm k_{\text{eff}}\Omega L\,, \tag{4.38}$$
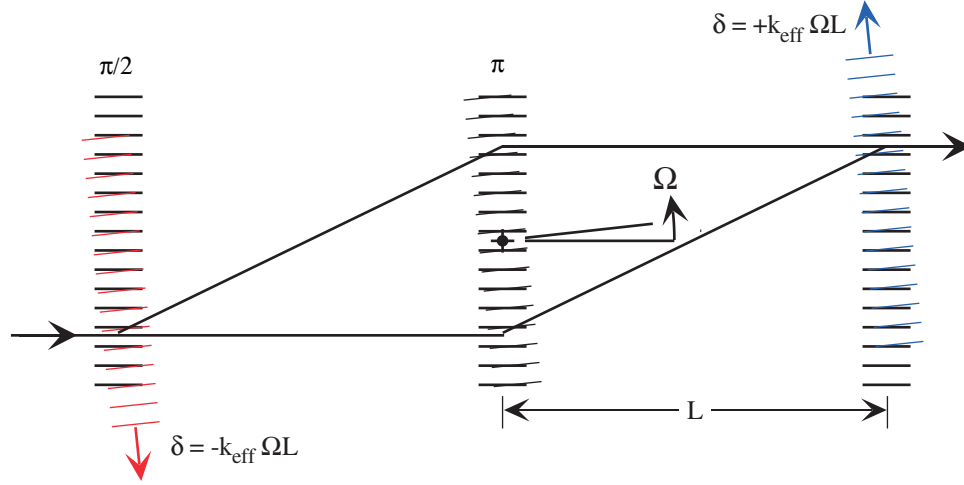
Figure 4.5: Rotation-induced Doppler shifts. The wavefronts of the 3 Raman pulses are drawn in their initial positions and after rotation of the apparatus about the center of the π pulse. Small rotations leave the π pulse essentially unchanged, but Doppler shift the $\pi/2$ pulses by $\pm k_{\text{eff}}\Omega L$. For clarity, only one Sagnac loop has been drawn, but the shifts are the same for each. The wavefronts and Sagnac loop are not drawn to scale.

with opposite signs for the North and South $\pi/2$ beams. Fig. 4.5 illustrates the Doppler shifts due to rotation. Note that the rotation-induced Doppler shift is independent of atom velocity and therefore is the same for both atomic beam directions. Section 5.8.3 describes how these shifts are compensated experimentally. Position and angle changes of the Raman beams are neglected, since for small rotation rates, the position changes by second order, and the angle change is smaller than the k-vector spread. Therefore, in the inertial frame, the Raman beams may be treated as static but with Doppler-shifted $\pi/2$ Raman detunings.

Substituting the Doppler shift of Equation 4.38 into the phase shift of Equation 4.37 and rearranging, one finds:

$$\Delta\Phi_\Omega = \boldsymbol{k}_{\text{eff}} \cdot (2\boldsymbol{\Omega} \times \boldsymbol{v})\frac{L^2}{v^2} , \tag{4.39}$$

which is equivalent to the usual Sagnac phase shift expression of Equation 4.19. The Doppler shifts can be compensated by detuning the Raman $\pi/2$ pulses by $\pm\delta$f. The

Raman beam detuning implementation is described in Chapter 5.

4.6   Phase shift interpretation summary

References to several viewpoints for calculating the Sagnac effect can be found in [43, 89]. The calculation is usually performed in either the lab frame or in an inertial frame. (Note that in the case of non-zero Raman detunings, the longitudinal momentum of the atom is not constant throughout the gyroscope.) Furthermore, the calculation may be performed for time domain or spatial domain beamsplitters. Bordé et al. have studied the theory of spatial domain beamsplitters in detail (including effects of finite pulse width, which have been neglected here) [85, 90, 83, 91, 92].

4.6.1   Time domain

In the time domain viewpoint, the longitudinal momentum of the atoms is conserved during Raman interactions. To determine the phase shift in the lab frame, the path integral perturbation technique may be used, in which case the phase shift arises due to propagation and can be calculated by integrating the perturbation to the Lagrangian over the straight, unperturbed trajectories as in Equation 4.9. In this case, the phase obtained from interactions with the laser is independent of acceleration.

The atoms actually follow curved trajectories in the lab frame due to the Coriolis acceleration. The phase shifts from propagation cancel when the classical action is evaluated along curved trajectories. Raman detunings can be treated by varying ω_{eff} in the laser interaction phase terms. This approach is used in section 5.8.3 to compute phase shifts when the $\pi/2$ or π Raman beams are detuned. In the lab frame, the lasers are not subject to Doppler shifts due to rotation.

In the inertial frame, longitudinal momentum kicks due to rotating Raman beams are cancelled by the phase shift due to the difference in starting points required for the paths to converge at the same time.

4.6.2   Spatial domain

In the spatial domain, energy is strictly conserved, but laser interactions induce longitudinal momentum changes due to Doppler shifts or non-zero Raman detunings. In the lab frame, the path integral perturbation technique may be used to calculate the phase shift using unperturbed trajectories, in which case the time and spatial domain problems behave equivalently. On perturbed (curved) trajectories, the acceleration phase shift arises due to interaction with the laser light, and spatial propagation phase shifts cancel.

In the inertial frame, the spatial propagation phase shift from integrating the perturbation to the Lagrangian is cancelled by the difference in starting points required, and the phase shift from atom interactions with the laser light at the Doppler shifted frequencies yields the acceleration phase shift.

4.7   Numerical model of gyroscope signal

To model the experimental signal, we used the Raman transition equations given in Equations 3.17 and 3.18 with the Raman beams frequencies set to resonance and ac Stark shifts neglected. Effects due to the finite width (duration) of the laser pulses have been neglected in this model, since $w_0 \ll L$ (or $\tau \ll T$). See [28] for the inclusion of these effects for the time domain case. Originally the Sagnac phase shift was allowed to arise from interaction with the phase of the Raman beams, but after this initial verification, we instead used the unperturbed (straight) trajectories and explicitly put in the Sagnac phase shift by hand, simplifying computation. The state amplitudes c_e were computed separately for the upper and lower interferometer paths shown in Fig. 4.6, and the amplitudes for ending up in the $F = 4$ state for the two paths were added and then squared to find the detection probability. Alternate paths due to imperfect pulse area that led to atoms ending up in the $F = 4$ state were also computed, since these result in a background offset to the interference signal. These non-interfering path amplitudes were squared individually and added to the interferometer detection probability to compute the contrast.
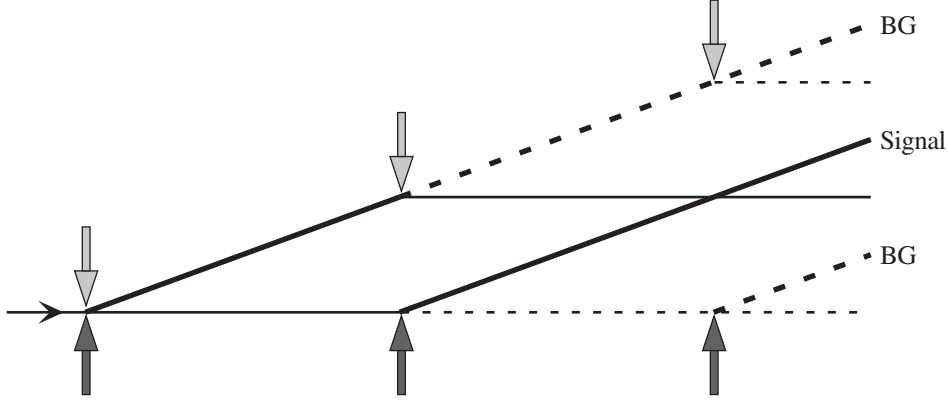
Figure 4.6: Gyroscope signal and background paths. When imperfect pulse area is considered, the additional paths shown with dashed lines contribute a non-interfering background to the detected signal that modifies contrast. Atoms start in the $F = 3$ state (thin lines) and atoms in the $F = 4$ state (thick lines) are detected.

The Raman pulse areas (π and $\pi/2$) were set to be optimal for the most probable velocity of the atomic beam and an integration over the measured longitudinal and transverse velocity distributions was performed to determine the contrast. The longitudinal velocity spread is primarily responsible for reduction of contrast as the rotation rate increases. If transverse velocity is neglected, then $\delta_{12} = 0$ and the expression for the number of atoms (for a particular velocity v) detected in the $F = 4$ state is as follows:

$$
P_e = 2 \left(C_{\pi/2} C_\pi S_{\pi/2} \right)^2 \\
+ (S_\pi)^2 \left[\left(C_{\pi/2} \right)^4 + \left(S_{\pi/2} \right)^4 - 2 \left(C_{\pi/2} \right)^2 \left(S_{\pi/2} \right)^2 \cos(\Phi_\Omega + \phi_1 - 2\phi_2 + \phi_3) \right] , \quad (4.40)
$$

where C or S represents $\cos(\Omega_{eg}\tau/2)$ or $\sin(\Omega_{eg}\tau/2)$ respectively, and the subscript denotes whether beam intensity was nominally adjusted for a π or $\pi/2$ pulse for atoms with the most probable velocity. Recall that for a π pulse, $\Omega_{eg}\tau = \pi$. The pulse area varies with atom velocity, because the time of flight through the Raman beam is $\tau = w_0/v$. In the limit of perfect pulse area (monochromatic velocity), $C_\pi = 0$, $S_\pi = 1$, and $C_{\pi/2} = S_{\pi/2} = 1/\sqrt{2}$, and therefore Equation 4.40 reduces to the usual

form for the case of perfect contrast (no background atoms):

$$P_e = \frac{1}{2}[1 - \cos(\Phi_\Omega + \phi_1 - 2\phi_2 + \phi_3)], \qquad (4.41)$$

with the Sagnac shift denoted by Φ_Ω.

For the final calculation including transverse velocity, δ_{12} cannot simply be set to zero, since it is proportional to $\boldsymbol{k}_{\text{eff}} \cdot \boldsymbol{v}$. Therefore, the general Raman transition equations were used in the actual computer model. A comparison of the model with experimental results is shown in Fig. 6.3.

Chapter 5

Apparatus

5.1 Overview

A diagram of the experimental setup is provided in Fig. 5.1. Briefly, counterpropagating cesium atomic beams in an ultra-high-vacuum (UHV) chamber (shown in Fig. 5.3) are transversely cooled, and optically pumped into a particular ground state before entering the interferometer region. There, three pairs of stimulated Raman transition lasers serve to divide, deflect, and recombine the atomic wavepackets. Interference between the two paths through the interferometer allows the rotation-rate dependent phase shift between the paths to be observed by detecting the number of atoms exiting the interferometer in a particular state, as measured by fluorescence from a resonant probe laser. The apparatus measures the relative angular velocity between the inertial frame of the freely falling atoms in the atomic beam, and the lab frame containing the optical table. A uniform magnetic bias field is applied along the axis of the Raman beams throughout the length of the interferometer region, and a two-layer μ-metal magnetic shield is used to protect this region from stray magnetic fields. A photograph of the apparatus is shown in Fig. 5.2.
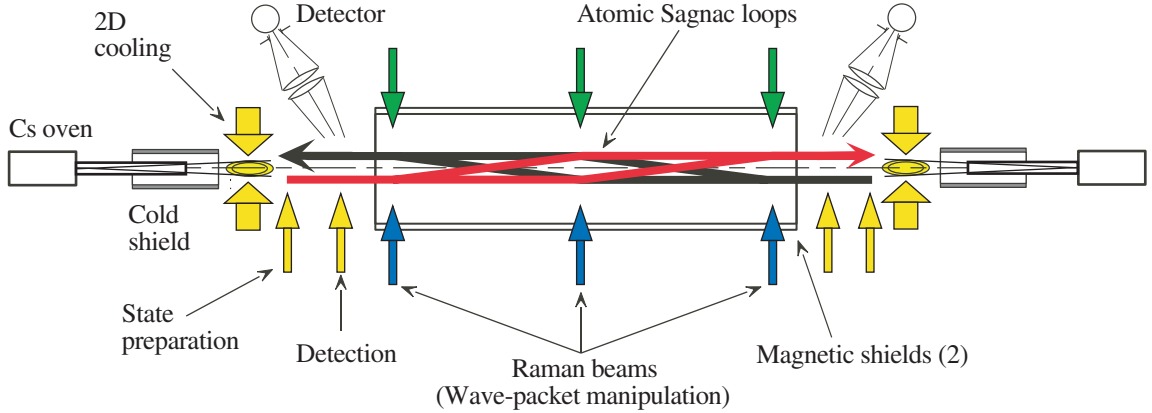
Figure 5.1: Schematic of the apparatus. Reprinted with permission from T. L. Gustavson, P. Bouyer, M. A. Kasevich, "A Dual Atomic Beam Matter-Wave Gyroscope," in *Methods for Ultrasensitive Detection*, Bryan L. Fearey, Editor, Proceedings of SPIE Vol. 3270, 62–9, 1998. Copyright 1998, The Society of Photo-Optical Instrumentation Engineers.

5.2   Choice of atomic source

One of the first choices to make in designing this experiment was the atomic species to use. An alkali atom is an obvious choice since alkalis have an appropriate electronic level structure for laser cooling and trapping. Cesium is convenient, partly due to the availability of high power laser diodes yielding > 150 mW at the 852 nm cesium wavelength. Also, cesium's large mass is advantageous for Doppler cooling, and low transverse velocity spread is important for good Raman transition efficiency. Surprisingly, the mass of the atom used cancels in the expression for the gyro phase shift in our apparatus, since the interferometer area $A = \hbar k_{\text{eff}} L^2 / mv$ is inversely proportional to m (v is the longitudinal velocity). Substituting for A in the expression for the gyro phase shift in Equation 1.4, we find

$$\Delta\Phi = 2\Omega k_{\text{eff}} L^2 / v \,. \tag{5.1}$$

Another fundamental experimental design decision was between the use of fast or slow sources of atoms. We contemplated using either a transversely cooled atomic beam with $v \simeq 300$ m/s, or cold atoms from a magneto-optical trap (MOT), launching

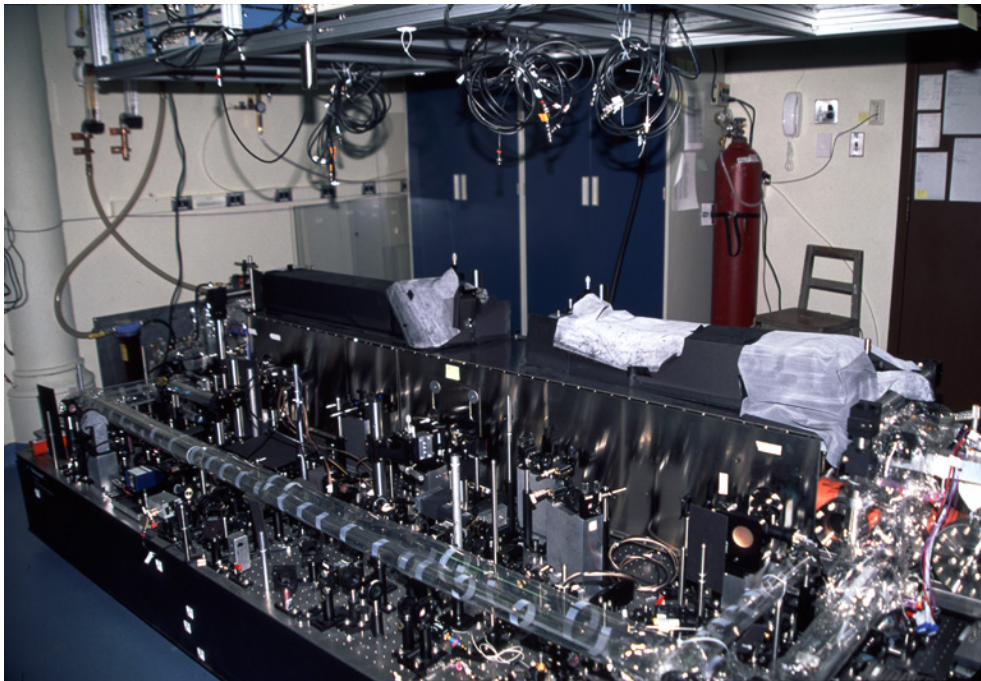Figure 5.2: Photograph of the apparatus. This side of the optics table contains the laser locks and Raman retroreflection optics. Most of the vacuum chamber is hidden from view by the magnetic shield. (This photo was taken immediately after lowering the chamber to the floor, so all cables are disconnected, and the acrylic enclosure that reduces air currents has been removed.)

atoms horizontally down the chamber at $v = 10$ m/sec. At first glance, using cold
and slow atoms from a MOT appears to be advantageous, since slow atoms give
larger rotation-induced phase shifts. From Equation 5.1, we see that $\Delta\Phi \propto 1/v$ for
Coriolis acceleration, so for the parameters described above, the MOT would yield
a factor of 30 larger phase shift. In addition, the MOT could potentially yield a
more homogeneous velocity distribution that would improve contrast and increase
the number of observable fringes.

We initially experimented with launching atoms from a MOT, though we even-
tually decided to use an atomic beam. To launch atoms from the MOT, we formed
a moving molasses by imposing a frequency difference on opposing pairs of beams
in the 3-D optical molasses beams from the MOT, a technique previously used in
atomic fountain experiments [93]. Atoms reach equilibrium at a velocity such that
Doppler shifts cancel the frequency difference between the beams, providing an effec-
tive means to accelerate the atoms. However, the minimum usable launch velocity
is limited by practical complications due to the parabolic trajectory due to gravita-
tional acceleration. For a horizontal launch in a symmetric parabola across our 2 m
interaction region at 10 m/s (requiring an initial vertical velocity of ~ 1 m/s), the
atoms rise and then fall ~ 5 cm. This required the center of the vacuum chamber
to be raised, and complicates generating a uniform bias field. Note that in vertical
atomic fountains, launch velocities are typically several times smaller. It proved to
be difficult to accelerate atoms to the high launch velocities required without heating
them substantially, given that detuning was limited by available laser power and the
acceleration time was limited by existing window access. Longer launch times would
allow atoms to remain at sub-Doppler cooling temperatures while being accelerated.

Atoms were loaded into the trap and then launched in a pulsed sequence at up to
~ 3 Hz. However, the pulsed launch typically only yielded a flux of $\sim 10^8$ atoms/sec
versus $> 10^{11}$ atoms/sec from an atomic beam. The improvement in signal-to-noise
due to the larger atomic beam flux more than compensates for the intrinsic sensi-
tivity difference between the fast versus slow atom velocities. Also, using an atomic
beam allows a continuous gyro signal output with ~ 100 Hz bandwidth rather than
the few Hz achievable with a pulsed MOT. Continuous operation is more convenient

for alignment and optimization of parameters, and is essential for some applications unless another instrument, presumably with lower sensitivity, is used as a flywheel. Finally, using an atomic beam is advantageous because it is extremely stable in comparison to a launched MOT, since launch parameters are highly sensitive to details of the MOT alignment and magnetic fields, and vary from shot to shot. The higher bandwidth of the atomic beam allows high frequency noise (from platform vibrations, for example) to be averaged quickly, whereas with the pulsed MOT, high frequency noise is aliased at the measurement frequency and is more difficult to average out.

An additional difficulty in using slow atoms for rotation measurements is that the acceleration sensitivity scales like $T^2 \propto 1/v^2$ and is greatly enhanced for slow atoms. Though acceleration can be rejected through the use of counterpropagating atomic beams (discussed in section 6.4), increased acceleration sensitivity would increase rotation rate measurement error to the extent that common mode rejection does not work perfectly.

Continuous atom sources based on cold atoms from either a standard MOT [94] or a 2D-MOT [95] have also been developed. For example, the 2D-MOT described by Dieckmann *et al.* achieved a flux of 9×10^9 rubidium atoms/sec, with most probable velocity of 8 m/sec. Since rotation sensitivity is proportional to $1/v$ and signal-to-noise is proportional to $\sqrt{N}$, the short-term sensitivity using this source should be 10 times better than with our current beam design, though the slow beam suffers from many of the deficiencies mentioned for the pulsed MOT. Nonetheless, this technique may be useful in the future.

In the implementation of our atomic beam, we use transverse laser-cooling to improve collimation. Alternatively, one could use mechanical slits to collimate the atomic beam, but that would greatly reduce the flux. In principle one could also use longitudinal cooling techniques (for example, see [96]) to narrow the velocity spread of the beam and improve contrast; however, this would reduce flux too much to justify the additional complexity. In fact, the contrast envelope due to the longitudinal velocity spread is helpful for determining the absolute zero rotation rate, as will be seen in section 6.4.

5.3   Vacuum system

The experiment must be carried out in an ultra-high vacuum (UHV) environment so that cesium atoms are not perturbed by collisions with background gas during their transit time across the apparatus. The vacuum chamber consists of a 3 m long tube of 4" diameter, with standard knife-edge vacuum flanges welded onto the sides and ends for attaching windows, pumps, and ovens, as shown in Fig. 5.3. The chamber was constructed with type 304 stainless steel, which is relatively non-magnetic and is easily welded. The vacuum is maintained by a Varian Turbo V-250 turbomolecular pump (250 l/s, 6" diameter inlet) at each end of the chamber, and the pumps are backed by a shared roughing pump (Edwards RV3). The chamber is mounted on a support stand resting on the floor to prevent vibrations from the vacuum pumps from coupling to the optical table. In addition, the roughing pump and hoses are isolated with sorbothane rubber pads to reduce vibrations transmitted to the floor or vacuum chamber. A cold finger near each oven provides a place for cesium vapor to condense, which is particularly important when baking the chamber. They are maintained at about 0°C by a stack of two water-cooled thermo-electric coolers (TECs).

A cantilever bridge structure was built over the support bed to add stiffness and reduce bending due to the weight of the chamber. The chamber includes two bellows segments, which allow the center of the chamber to be raised, approximating a parabola. This feature would have been necessary had slow atoms been used, due to the greater influence of gravity during their longer time of flight, but was not needed for the atomic beam configuration we used. The chamber and its immediate supports weigh ~ 180 kg (excluding the vertical supports and external magnetic shield).

5.3.1   Window seals to UHV flanges

All the windows on the chamber were sealed to standard stainless knife edge vacuum flanges by a technique developed for this apparatus using standard OFHC copper vacuum gaskets with a knife edge machined on one side [97]. The copper knife edge deforms against the glass to form a seal between the copper and glass and the stainless flange knife edge seals against the copper gasket in the usual manner. A diagram is
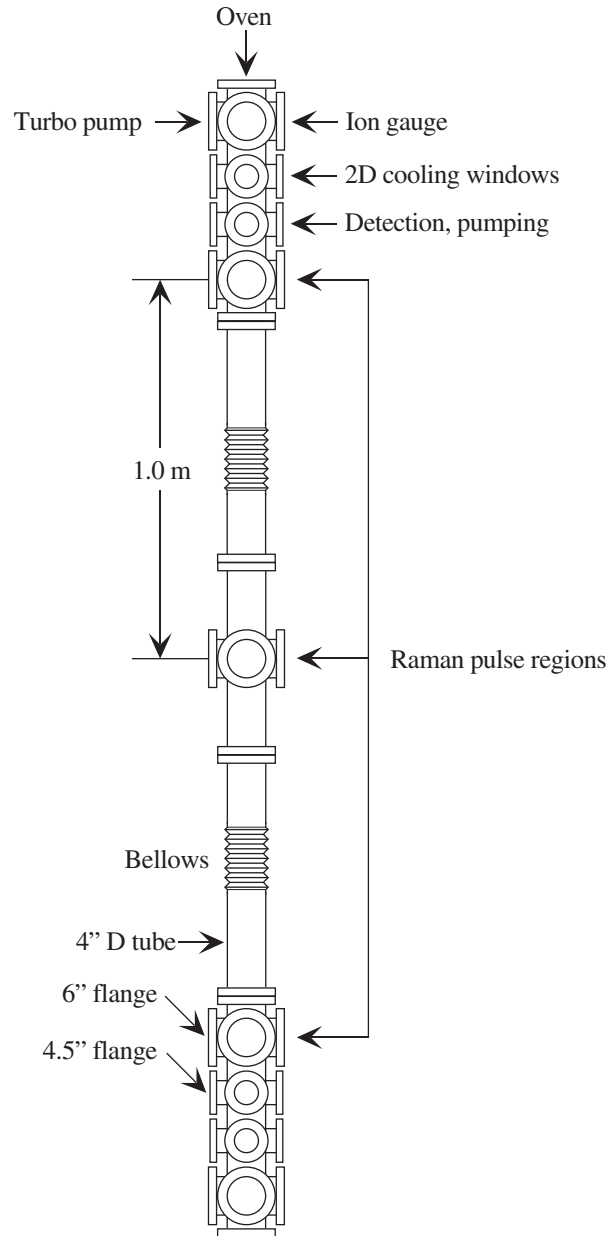
Figure 5.3: Vacuum chamber, top view (scale $\simeq$ 1 : 20). The system is symmetric about the center of the chamber, but for clarity, only one pump, gauge, oven, etc. is labeled.
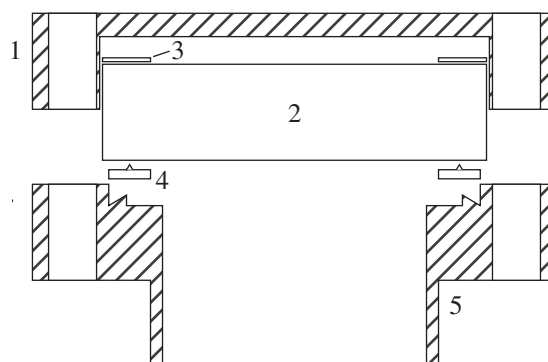
Figure 5.4: Knife edge window seal, shown in cross-section. A knife edge machined on one side of a standard copper gasket allows a window to be sealed to a standard conflat vacuum port. 1) Modified rotatable flange retaining ring, 2) glass window, 3) 0.01" mylar shim, 4) machined copper gasket, and 5) stainless knife edge vacuum flange. Reprinted with permission (with minor modifications) from A. Noble and M. Kasevich, "UHV optical window seal to conflat knife edge," *Review of Scientific Instruments* **65**, pp 3042–3, 1994. Copyright 1994, American Institute of Physics.

given in Fig. 5.4. This sealing technique has the advantage that high quality optical flats can be sealed at minimal cost and without the distortion associated with a brazed seal, yielding excellent wavefront quality. Stress induced birefringence is minimal, and caused 0.01% of incident light to pass through crossed linear polarizers. A cushioning shim is required to ensure uniform force on the glass from the metal clamping plate, and rings of mylar (0.010" thick) or of aluminum foil (20 layers of 0.001" thick foil) were used with success. Mylar melts at 254°C, so the foil may be a better choice for high temperature bakes of small windows. The mylar was more satisfactory because the aluminum foil was prone to creases and tears upon cutting. The copper knife edge must be carefully machined to a sharp edge, as any flat spots will increase the force needed to achieve a seal and this may lead to cracking when the window is baked. State preparation and detection windows are 3.2" diameter, sealed to 4.5" flanges (14 windows total); Raman windows are high quality 2" diameter by 0.5" thick $\lambda/20$ flats, sealed to 6" to 2.75" reducing flanges (6 windows total). All windows used have anti-reflection coatings for $< 0.25\%$ reflection per face at 852 nm. Two-inch diameter windows sealed with the knife edge technique are extremely robust and test pieces have been successfully baked up to 250°C. The larger windows are more susceptible

to cracking during baking, but are no problem for this apparatus, since the window temperatures were typically kept below $< 50°$C during bake-out. The windows are compressed until they just seal by monitoring with a helium mass-spectrometer leak detector. With the 4.5" flanges, the knife edge position is near the edge of the 3.2" windows, so the knife on the copper gasket was offset slightly to avoid pressure within 0.1" of the edge of the window, which sometimes led to cracks. (The window already had the largest diameter that was easily accommodated by the retaining ring and bolt circle.) The offset between copper and stainless knife edges causes the gasket to twist when compressed, and care must be taken that the edge does not hit the glass or form a virtual leak. An alternate approach would be to use indium seals ($155°$C melting point), which might be preferable for larger windows if higher baking temperatures were required.

5.3.2   Vacuum bake-out

Heating pads glued to the main cylinder of the vacuum chamber were used to bake the chamber. (The pads are wired in series in three groups such that the temperature of the center and two end regions can be controlled using three adjustable voltage transformers.) When breaking vacuum, the chamber was vented with argon, and after re-evacuating, the chamber was typically baked for a few days, with the chamber wall in the central region from 70-80$°$C and the wall temperature of the end regions at 45$°$C. The windows typically were only $\sim 35°$C since the windows were only heated indirectly via the main tube, and as a matter of convenience, the chamber is only thermally insulated by the external magnetic shield, which does not extend over the detection windows. This baking technique is conservative in that the windows are heated only minimally, so there is no danger of cracking a window, yet it was sufficient to achieve the desired vacuum. Ideally, the windows should be heated at least as much as the chamber walls so that no material is baked on to the windows. In practice, this didn't appear to be a major problem. The chamber was also baked on some occasions when the ovens had been run at excessive temperatures, and cesium vapor had built up in the detection region. With the ovens cold, the system reaches a base

pressure of $\sim 8 \times 10^{-10}$ torr and under normal operation the pressure is $\sim 2 \times 10^{-9}$ torr. (To convert to SI units of pressure, recall that 1 Pa= 7.5×10^{-3} torr.) The gyroscope can be operated at an order of magnitude higher pressure, but beyond that the oven flux begins to decrease, presumably due to collisions within the long oven tubes (described in the next section), which are not differentially pumped.

5.4 High brightness recirculating oven

The cesium source is of critical importance for our gyroscope, and we have experimented with the design, now on its third revision, to improve reliability and to optimize flux (atoms/sec), brightness (atoms/sec/ster), and operating lifetime. Our current oven has a recirculating design for increased operating lifetime. This design is relatively straightforward to implement, and a similar principle has been successfully used elsewhere for rubidium [98]. The following gives a detailed account of our current design which has also been discussed in [99].

The flexibility of the Raman technique is such that we can readily accommodate atomic beams with various diameters and collimations. Our Raman beams are applied transversely to the atomic beam, and are expanded to 1.3 cm diameter, resulting in only $\sim 10\%$ intensity fluctuations over the ~ 4 mm diameter atomic beam. Since the Raman beam pulse time is determined by the time-of-flight of an atom through the beams, we can apply narrower Raman pulses to broaden the transition linewidth, allowing us to address atoms with larger transverse velocities (limited by available laser power). The dimensions of our oven were chosen to give the collimation that maximized the number of atoms addressable by our Raman beams after transverse cooling. We estimated that a $\sim 60 : 1$ length to diameter aspect ratio would be optimal because it was the minimum collimation required to match the capture range of our 2-D transverse laser-cooling, maximizing the usable flux of atoms.

The primary component of our oven is a tube of type 304 stainless that is ~ 30 cm long and has a 4.5 mm ID as shown in Fig. 5.5. The oven length was determined partly to achieve the required collimation and partly due to constraints imposed by our vacuum chamber. We wanted the transverse cooling region as close as possible to
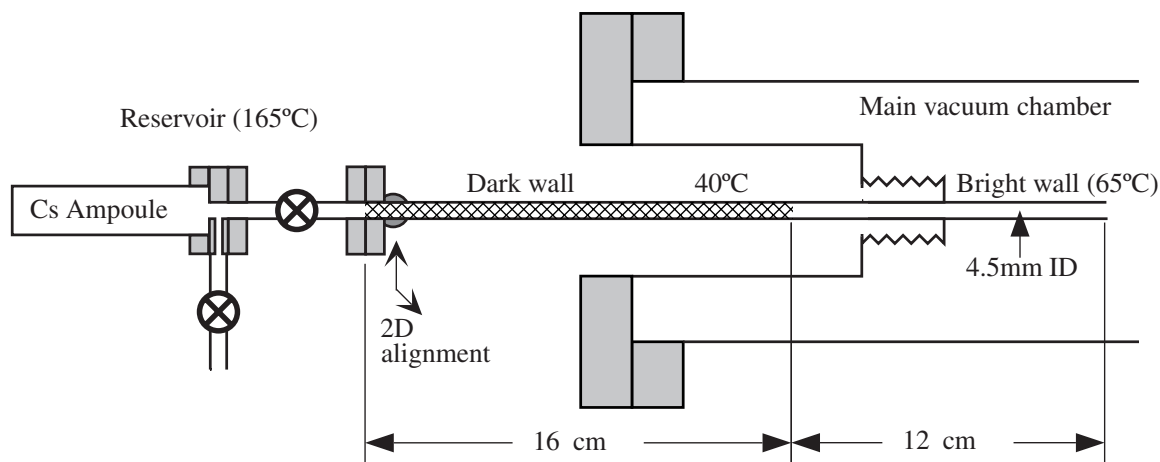
Figure 5.5: Diagram of the recirculating oven design, shown in cross-section. The cross-hatched region represents the fine stainless mesh in the dark wall region (40°C) and a temperature gradient causes cesium to wick back to the hotter reservoir (165°C). The bright wall region (65°C) improves collimation. The oven flux is $\sim 1 \times 10^{11}$ atoms/sec after transverse laser-cooling. For clarity, the oven pointing control 2D stage and mounting brackets have been omitted, along with copper blocks used for thermal transfer to the oven tube. Reprinted with permission from T. L. Gustavson, P. Bouyer, M. A. Kasevich, "A Dual Atomic Beam Matter-Wave Gyroscope," in *Methods for Ultrasensitive Detection*, Bryan L. Fearey, Editor, Proceedings of SPIE Vol. 3270, 62–9, 1998. Copyright 1998, The Society of Photo-Optical Instrumentation Engineers.

the end of the oven in order to keep the atomic beam diameter from expanding unnecessarily. Our oven has three distinct sections: *reservoir*, *dark wall*, and *bright wall*, where we have borrowed concepts and terminology from the atomic clock community [100].

The oven is loaded by inserting a glass ampoule containing 5 gm of Cs into a thin-walled stainless tube that is isolated from the main chamber by a stainless valve (Nupro). A vent valve allows the ampoule holder to be pumped out so that cesium can be reloaded while the main chamber is kept under vacuum. After pumping out the ampoule holder with an external pump, a machinist's vice is used to crush the ampoule. The ampoule holder and valve tubing leading to the main oven together constitute a cesium reservoir, and are heated to 165°C with resistive heater wire, using separate temperature control servos (Wavelength Electronics RHM-4000).

The first half of the oven tubing nearest the reservoir has a fine mesh wrapped inside to wick cesium atoms from the walls toward the higher temperature reservoir. The mesh is stainless type 304 screen with 270 wires/inch and 0.0014" diameter wires, wrapped in an overlapping spiral along the walls of the stainless tubing. (No extraordinary measures were taken to prepare the mesh before installation, though it was cleaned ultrasonically with acetone followed by methanol. In contrast, see [101] for the extensive surface preparation required for sodium.) This recirculating mesh or dark wall region is kept at ~ 40°C, just above the cesium melting point of 28°C. The relatively cool wall temperature in the dark wall region keeps cesium vapor emission from the walls low, and prevents collisional losses, which can greatly reduce beam flux through such a long tube. Though our design does not permit direct observation of cesium wicking, others have reported cesium wicking using this type of mesh [102]. The dark wall portion of the oven tubing is temperature-controlled by a water-cooled thermo-electric cooler (TEC) that is mechanically coupled to the stainless tubing by a copper block near the bright wall region. Since the temperature is controlled at the far end of the dark wall and the reservoir, a gradient can be established across the dark wall. The dark wall temperature is actively controlled by a proportional and integral gain servo (Wavelength Electronics MPT-2500).

Following the dark wall region is the bright wall region at the end of the oven tube, which is maintained at 65°C. This section is intended for additional collimation and is kept hotter to prevent cesium from accumulating on the walls. The end of the bright wall region is just outside the main vacuum chamber and is heated by cartridge heaters coupled to the stainless with a copper block.

A welded bellows seals the oven tube to the end of a 3.5" long 2" diameter tube welded onto a larger vacuum flange, recessed into the chamber. The recession allows access for heaters and avoids excessive oven length while keeping the end of the oven as close as possible to the collimating transverse cooling light described in section 5.4.1. A 1.33" conflat flange was welded to the reservoir side of the oven tubing, after a brass ball with a hole drilled through it was slid over the tubing to act as a pivot point. Two aluminum semi-circles are clamped over the 2" hole in the center of an x-y translation stage (Newport #406) such that the brass ball is seated on the clamp,

and the tension of the bellows keeps the ball in place. (The aluminum clamps are thermally isolated from the translation stage with mylar.) The translation stage gives convenient orthogonal adjustments for the oven pointing. The oven can be aligned upon installation by aiming an alignment laser down the oven bore and observing the spot at the far end of the chamber. Fine adjustments are then mainly achieved by walking the 2D cooling beams.

We stabilized the temperature of the resistive heater and thermo-electric cooler controlled regions using commercial temperature controllers (Wavelength Electronics models RHM-4000 and TEC-2500, respectively) and monitoring each temperature with multiple thermistors. With the oven insulated with foil and shielded from air currents with an aluminum box, the peak-to-peak oven temperature fluctuations are stabilized to 0.007°C in 1 hour, from which we infer atomic number fluctuations of $\Delta N/N \sim 10^{-4}$, based on the vapor pressure as a function of temperature (see Table E.2).

5.4.1   Transverse cooling

After leaving the oven, the atomic beam is transversely cooled in a two-dimensional optical molasses [103]. (This technique was first used for an atomic beam in [104].) The distance between the oven nozzle and the beginning of the cooling light is about 5.5 cm. A laser tuned to the red of the cesium $F = 4 \rightarrow F' = 5$ transition is linearly polarized and retro-reflected with crossed linear polarization. The cooling light is expanded with an anamorphic prism pair to 1.9×4.5 cm² before being divided by a 50-50 beamsplitter to provide light for cooling both atomic beams, and is split again for separate vertical and horizontal cooling. A comparison of various laser beam sizes used in the experiment is shown in Fig. 5.6. Three Helmholtz bias coils driven by quiet current supplies (HP-3610) were used at each end of the chamber to zero the magnetic field in the transverse cooling regions.

Cooling efficiency depends on intensity and detuning. In practice, the intensity was set to maximum and the detuning was varied for optimal cooling. However, the optimal detuning was found to vary with the linewidth of the laser used. The
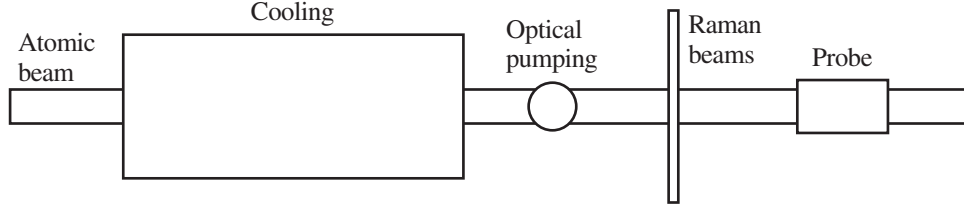
Figure 5.6: Laser beam sizes compared with the atomic beam. (Drawn approximately full scale.) For the Gaussian Raman beam, the $1/e^2$ diameter is shown.

peak intensity was 12 mW/cm^2 before beamsplitters or retro-reflections, limited by available laser power, though appropriate beam-shaping optics could have been used to reduce the size of the beams and increase the intensity. A detuning of 10 MHz (1.9 Γ) was optimal when a distributed Bragg reflector (DBR) laser with 3 MHz linewidth was used. Because the laser linewidth was a sizeable fraction of the cooling detuning, we suspected noise might be introduced in the cooling process. The laser lock stabilizes the center frequency of the laser mode, but mode instabilities could lead to enhanced noise. To test this hypothesis, we used an external cavity grating stabilized laser with $\sim$ 200 kHz linewidth, for which the optimal detuning was found to be 3.2 MHz (0.6 Γ). To achieve the required optical power, a 150 mW laser was optically injection-locked to either the DBR or external cavity laser, and the seeded laser copies the spectral characteristics of the master injecting laser, but amplifies the power. The details of the optical injection-locking technique used are discussed in section 5.6.1. We found that the narrower linewidth of the external cavity grating stabilized laser did significantly improve the stability of the detected beam signal.

Since the atoms only spend $\sim$ 150 μsec in the beam, sub-Doppler cooling mechanisms are not dominant, though varying the polarizations changed the number of cooled atoms reaching the detection region by up to 30%. We used Doppler sensitive Raman transitions (see section 6.1) to measure the transverse velocity spread along the horizontal axis and found $v = \pm 11$ cm/sec FWHM. This corresponds to a temperature of $T = 160$ μK, compared to the Doppler cooling limit of $T_D = 124$ μK. The stability of the transversely cooled atomic beam signal was sensitive to air currents so mylar tubes were added around the cooling laser beams. The noise may have coupled
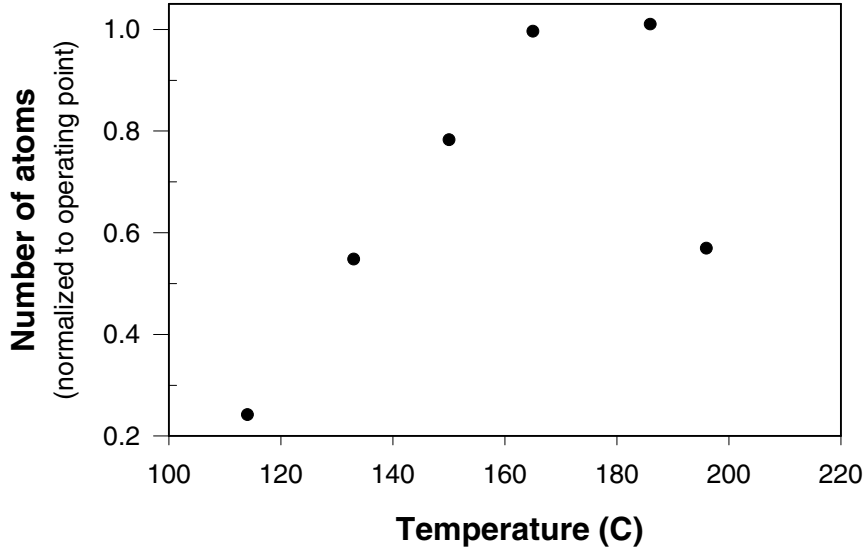
Figure 5.7: Flux vs. oven reservoir temperature. The reservoir temperature was set at 165°C to maximize the flux of atoms. As the temperature is increased further, collisions in the long oven tube begin to scatter atoms, reducing the flux reaching the detection region.

through cooling laser pointing changes due to fluctuations in air density (and index of refraction). An acrylic box enclosing the optical table also helped, though it was primarily intended to reduce phase fluctuations of the Raman beams.

5.4.2   Oven performance characterization

With our standard operating temperatures, the ovens each give a flux of $\sim 1 \times 10^{11}$ atoms/sec after laser cooling, detected at the far end of the apparatus. We used a calibrated CCD camera to image fluorescence from the atomic beam as it passed through a resonant probe laser beam to measure the flux and beam diameter. See section 5.7 for details of the detection system. We measured the atomic beam diameter to be 5.6 mm FWHM in the transverse cooling region, and 2.2 mm FWHM at a distance of 2.6 m from the oven. The reduction in size is presumably due to the finite capture velocity of the transverse cooling. The temperature of the reservoir was determined experimentally to maximize the flux, as shown in Fig. 5.7.
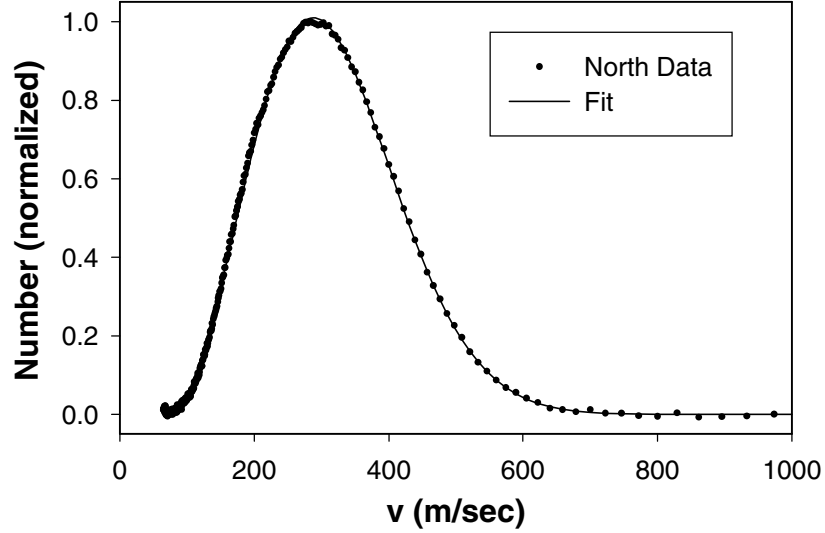
Figure 5.8: Thermal beam longitudinal velocity distribution, as measured by a time of flight method.

We measured the longitudinal velocity distribution by a time of flight measurement. A short pulse of atoms was optically pumped to the $F = 4$ state at a known position and time, and those atoms were detected after they propagated the length of the chamber. The velocity distribution can be computed from the arrival time of the detected atoms and the distance between the pumping and detection regions at opposite ends of the chamber. The optical pumping was done by momentarily switching off the state preparation $F = 4 \rightarrow F' = 4$ light, which was done by switching the rf power to an acousto-optical modulator (AOM). We fit the measured velocity distribution to a generalized form of the usual thermal beam distribution [105]:

$$I(v) = I_0(v - \text{offs})^b \exp\left[-\frac{3}{2}\left(\frac{v - \text{offs}}{v_{\text{mp}}}\right)^2\right], \tag{5.2}$$

where $v_{\text{mp}} = \sqrt{\frac{3k_B T}{2m}}$ is the most probable velocity for a standard thermal beam, $v_{\text{max}} = v_{\text{mp}}\sqrt{\frac{b}{3}} + \text{offs}$ is the measured peak of the distribution, and I_0 is a normalization constant; $b = 3$ and offs $= 0$ for a usual thermal beam. Because slower atoms scatter more photons while passing through the probe beam, we fit the distribution with

$b = 2$. For the North atomic beam,[1] we found $v_{\mathrm{mp}} = 267$ m/sec and offs $= 70$ m/sec, which yielded a detected maximum of $v_{\mathrm{max}} = 287$ m/sec. For the South beam, we found $v_{\mathrm{mp}} = 273$ m/sec and offs $= 75$ m/sec, yielding a detected maximum of $v_{\mathrm{max}} = 299$ m/sec. The reason for a non-zero offset parameter was not studied, but may be due to collisions in the long oven tube (Equation 5.2 is intended for an effusive beam with mean free path greater than the nozzle dimensions) or due to multiple effective source temperatures in the oven. After transverse cooling, the transverse velocity spread of ± 11 cm/sec corresponds to a collimation of 2.9×10^{-7} steradians (a factor of 2.5×10^3 improvement due to the cooling).

The oven lifetime is not well known, as the cesium was sometimes replaced prematurely due to an oven clog or a vacuum break for some other reason. Oven clogging can be caused by imperfect wicking, possibly due to improper temperature gradients across the dark wall region. The ovens run reliably except that after running continuously for one or more days, the flux begins to decrease, recovering completely if the oven is tilted so the reservoir is lowered and then the oven is shaken sharply. More serious oven clogs could generally be cleared by baking the dark wall region while keeping the reservoir hotter than the dark wall to maintain a gradient. A 5 g cesium ampoule should last in excess of 6 months of continual run-time. A redesigned oven with appropriate apertures for collimation and large bore diameter could greatly reduce the likelihood of clogging, and we anticipate upgrading the ovens at some point. Other possible alternatives include the following:

1. *'Candlestick' design* [101]. Though our current recirculating oven design has similarities to this technique, a more compact oven with a better defined source region might prove advantageous.

2. *Effusive oven and cold shield.* This was the second method used for this apparatus, though it was abandoned due to low flux, likely in part due to misalignment of the nozzle and cold shield. However, a larger source aperture and

---

[1]The term *North* refers to the atomic beam from the Northern-most oven (conversely for *South*), but the name is otherwise arbitrary. The gyroscope was aligned nearly North–South at both Stanford and Yale by coincidence; however, this alignment does have the advantage that centripetal acceleration due to the Earth's rotation cancels, as the gyro is only sensitive to acceleration along the Raman beams.

re-engineering the cold shield alignment method could resolve these problems.

3. *Microchannel array* [106]. This approach can yield good performance because the ratio L/d of hole length to diameter is large, yet L is small, avoiding collisions. This type of oven was initially used with this apparatus, but was prone to clogging. However, this method could work well with more careful thermal engineering to ensure a temperature gradient perpendicular to the face of the array.

The oven design in our apparatus is greatly complicated by the distance between the oven mounting flange and optical access for the transverse cooling. Redesigning the end sections of the chamber to exchange the turbo pumps and cooling windows would solve this problem.

5.5 Magnetic fields

Magnetic fields in the interferometer region will produce first order Zeeman ground state energy level shifts of the form $\sim m_F \mu_B B$ that cause a relative shift between the two ground states of:

$$\Delta\nu_{\mathrm{hfs}} = m_F \times 700.8 \text{ kHz/G} . \tag{5.3}$$

We can eliminate the first order Zeeman shift by using $m_F = 0$ atoms; however, in this case, we are still sensitive to the second order Zeeman shift of:

$$\Delta\nu_{\mathrm{hfs}} = 427.5 \text{ Hz/G}^2 . \tag{5.4}$$

(These shifts can be calculated using the Breit-Rabi formula, given in standard texts such as [65].) Variations in the field between the two interferometer paths or along the length of the interferometer will result in a spurious interferometer phase shift. To select only atoms in the $m_F = 0$ state, we must define a quantum axis by applying a magnetic bias field horizontally, in the direction of the Raman beams, throughout the length of the interferometer interaction region. The bias field strength must be
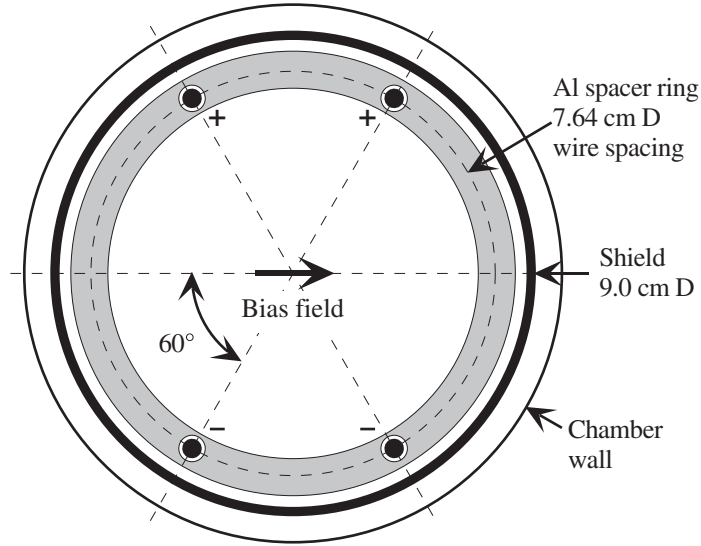
Figure 5.9: Uniform magnetic bias field generation. Cross-section of 4 bias wires (small black circles), aluminum spacer ring, magnetic shield, and vacuum chamber.

sufficient to shift the Zeeman sublevel energies apart by an amount comparable to the Doppler sensitive Raman transition linewidth, or about 300 kHz, otherwise the Raman transitions will not address only $m_F = 0$ atoms. The peak spacing can also be used to measure the magnetic field applied, using Equation 5.3. These peak spacings will be shown later in Fig. 6.1.

The bias field is generated by four 1/8" diameter aluminum wires running inside the length of the main vacuum chamber. The bias wires are placed at vertices of a rectangle concentric with a cylindrical magnetic shield inside the chamber, as shown in Fig. 5.9. The magnetic shield and bias wire arrangement are based on a design used for atomic clocks [107]. The shield is designed to eliminate stray fields from the interaction region, and image currents due to the shield make the bias field more homogeneous. The bias wires are held by a series of aluminum spacer rings inside the shield, with ceramic insulators attached by TorrSeal epoxy preventing electrical contact. Electrical connection is made by mechanical connection to a UHV electrical feedthrough with ceramic to metal seals, rated at 15 A. Aluminum spacer rings outside the shield hold the shield and bias wire assembly centered in the vacuum chamber. The shield starts after the detection window, and has end-caps (with openings to allow

the atomic beam to pass) to improve the field at the first Raman pulse. Because the chamber was originally designed to bend at the bellows, the shield is in three major sections with articulated joints at the bellows. (The middle section was actually made in three pieces with tight slip-fit joints.) The shield also has six 2" diameter openings to allow access for the Raman beams. We measured the field inside the shield using a 3-axis magnetometer (Applied Physics Systems, CA) with milliGauss resolution. The field was < 1 mG except at the joints in the shield, where the field along the longitudinal axis reached ~ 70 mG even after wrapping flexible μ-metal foil around the joints to reduce field leakage. Now that we do not intend to bend the chamber, a monolithic shield could be used and would greatly improve the field uniformity. Though the state preparation and detection regions are quite sensitive to magnetic fields, so much optical access is required there that it was deemed impractical to extend the shield that far. Typically the bias current is I=3 A, corresponding to a magnetic field of 1.10 Gauss, a first order Zeeman shift of 771 kHz for $m_F = 1$, and a second order Zeeman shift of 518 Hz for $m_F = 0$ atoms. Better bias field uniformity could be achieved by using more than four bias wires [108], but currently this is not a limitation.

5.6 Laser locks

A distributed Bragg reflector (DBR) laser with 100 mW output power (SDL[2] 5712-H1) is referenced to a cesium transition using a frequency modulation saturated absorption lock, and the laser frequencies for transitions from the $F = 4$ ground-state are derived from this laser. Note that all diode lasers used in the experiment are collimated with an antireflection-coated microlens (2 mm focal length) and protected against feedback by one or more optical isolators, each with > 35 dB attenuation. The lasers are controlled by self-made current and temperature controllers[3] which are stable to ~ 100 nA/$\sqrt{\text{Hz}}$ rms and ± 1 mK respectively.

---

[2]SDL Inc., San Jose, CA

[3]The current controller is based on a published circuit design by Libbrecht and Hall [109] and the temperature controller uses a JILA design implemented by Brent Young.

Figure 5.10: $F = 4$ laser lock schematic.

To implement the lock, a Fresnel beamsampler splits 1.4 mW from the main laser output for use in the lock, and this light is divided into pump and probe components. The pump and probe beams are overlapped and counterpropagate through a cesium cell, as shown in Fig. 5.10. The probe passes directly through the cell and onto a photodiode, while the pump is double-passed through an AOM to frequency modulate the beam before entering the cell. The pump AOM down-shifts the carrier by 2×60 MHz with a frequency modulation dither at 312.5 kHz, using rf generated by the doubled output of an HP8770A arbitrary waveform generator, referenced to a stable 10 MHz reference. The cesium cell is magnetically shielded to avoid Zeeman shifts, which would cause an offset in the lock frequency.

The main laser frequency is at 60 MHz above the 3/5 cross-over line to which we lock. To see this, recall that saturated absorption spectroscopy avoids Doppler broadening because when irradiating the cell with a counterpropagating pump and probe laser, only one longitudinal velocity class of atoms is in resonance with both beams at once. The pump beam optically pumps the resonant velocity class of atoms

into the $F = 3$ state, allowing the probe beam to pass through with reduced absorption since atoms resonant with the probe have already been optically pumped. A cross-over resonance works similarly, except the lasers are tuned half way between two excited state transitions such that a particular velocity class Doppler shifts one laser up and the other down so that the lasers are on resonance with different lines. Consider a velocity class of atoms in the cell that moves along the laser beams and sees the probe Doppler shifted by $-\Delta \nu$ and the pump shifted by $+\Delta \nu$. If ν_L is the laser frequency and $\nu_{\text{AOM}} = 60$ MHz is the frequency shift of the AOM, then for the two laser beams to address the same atoms, we must have:

$$\nu_L - \Delta \nu = \nu_L - 2\nu_{\text{AOM}} + \Delta \nu \,. \tag{5.5}$$

Then we have $\Delta \nu = \nu_{\text{AOM}}$ and for our lock point, $\nu_L = \nu_{3/5} + \nu_{\text{AOM}}$. To tune onto the $F = 4 \rightarrow F' = 5$ transition for the detection laser, we pass light from the main laser through an AOM double-pass for a 2×83 MHz up-shift. See Fig. 5.11 for a diagram of the energy levels and frequency shifts used. A detailed account of cesium saturation spectra can be found in [110]. Light for the transverse cooling is treated the same way, but up-shifted by only 2×81.3 MHz to make the light slightly red-detuned. Because the cooling requires substantial laser power, we use a small amount of power from the DBR laser, ending up with $\simeq 400$ μW after the double-pass, and optically inject a 150 mW standard (non-DBR) diode laser (SDL 5422-H1).

A separate DBR laser is locked with a saturation absorption setup for the $F = 3$ laser. It is locked to the 2/3 cross-over and a 94.5×2 MHz AOM up-shift produces $F = 3 \rightarrow F' = 4$ light for the cooling repumper. This lock is not as critical, and the laser linewidth and lock bandwidth are not an issue.

5.6.1   Vortex injection lock

For the $F = 4$ laser lock, we originally used a DBR laser with 3 MHz linewidth, but suspecting that the DBR linewidth might introduce noise in the cooling process, we narrowed the linewidth by optically injection-locking the DBR with a 200 kHz linewidth commercial diode laser, an external grating stabilized *Vortex* model from
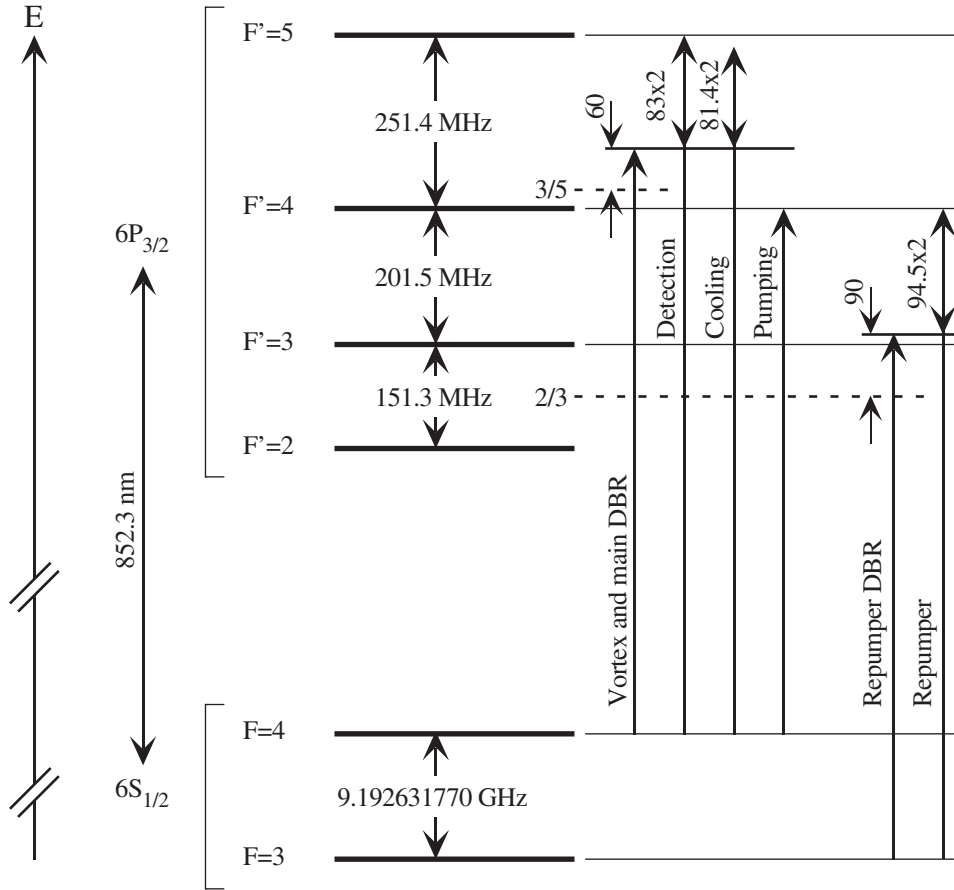
Figure 5.11: Cesium transition spacings and AOM frequency shifts. The main laser used to generate frequencies from $F = 4$ is referenced to the 3/5 cross-over, and the repumper is referenced to the 2/3 cross over. An AOM is used to frequency shift light for each of the detection, cooling, pumping, and repumper beams.

New Focus Inc., CA. Optical injection of light from the Vortex into the DBR laser narrowed the linewidth of the DBR while copying the phase and frequency of the master laser.[4] The light was coupled in through the output ports of an optical isolator from Optics For Research (OFR), and this technique allowed us to utilize the existing laser lock setup (and quickly switch between configurations). The only other necessary change was to the lock electronics, since with the injection, the error signal corrections must be applied to the Vortex. We typically operated the Vortex at 3.4 mW (its maximum power is 5 mW), of which < 1 mW was diverted for the injection lock. This was more than enough power for a robust lock with a large injection range. In fact, too much optical power (more than about 100 μW coupled into the laser) can lead to a narrower injection range, as optical power can transfer to relaxation sidebands, as studied in [113].

5.6.2   Lock electronics

The lock electronics are constructed as follows: The photodiode is ac coupled with an integrated amplifier, which was found to be necessary to avoid being limited by technical noise of the detector itself. The photodiode signal was amplified again with a MiniCircuits ZFL-500 amplifier and limiting Zener diodes to ground were added before the mixer that followed (MiniCircuits ZFM-3). The diodes allow maximal gain when locked to the center of the line by clipping the large peaks of the saturation absorption signal that could damage the mixer. The increased gain yields a steeper slope of the lock derivative signal, resulting in a tighter lock [114]. The signal was mixed with a local oscillator at the 312.5 kHz FM frequency, and the demodulated signal from the mixer gives a derivative of the cesium transition line-shape. The FM frequency was optimized experimentally by maximizing the slope of the lock derivative signal. The mixer output is fed into a proportional and integral gain box that outputs corrections to the Vortex laser. The PI box buffers the input and connects it to a high bandwidth error monitor op-amp and separate op-amps for proportional and integral gain. The proportional and integral signals are summed together with an adjustable

---

[4]Optical injection locking was first demonstrated in [111], and the phase relationship between the master and slave was established in [112].
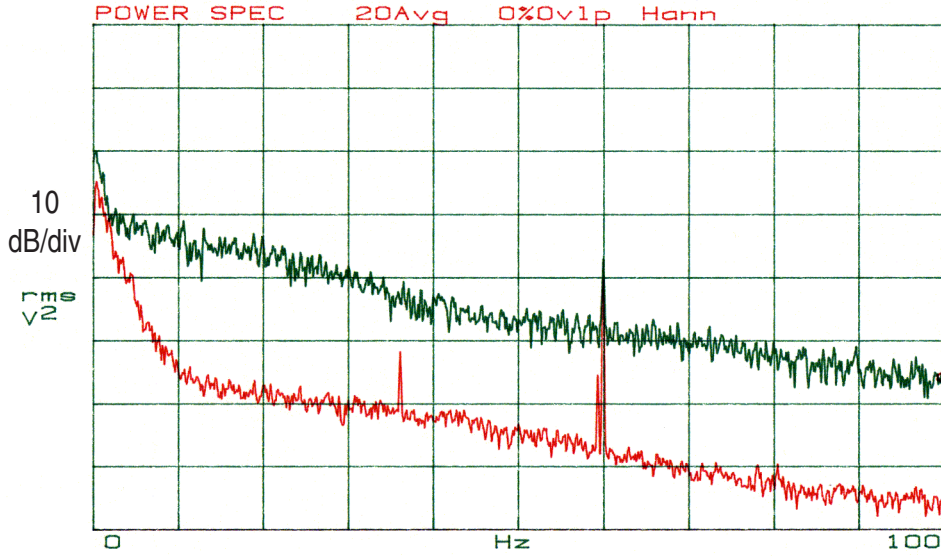
Figure 5.12: Laser lock improvement. The upper trace shows the power spectral density of the lock error signal with the original DBR laser, and the lower trace shows the quieter error signal with the external cavity Vortex laser optically injecting the DBR and new lock electronics.

preset for setting the lock point, and the output is divided into a low bandwidth piezo error monitor, and amplifiers for current and piezo modulation outputs. Frequencies below 0.2 Hz are sent to the piezo control, and the current controller handles higher frequencies. Relative gains were balanced for equivalent frequency response. Care was taken to achieve a large frequency bandwidth ($\sim$ 90 kHz) for this laser lock, since that allows more gain without oscillation and correspondingly reduces frequency noise.

The Vortex laser greatly improved the frequency stability of the cooling and detection light, with noise power of the detected transversely-cooled beam reduced $\sim$ 20 dB by the Vortex lock, and reduced an additional 10 dB by replacing the lock-in amplifier with a mixer (perhaps due to higher modulation frequencies). A comparison of the laser lock error signal with and without Vortex injection is shown in Fig. 5.12. The Vortex has mechanical resonances around 5 kHz that were not completely removed by the lock, but this noise is above the frequency response of the gyroscope, and posed no problem for the experiment. We plan to construct a separate grating-stabilized laser lock and beat it against the Vortex output for an accurate measurement of the

locked Vortex linewidth. By comparing the lock error signal rms fluctuations with
the peak-to-peak voltage of the saturation absorption signal at the lock-point (the
3/5 cross-over peak, with frequency width Γ), we infer a lock linewidth of 1.23 kHz
rms in 1 sec.

Because of the limited range of the current and piezo modulation inputs, the
Vortex laser would typically drift out of range of the lock within a few hours. The
piezo exhibits hysteresis, and was especially prone to drifts after the set-point was
changed, for example when the laser was first locked. Fortunately, the piezo set-point
has enormous range, accessible by front panel or GPIB control. To keep the laser
locked for long periods of time, the offset of the piezo modulation error signal was
monitored by a dedicated computer and a GPIB command was sent to the Vortex
to adjust the piezo set-point when the error signal exceeded a threshold value. The
electronic lock servo had sufficient bandwidth to cope with the glitch caused when the
digital servo loop made an adjustment, so the laser stayed locked. Because the GPIB
bus of the Vortex laser is not well shielded, noise spikes appear on the lock error signal
when GPIB activity occurs on the bus. Therefore, separate GPIB cards were used for
reading the error signal (through an auxiliary input of the GPIB-controlled SR810
that locks the $F = 3$ laser) and for occasional corrections to the Vortex digital piezo
setpoint. The digital servo loop polls the error signal only once every 30 seconds,
which is much faster than the drift of the error signal.

5.7   Detection of atomic flux

Atoms in the atomic beam are detected using a probe laser tuned to the $F = 4 \rightarrow$
$F' = 5$ resonance, as described in section 3.4. Atoms at 300 m/sec scatter approxi-
mately 560 photons while crossing the 1 cm detection region. Considering our detector
quantum efficiency of 0.75, our imaging at $f/D \simeq 2$, and losses for uncoated lenses,
we estimate an average of 5.5 photoelectrons are generated in the detector for every
atom passing through the probe. This means we will be limited by shot-noise fluc-
tuations in the number of atoms rather than the sensitivity of the detection system.
(This estimate neglects other electronic noise that could prevent us from reaching

the atom shot-noise limit.) We calibrated the fluorescent detection by measuring the absorption of the probe beam due to the atoms, which avoids uncertainties in the imaging collection efficiency.

We found that the detection noise was substantially reduced by retroreflecting the probe beam. Otherwise, the scattering force from the probe transfers momentum to the atoms and Doppler shifts them away from resonance. With the retroflected probe, atoms stay on resonance, where the sensitivity to laser frequency fluctuations is only second order. The probe intensity is $I \sim 10 \times I_{sat}$, and power broadening also reduces sensitivity to frequency noise. We also found that sensitivity to intensity fluctuations was reduced with the narrower linewidth laser. With the original DBR lock before retroreflecting the probe, implementing a probe intensity stabilization servo that gave $\Delta I/I < 1 \times 10^{-4}$ had improved detection noise. With the Vortex lock and retroreflected probe, we were not limited by intensity fluctuations even without the servo. (We did not investigate to what extent this improvement came from the narrow linewidth or from a change in the intensity stability after implementing the injection-lock.)

A normalized detection scheme, in which the number of atoms in the $F = 4$ and $F = 3$ states are measured separately, could reduce sensitivity to variation of flux in the atomic beam. This technique was not used, because continuous detection would not be possible with overlapping counterpropagating beams.

The detection photodiodes are Hamamatsu S3590-01 Si-PIN with area of 1 cm^2. The photodiodes were integrated into low-noise amplifier circuits that are described in Appendix A. We reduced the detector bandwidth to 133 Hz, since we can only measure rotation rate changes at frequencies that are lower than $(2L/v)^{-1}$, a natural cutoff frequency set by the transit time of atoms through the apparatus. The detector sensitivity is 10.3 V/μW, which corresponds to a detection calibration of 1 V$= 7 \times 10^{10}$ atoms/sec.
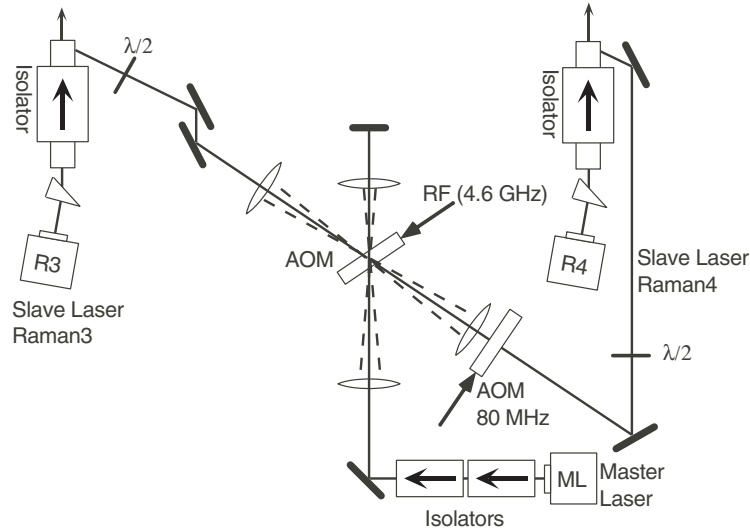
Figure 5.13: Raman laser frequency generation. The +1 and −1 diffraction orders from a master laser retroreflected through a high frequency AOM operating at 4.6 GHz were used to optically injection lock two slave diode lasers, yielding the required 9.2 GHz frequency difference. Reprinted with permission (with minor modifications) from P. Bouyer, T. L. Gustavson, K. G. Haritos, and M. A. Kasevich, *Optics Letters* **21**, pp. 1502–4, 1996. Copyright 1996, Optical Society of America.

5.8 Raman lasers

5.8.1 Microwave signal generation

Achieving stimulated Raman transitions requires two frequency-stabilized laser beams detuned from an optical resonance with frequency difference equal to the cesium rf hyperfine splitting frequency. (The theory of Raman transitions is discussed in section 3.5.) We used an original solution based on optical injection locking, shown schematically in Fig. 5.13. (Optical injection locking was discussed previously in section 5.6.1.) Our Raman beam injection implementation has been described in a separate publication [115], but will be summarized here.

The master laser, a 100 mW DBR (SDL 5712), is focused to a 50 μm waist through a high frequency acousto-optical modulator operating at 4.6 GHz, made by Brimrose (GPF-4600-300-X). The crystal must be specially cut unusually thin so it can be used in a double pass configuration with reasonable efficiency. This allows the light beam

to pass close to the transducer, and allows undiffracted light to exit the crystal cleanly. We take the -1 order from the first pass, then retro-reflect the light by imaging the zero-order beam back on the crystal and take the $+1$ order from the second pass. The diffracted optical power from the AOM is 30 μW using the maximum allowed rf power of 100 mW (20 dBm). The difference between the $+1$ and -1 diffracted orders is the 9.2 GHz cesium clock transition frequency. The AOM has a Bragg angle of $\theta_B = 17.8°$ (the separation angle is twice this) and a diffraction efficiency of only 0.03%. We amplify each diffraction order by optical injection locking two slave diode lasers (SDL 5422-H1), coupling through the escape port of an optical isolator (from OFR). Because the injecting beams have low power, a lens and two mirrors are used to match the transverse modes of the master and slave beams. The master laser frequency is set so the slave lasers are detuned from resonance with the excited state by $\Delta \simeq 2$ GHz. The slave laser that would be on resonance with the $|F = 4\rangle \rightarrow |i\rangle$ level for $\Delta = 0$ will be denoted Raman4, and the laser addressing $|F = 3\rangle$ will be denoted Raman3.

We characterized the beat note between the two slave lasers by overlapping the beams on a fast photodiode, and found that $> 99\%$ of the optical power was in the carrier with the remaining power in the pedestal, as shown in Fig. 5.14. The linewidth of the peak signal was less than the 20 Hz resolution of the spectrum analyzer.

To generate the rf at 4.6 GHz, we use an HP83711B synthesizer, with an external 10 MHz timebase. For a 10 MHz source, we used a temperature stabilized quartz crystal, first from an HP8770A arbitrary waveform generator, but later this was upgraded to an oscillator with $\Delta\nu/\nu = 1.5 \times 10^{-13}/\sqrt{\text{Hz}}$ stability (Oscilloquartz #8607-BGE). This oscillator was adjusted by comparison with a time standard based on GPS (HP-58503A). The GPS time standard has excellent long-term stability, though its short-term stability is inferior to that of the crystal. The crystal oscillator was found to drift by ~ 0.01 Hz in 3 months. To reduce rf noise, the HP83711B synthesizer may eventually be replaced by a frequency chain referenced to the Oscilloquartz.

Because the HP rf synthesizer frequency can only be scanned in discrete steps, we added a separate 80 MHz frequency shifter in the injection locking path for Raman4
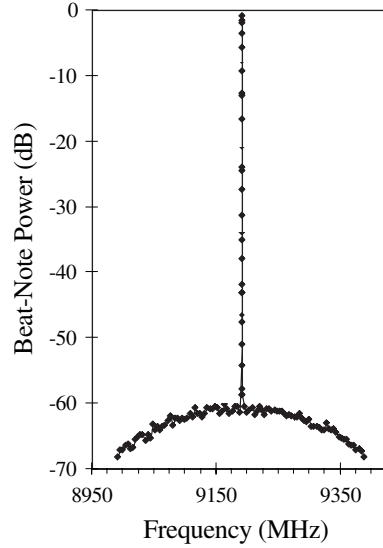
Figure 5.14: Raman laser beat note. The peak frequency is at twice the rf driving frequency, or 9.2 GHz. More than 99% of the power is in the peak. The spectrum analyzer was configured for 10 kHz resolution bandwidth and 64 averages. Reprinted with permission from P. Bouyer, T. L. Gustavson, K. G. Haritos, and M. A. Kasevich, *Optics Letters* **21**, pp. 1502–4, 1996. Copyright 1996, Optical Society of America.

(see Figure 5.13). This allowed us to scan the Raman transition peaks using an arbitrary waveform generator (SRS-DS345, from Stanford Research Systems, Sunnyvale, CA), which was useful during alignment. The high frequency rf synthesizer was offset by 80 MHz to maintain zero Raman detuning.

5.8.2   Optical layout

After the Raman slave lasers are set to the correct frequencies by injection locking, they are combined on a polarizing beamsplitter cube preceded by $\lambda/2$ waveplates to adjust the total and relative Raman intensities. The spatially overlapped Raman beams copropagate through the system so phase fluctuations from air currents largely cancel and Doppler shifts from mirror vibrations are reduced by the ratio of the Raman transition rf wavelength to a single beam optical wavelength, or 2.6×10^{-5}. Due to selection rules, the Raman transitions can only be driven by certain combinations of polarizations, namely crossed-linear, $\sigma_+ - \sigma_+$, or $\sigma_- - \sigma_-$. We must take

care to avoid driving copropagating (Doppler insensitive) transitions in the gyroscope configuration. Originally this was done by adding a $\lambda/4$ waveplate before the vacuum chamber to yield opposite circular polarizations. After the vacuum chamber, another $\lambda/4$ waveplate linearized the polarization and a polarizing cube separated the two Raman beams, allowing us to reflect just one beam back through the chamber. This yielded polarizations of the form $\sigma_+ - \sigma_+$ for the counterpropagating beams, but due to imperfections in the polarizations, residual peaks corresponding to copropagating transitions were still present. With the addition of AOM frequency shifters to the retroreflection optics, described in section 5.8.3, the beam to be reflected is initially detuned from resonance (before retroreflection), so only counterpropagating transitions occur.

A two mirror periscope was used to bring the light up to the level of the atomic beam, 23 cm above the optical table. Eventually the beam delivery to the spatial filter was replaced by an optical fiber, which greatly improved performance by assuring that the Raman lasers were overlapped and had the same mode, eliminating a serious source of alignment error. This improvement is described in section 7.5.1. The spatial filter, beamsplitters and final beam delivery optics are all mounted at atomic beam height to avoid introducing any additional optics after the spatial filter, which could degrade the wavefront unnecessarily. Vibration is a concern for optics mounted high above the table, so these optics are mounted on sturdy aluminum riser blocks with substantial cross-section, typically $> 5 \times 15$ cm^2. To maximize vibration damping, we used a high quality optical table (Newport RS-4000 5 ft $\times$ 10 ft), which was typically floating on pneumatic legs (Newport I-2000).

Spatial filter

The goal of the spatial filter and beam shaping optics is to generate Raman beams with an aspect ratio that is taller vertically than the height of the atomic beam, but narrow horizontally to produce a broad Raman transition linewidth and maximize the number of atoms addressed. The optical layout is shown in Fig. 5.15.

A conceptual overview of the spatial filter setup is presented, and is followed by a more detailed treatment and the alignment optimization procedure. A pair of
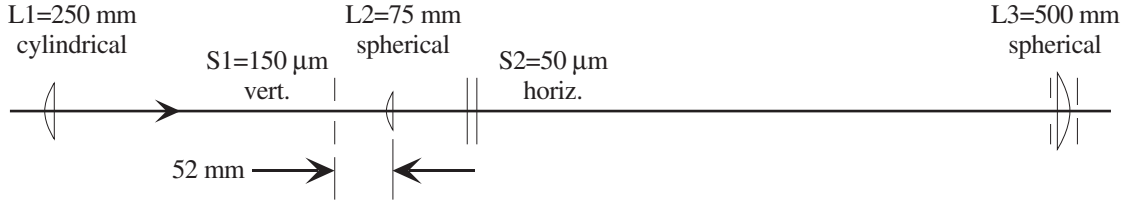
Figure 5.15: Raman laser spatial filter and beam shaping, top view. L1 is a cylindrical lens and S1 is a vertical slit at its focus; S2 is a horizontal slit at the focus of spherical lenses L2 and L3.

spherical lenses with a horizontal slit at the focus form a telescope that magnifies the light and spatially filters it in the vertical direction. A cylindrical lens and vertical slit were added before the first spherical lens to reduce the size of the beam and spatially filter it along the horizontal axis. The system is adjusted so that the output beam is collimated vertically and the horizontal Gaussian beam waist is at the atomic beam, with a vertical to horizontal aspect ratio of 20:1.

To set up the spatial filter, we first set up a telescope to expand the beam with spherical lenses L2 and L3, then added a horizontal slit S2 at the focus of L2. The slits are mounted on 2-axis translation stages on top of tilt stages, to allow angular and transverse adjustments. L1 is on a longitudinal translation stage, and L3 is on a 3 axis stage with a 2 axis gimbal mount. L3 was translated until the beam was collimated vertically, based on a shear plate, a wedged optical flat yielding an interference pattern that rotates depending on collimation. To minimize aberrations, the angle of L3 was adjusted with the gimbal mount to retro-reflect the back-reflected light beam. Then the cylindrical lens L1 was added and roughly positioned, and the slit S2 was rotated to be perpendicular to L1. L1 was translated to put the waist of the output beam $\simeq$ 1.7 m from L3, the distance to the atomic beam. Note that the beamsplitter setup following the spatial filter has been designed so the total path length for the three Raman beams is the same, which is necessary to produce the desired waist sizes at the atomic beam, and has the added virtue that it eliminates laser coherence length effects. Next, slit S1 was added after the cylindrical lens, and positioned for maximum power transmission. Finally, a circular aperture was placed
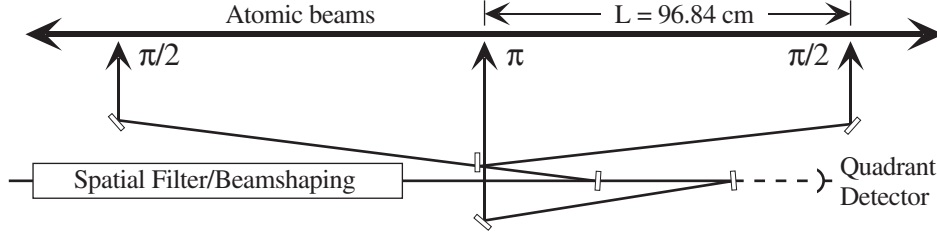
Figure 5.16: Raman laser beamsplitter scheme used to generate the $\pi/2 - \pi - \pi/2$ pulses. Note that the optical path lengths of the three Raman beams were adjusted to be the same. Scale $\simeq$ 1:20.

in front of L3 to block vertical diffraction orders, and a large slit was added after L3 to block horizontal diffraction orders. The resulting beam waists ($1/e$ diameter) are 13.6 mm vertically and 0.64 mm horizontally.

Because parallel rays of light passing through a lens focus at the same point (for paraxial rays, ignoring spherical aberration), parallel rays of light pass through the spatial filter without clearly defining a center position. This led to difficulty in overlapping the two Raman lasers, since simply optimizing the power through the spatial filter did not guarantee overlap. To counter this problem, we mounted quadrant detectors (EG&G #C30845E, 8 mm diameter) at two positions after the spatial filter, with 1 m separation. This allowed us to match the overlap of the Raman beams to $\sim 20~\mu$m at each position, establishing position and direction of the beams. The addition of the optical fiber gave further improvement, as it guaranteed the relative alignment of the two Raman lasers.

Beamsplitters

Beamsplitters are used to divide the Raman laser light into three pulses with intensity ratios 1:2:1 for the $\pi/2$, π, and $\pi/2$ beams respectively, with a separation distance of $L \simeq 1$ m between the $\pi/2$ and π beams. The details of the beamsplitter configuration are shown in Fig. 5.16. A 50/50 beamsplitter is used near normal incidence to divert half the light for the two $\pi/2$ pulses, and the remaining light is used for the π pulse. A second beamsplitter divides light between the two $\pi/2$ beams. Additional mirrors

are required to balance the path length (equal to < 3 cm) and to use the beamsplitters near normal incidence ($\simeq 4°$), which improves the splitting ratio between the polarizations. The beamsplitters are 2" diameter × 12.5 mm thick optical flats[5] with $\lambda/20$ flatness on each face (< 10 arcmin wedge), mounted in Newport 600A-2R optics mounts. These mounts have micrometer controls with 1 μm resolution and 10 cm lever arm, yielding 10^{-5} rad resolution, which was the precision required.

5.8.3   Retroreflection frequency shifts and phase-locked loops

Rotation and Doppler shifts

The Earth's rotation Doppler shifts the Raman beams relative to the inertial frame of the atoms, giving a rotation bias away from the center of the contrast envelope and reducing contrast. (See section 4.5.1.) If we compensate for these Doppler shifts by adjusting the Raman detuning of the $\pi/2$ beams, we can cancel this bias and work at the center of the contrast envelope where the signal is larger. In this case, the atoms once again see zero Raman detuning for each Raman pulse, and $\Delta\Phi = 0$.

To implement this scheme, we must apply opposite Raman detunings to the two $\pi/2$ beams, which can be accomplished by frequency shifting the retroreflected Raman beams with AOMs. The optics setup is shown later in Figure 5.18. Because the AOMs are optimized to work around 80 MHz, we use AOM double passes to up-shift all three Raman retroreflections by $\simeq 2 \times 80$ MHz, with the $\pi/2$ beams offset by $\pm\delta\text{f} = 108.8$ Hz to cancel the Earth's rotation rate. The high frequency rf generating the 9.2 GHz Raman difference frequency must be compensated for the 160 MHz shift. By scanning the frequency δf, we can electronically scan the rotation fringes and avoid the vibration and calibration uncertainties of mechanically rotating the table.

Rather than simply cancelling the bias due to the Earth's rotation rate, one could servo δf so that the rotation signal always reads zero, and accurately determine the rotation rate from the frequency offset δf. A closed loop rotation readout could improve the instrument's linearity by ensuring that the gyroscope is always operating

---

[5]The optical flats were manufactured by Rocky Mountain Instruments, and coated by PFG Precision Optics Inc.

near an effective zero rotation rate. Also, the dynamic range of measurable rotation rates could be increased, since servoing δf would keep the signal within the contrast envelope even for large rotation rates.

AOM rf configuration

To generate the rf frequencies for the three Raman retro AOMs cleanly with minimum phase noise, a single rf synthesizer was used to sweep $+\delta$f and $-\delta$f for the two $\pi/2$ beams, and this synthesizer was mixed with additional synthesizers to generate the rf references for each of the three Raman retroreflections. The synthesizer frequencies used and the required combinations are shown in Table 5.1. The desig-

Item	Frequency	Value (MHz)
AWG1	ν_1	32.5
AWG2	ν_2	47.5
SRS1	ν_3	$15 + \delta$f$/2$
SRS2	ν_4	$16.25 + \epsilon$
North	$2\nu_1 + \nu_3$	$80 + \delta$f$/2$
South	$2\nu_2 - \nu_3$	$80 - \delta$f$/2$
Center (independent)	$\nu_2 + 2\nu_4$	$80 + 2\epsilon$
Center (sum)	$\nu_1 + \nu_2$	80

Table 5.1: Reference frequencies for Raman retroreflection PLL.

nation AWG refers to an HP-8770A arbitrary waveform generator, and SRS refers to an SRS-DS345 synthesizer. SRS1 was used to control δf by adding an offset (typically δf = 108.8 Hz) to its 15 MHz nominal value. The rf synthesizer frequencies were chosen to make combinations of harmonics far from the 80 MHz operating point. The AOM rf implementation used to generate the frequencies in Table 5.1 is described in Appendix B.1.

The retro-reflection double-pass AOMs were always aligned to give +160 MHz shifts, and the single-pass AOM in the injection path of Raman4 was aligned for a -80 MHz shift for counterpropagating transitions, and +80 MHz for copropagating transitions. The high frequency AOM rf frequency was set to $(\nu_{\text{hfs}} + 80 \text{ MHz})/2$

in both cases.[6] Switching between Doppler insensitive and sensitive configurations was then easily accomplished by realigning the single pass AOM between the plus and minus 1 orders and realigning the optical injection. Each Raman laser still propagated in both directions through the atomic beam, but only one set of counterpropagating beams was resonant (the other was 160 MHz detuned). The frequency shifts and resonance condition are given more explicitly in section 7.5.1, in which both Raman lasers are retroreflected.

Frequency modulation

The frequency for the center or π beam was generated in one of two ways. For the frequency modulation technique, where δf was used to compensate or to electronically simulate the rotation rate, the *sum* rf configuration was used. A total of three synthesizers were needed and were arranged such that low frequency phase drifts of the synthesizers cancelled in the interferometer signal. For slow phase drifts, the phase of frequency synthesizer i can be written as follows:

$$\phi_i(t) \simeq \varphi_i^0(t) + \nu_i t. \tag{5.6}$$

Here $\nu_i t$ is the rapid phase oscillation at frequency ν_i, where the frequency is assumed to be constant, and $\varphi_i^0(t)$ is an arbitrary phase that ideally would be constant, but here it is assumed to vary slowly compared to the time of flight between Raman beams, T. For convenience, we will write φ_i in place of $\varphi_i^0(t)$. Then substituting the synthesizer combinations from Table 5.1 for the phases at the interaction times in the expression for the interferometer phase shift, we find:

$$\begin{aligned}
\Delta\Phi_N &= \phi_1 - 2\phi_2 + \phi_3 \\
&= 2\{[(2\varphi_1 + \varphi_3) - 2(\varphi_1 + \varphi_2) + (2\varphi_2 - \varphi_3)] \\
&\quad + [(2\nu_1 + \nu_3)t_1 - 2(\nu_1 + \nu_2)(t_1 + T) + (2\nu_2 - \nu_3)(t_1 + 2T)]\} \\
&= -2\delta f T,
\end{aligned} \tag{5.7}$$

---

[6]In the counterpropagating configuration, the frequency was corrected by 8.265 kHz due to the recoil shift.

the same result as in Equation 4.37. The slowly varying arbitrary phase terms all cancel, which also means there is no way to adjust the arbitrary phase in this configuration. The overall factor of 2 accounts for the AOM double-pass (the local oscillator reference is at 160 MHz). Note that the phase shift correction $-2\delta fT$ in Equation 5.7 changes sign for the other atomic beam because ϕ_1 and ϕ_3 are encountered in the opposite order. Therefore, it acts like a rotation phase shift, and can be used to cancel the usual Sagnac shift. The time domain picture has been used for convenience in examining phase dependence on the synthesizers, but the rotation phase shift can also be computed by considering longitudinal momentum changes as in section 4.5.

Phase modulation

For the *independent* configuration, a fourth synthesizer at frequency ν_4 was added, and it could be used to add a frequency shift, ϵ, to the π pulse. When the π pulse frequency is detuned from zero, a linear phase modulation of the interferometer phase results, as will be shown below. Writing the phases at the interaction times as for the *sum* configuration above, we find:

$$
\begin{aligned}
\Delta\Phi_N &= \phi_1 - 2\phi_2 + \phi_3 \\
&= 2\{[(2\varphi_1 + \varphi_3) - 2(\varphi_2 + 2\varphi_4) + (2\varphi_2 - \varphi_3)] \\
&\quad + [(2\nu_1 + \nu_3)t_1 - 2(\nu_2 + 2\nu_4)(t_1 + T) + (2\nu_2 - \nu_3)(t_1 + 2T)]\} \\
&= -2\delta fT + (4\varphi_1 - 8\varphi_4 - 8\epsilon T) - 8\epsilon t_1 .
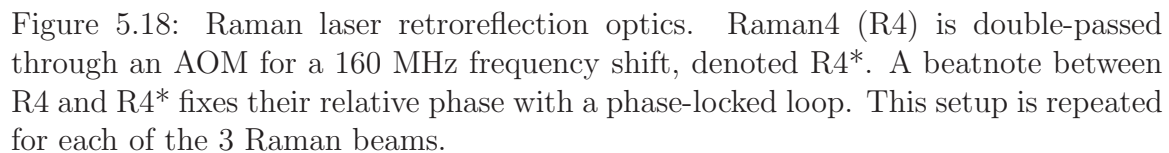\end{aligned}
\tag{5.8}
$$

The term $-2\delta fT$ in Equation 5.8 reflects $\pm\delta f$ detunings of the $\pi/2$ pulses as in the frequency modulation case in Equation 5.7. The terms in parentheses contain an arbitrary phase term that unfortunately does not cancel as it does for the sum configuration. The $-8\epsilon T$ term has the same sign for both atomic beam directions and is equivalent to a linear acceleration. We observed a corresponding shift between North and South contrast envelope centers. The last term is time dependent, since it contains t_1, the initial time the atoms entered the first pulse,[7] which means $\Delta\Phi$

---

[7] Terms with T do not give time dependence, since the time between pulses is constant for a particular velocity class and could be replaced by L/v.

increases linearly with time, and gives linear phase modulation. Since the interferometer signal has the form $\cos(\Delta\Phi)$, the signal will oscillate with frequency 8ϵ. To be explicit, this means that if $\epsilon \neq 0$, the number of atoms detected in the $F = 4$ state will sinusoidally oscillate in time with exactly the same frequency for both atomic beams. (Modulation of the interferometer phase results in amplitude modulation of the atomic signal.) The phase modulation technique is extremely useful, as it allows us to use synchronous detection techniques, either with a lock-in amplifier or equivalently by digitally sampling sine waves and fitting phase, amplitude, and offset, keeping the frequency fixed.

Phase-locked loops

With the addition of the retro AOMs, the distance that Raman4 travels separately from Raman3 has been greatly increased, which could lead to phase shifts due to air currents, mirror mount vibrations, or temperature induced shifts from the AOM. To determine the extent of the phase drift after the AOMs, we set up a Michelson interferometer with an AOM double-pass in one arm and beat the frequency shifted light against the unshifted light. Then we mixed the resulting beatnote with the doubled rf source to get a dc readout of the phase. The phase drift of an AOM from Crystal Technology (Palo Alto, CA) is shown in Fig. 5.17. The high frequency noise is of more concern than the slow drift, since the apparatus is relatively insensitive to slow phase changes but cannot reject high frequency phase noise. We used Crystal Technology AOMs (#3080-120) after finding that they were quieter and had less phase drift with temperature than the Isomet (#1205C-1) AOMs we had used previously. Based on the results of studying the phase stability with and without the AOM, we added a phase-locked loop (PLL) for each of the three Raman retroreflections. The PLLs maintain a constant phase relationship between Raman4 before and after the double-pass trip through the AOM. Since the phase comparison is made close to the vacuum chamber, roughly where the retroreflection mirror was previously, the PLL allows us to recover approximately the same phase stability that would be achieved without the AOM. The optics layout is shown in Fig. 5.18. The beamsplitter used to direct most of the light toward the AOM transmits 1% of the light, which is used to form

Figure 5.17: Phase drift of Crystal Technology AOM.

Figure 5.18: Raman laser retroreflection optics.   Raman4 (R4) is double-passed through an AOM for a 160 MHz frequency shift, denoted R4*. A beatnote between R4 and R4* fixes their relative phase with a phase-locked loop. This setup is repeated for each of the 3 Raman beams.

a beat note at 160 MHz. The phase-locked loop servos the phase of the AOM so the beat note stays in phase with an rf reference. The PLL can compensate for vibrations along the AOM path, but Doppler shifts from vibrations of the mirror that retrore-flects the Raman4 reference will be copied. A 50 mm focal length lens is used in a cat's-eye configuration with a mirror at its focus to retroreflect the light and re-image it, yielding the same beam waist as the incident light at the atomic beam. A 400 mm lens was added before the AOM to form a telescope with the 50 mm lens and magnify the angle of the retroreflection mirror such that a slight misalignment in the vertical direction (which does not compromise AOM efficiency) prevents feedback of the re-flected light into the laser diode. With only the cat's-eye in the AOM double-pass, it was impossible to misalign the retroreflection beam sufficiently to avoid feedback without also having poor AOM efficiency. We achieved 95% diffraction efficiency for a single pass through the AOMs. The AOM and retroreflection optics were mounted on a stable, monolithic block for pointing stability and to minimize vibrations (which the PLL would attempt to remove).

A block diagram of the phase-lock loop electronics is shown in Fig. 5.19. Further discussion of PLL design can be found in [116] and in the MiniCircuits rf design guide. Fig. B.2 in the Appendix gives an expanded diagram of the PLL filter circuitry that conditions the signal from the phase detector.

It should be noted that we found the external timebase circuitry of the SRS-DS345 was responsible for rf phase noise spikes at ~ 3 Hz. Solving this problem required removing the crystal inside the SRS timebase PLL and directly connecting 40 MHz at ~ 0 dBm quadrupled from our 10 MHz reference oscillator. A MiniCircuits 4T-6T transformer was used to make the connection without introducing a ground loop.[8]

5.8.4 Raman beam alignment

The interferometer depends crucially on the Raman beam alignment, and the beams must be set precisely before an interference signal can be seen. For the horizontal alignment, the Doppler shift $\Delta\omega = -\boldsymbol{k}_{\text{eff}} \cdot \boldsymbol{v}$ must be smaller than the linewidth of

---

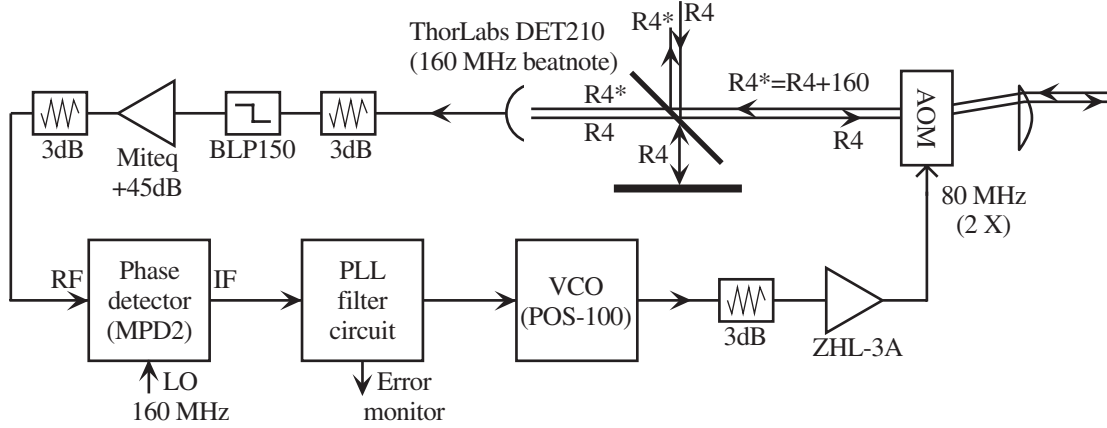[8]The solution to this SRS timebase problem was suggested by Kurt Gibble.

Figure 5.19: PLL electronics block diagram. The photodiode beatnote signal is filtered and amplified before entering a phase detector where it is compared with a local oscillator. The phase output is fed into a PLL filter circuit, shown in detail in Fig. B.2. The filter circuit contains a low pass filter to smooth the output and adjust the capture range of the loop, and adds adjustable gain and offset to condition the signal for the voltage controlled oscillator (VCO) that follows. Finally, the rf output of the VCO is amplified and fed into the AOM.

the transition, typically ~ 300 kHz. This implies $\theta \ll 4 \times 10^{-4}$ rad, which is easily achieved by scanning the Raman detuning to find the center of the Doppler shifted Raman transition, and adjusting the angle of the beam until the transition is centered at 0 detuning. (This assumes that the Raman intensities have been adjusted to cancel ac Stark shifts.) The vertical Raman beam alignment is equally critical, yet there is no sensitive diagnostic like the Doppler shift that can be used to determine the vertical alignment for an individual Raman beam. The alignment condition for the vertical is that

$$|\boldsymbol{k}_1 - 2\boldsymbol{k}_2 + \boldsymbol{k}_3| \ll \frac{\pi}{w}, \tag{5.9}$$

where w is the spatial width of the atomic beam, and $\boldsymbol{k}_i$ are the effective Raman propagation vectors. This is because atoms at different transverse positions in the atomic beam will see different laser phases since $\phi = \boldsymbol{k} \cdot \boldsymbol{x}$, and misalignments will cause different interferometer phase shifts of the form $\phi_1 - 2\phi_2 + \phi_3$, which will average out and reduce contrast.

Coarse alignment

The alignment strategy to obtain a gyroscope signal from the beginning[9] (assuming the Raman spatial filter has already been aligned) is as follows: First the atomic beams must be aligned to be counterpropagating. Because the ovens have adjustable direction but approximately fixed position, the beam alignment is uniquely determined. CCD cameras were installed at both ends of the chambers to observe fluorescence in the detection regions. The cameras were used to verify horizontal and vertical overlap of the beams and to verify the transverse cooling alignment. The beam position was primarily adjusted by the 2D cooling, followed by a fine adjustment of the oven angle to maximize signal. Once the 2D cooling has been optimized, small pointing changes can be made by adjusting only the cooling retroreflection mirrors. Then the CCD cameras were removed and replaced by the detection collection lenses and amplified photodiodes. After the probe beam and detection optics were first put in position, these were used in connection with the Raman beams to reset the atomic beam directions when needed, avoiding reinstalling the cameras.

Copropagating Raman transitions were used in each of three interaction regions with a small aperture to set the height of the Raman beams relative to the atomic beam. The height was measured on each side of the vacuum chamber and the Raman beams were adjusted to be parallel to the table and centered on the atomic beam.

Horizontal alignment

To observe counterpropagating Raman transitions, the Raman beams must be perpendicular to the atomic beam to high accuracy. For aligning the Raman beams completely from scratch, the angle was coarsely set initially by using only one Raman laser and scanning the master laser to sweep the slave through resonance, optically pumping atoms in the beam. The final incident Raman mirror was adjusted horizontally, while following up on a retroreflection mirror on the other side of the chamber to keep the beam reflected back on itself by centering on an aperture at the output of the spatial filter. (When aligning from scratch, the PLL beamsplitter is replaced

---

[9]Even after experience aligning the gyro, a full realignment typically took ~ 1 week.

by a retroreflecting mirror, as the beam angle can not be varied widely and still pass through the AOM with good efficiency.) The width of the optical pumping peak was narrowest when the Raman beam was roughly orthogonal to the atomic beam, since the longitudinal velocity spread of the atoms could no longer Doppler broaden the transition. This technique made it possible to obtain a counter-propagating Raman signal, which could then be optimized.[10]

Intensity balance

The intensity ratio between the Raman lasers must be set to cancel ac Stark shifts, before the final optimization of the counter-propagating transition horizontal beam angles can be made. Otherwise, ac Stark shifts would mimic Doppler shifts, causing offsets in the horizontal Raman alignment angles and reducing interferometer contrast. Also, the ac Stark shift is proportional to intensity, so π and $\pi/2$ beams would have different angle misalignments if the ratio were set incorrectly. For the Doppler-sensitive configuration, the ac Stark shift was compensated experimentally by varying the Raman beam intensity ratio and measuring the shift of the Raman transition peak when both intensities were reduced by a factor of two. For the optimal intensity ratio, the shift should be zero. The product of the Raman intensities must be adjusted to yield a π pulse while maintaining the same intensity ratio. A simple argument is sufficient to show why the ac Stark shifts can be made to cancel. Light detuned from resonance by Δ causes an ac Stark shift of an energy level by an amount $\Omega_r^2/4\Delta \propto I/\Delta$, where $\Omega_r = \boldsymbol{d} \cdot \boldsymbol{E}/\hbar$ is the Rabi frequency, and I is the laser intensity. The $F = 3$ and $F = 4$ ground state levels are shifted due to both Raman beams, since both are detuned from resonance. The shift for $F = 4$ is $\simeq \dfrac{I_4}{\Delta} + \dfrac{I_3}{\Delta + \nu_{\mathrm{hfs}}}$, where I_3 and I_4 are the intensities of Raman3 and Raman4, ν_{hfs} is the 9.2 GHz groundstate splitting, and Δ is the global Raman detuning defined to be negative when red-detuned (as it was in the experiment). Similarly, $F = 3$ is shifted by $\simeq \dfrac{I_3}{\Delta} + \dfrac{I_4}{\Delta - \nu_{\mathrm{hfs}}}$. The Raman transitions are only sensitive to the difference frequency between the $F = 3$ and $F = 4$ levels, which changes by the difference of

---

[10]The optical pumping technique was essential the first time the gyro signal was obtained, since at first the Raman lasers propagated independently and were separately spatially filtered.

the two expressions above, which simplifies to $\dfrac{-\nu_{\text{hfs}}}{\Delta}\left[\dfrac{I_4}{(\Delta - \nu_{\text{hfs}})} + \dfrac{I_3}{(\Delta + \nu_{\text{hfs}})}\right]$. This expression is 0 if

$$\frac{I_4}{I_3} = \frac{\nu_{\text{hfs}} - \Delta}{\nu_{\text{hfs}} + \Delta} \,. \tag{5.10}$$

This calculation has neglected the important fact that there are actually several excited states to which the ground state levels can couple, and these must be properly weighted by the Clebsch-Gordon coefficients governing their transition probabilities. The results of the full calculation (which have been omitted here) were in good agreement with experiment.

Scale factor (L)

After adjusting the horizontal Raman angles to center the peaks, the beam spacing L between the North–Center and Center–South beams must be made equal. Originally this was done to < 1 mm precision using a tape measure and then optimized using a copropagating $\pi/2 - \pi - \pi/2$ sequence and adjusting the beam spacing to null the signal. Later, we used a precision 1 m caliper, which also allowed an accurate determination of the interferometer scale factor, namely the signal output for a given rotation input. Recall that the $\pi/2$ Doppler shift readout method of section 5.8.3 gives a rotation signal proportional to $k_{\text{eff}}\Omega L$. We measured L precisely using a 1 m digital caliper (Mitutoyo model #500-507-10) with 0.01 mm resolution and ± 0.076 mm specified absolute accuracy. By measuring optical power through a pinhole glued to the caliper jaw and using reflections off the machined surface to assure angular alignment, we measured a North–Center separation of $L = 96.842 \pm 0.015$ cm and set the South–Center spacing to be the same by walking the South Raman beam to maximize power through the pinhole. The interferometer enclosed area depends on the separation distance as:

$$A = \frac{v_r}{v}L^2 \,, \tag{5.11}$$

where v_r is the recoil velocity. For a beam velocity of 290 m/sec, $A = 22\text{mm}^2$ and the maximum atomic wavepacket separation is 24 μm. The plane of the gyroscope enclosed area is parallel to the floor, so

$$\mathbf{\Omega}_E \cdot \mathbf{A} = \sin(\varphi_{\text{lat}})\Omega_E A \,. \tag{5.12}$$

The latitude at Yale measured by GPS is 41:19:02.661N, so $\sin(\varphi_{\text{lat}}) = 0.66023$. The single interferometer phase shift due to the Earth rotation rate is 6.8 rad, or 4.5 rad when projected to Yale's latitude.

Vertical alignment (tilt-sensor)

Next, the fine vertical alignment must be adjusted. This was achieved using a tilt sensor with < 10 μrad repeatability (from Applied Geomechanics) rigidly mounted to a high quality Lees mirror mount that held a vertically mounted reference mirror. Originally we set up a Michelson optical interferometer to align the incoming beam perpendicular to the reference mirror. The tilt reference mount must be moved and re-zeroed for each beam. Aligning the experiment to the tilt sensor zero makes all the beams parallel, and also makes the Raman beams perpendicular to the local gravitational acceleration plus centripetal acceleration from the Earth's rotation,[11]

$$\mathbf{a}_{\text{cen}} = -\mathbf{\Omega}_E \times (\mathbf{\Omega}_E \times \mathbf{r}) \,. \tag{5.13}$$

The absolute accuracy of the tilt sensor technique was calibrated using a precision level. First, the table tilt was adjusted so the precision level indicated horizontal. Then a laser was retroreflected to be perpendicular to the tilt sensor reference mirror, and the slope of the laser relative to the table was determined by measuring the beam height at various positions with an aperture on a translation stage and a power meter. The tilt sensor assembly differed from the precision level by 1.2 mrad, due to machining tolerances and the wedge and mounting accuracy of the reference mirror. However, the relative error between the Raman beams using this method was limited

---

[11]The centripetal acceleration due to Ω_E is equal to $\mathbf{a}_{\text{cen}} = 2.5 \times 10^{-2}$ m/sec^2 at Yale.

by the 10 μrad tilt sensor repeatability, rather than by this systematic shift. The tilt repeatability of the floating table was measured to be $\sim 1 \times 10^{-4}$ rad, but was unfloated during the tilt sensor alignment.

Originally, when the Raman lasers propagated independently rather than copropagating through a single spatial filter, the tilt sensor assembly was used facing opposite directions for the two Raman beams, so the net tilt cancelled for $\boldsymbol{k}_1 - \boldsymbol{k}_2$. This tilt cancellation method is not necessary, however, since acceleration due to projection of local gravitational acceleration $\boldsymbol{g}$ onto the Raman beams can be observed on the dual gyro signal through a shift between the two contrast envelopes (clearly distinguishable from rotation). Fine adjustments of the Raman tilt were made by minimizing this contrast envelope offset. Instead of setting up Michelson interferometers for initial alignment, it was sufficient to align the incident laser beam vertical and tilt sensor reference mirror horizontal to achieve feedback into the laser for each Raman beam. After the beams were vertically aligned, the retro AOM optics were replaced and the laser feedback technique was used to recover the alignment. Because the laser performance was severely degraded when there was light feedback, all three retroreflection beams were slightly misaligned in the vertical direction by a fixed amount that was sufficient to avoid feedback.

After setting the vertical alignment, fine adjustments to the horizontal alignment were generally needed to make sure that the center Raman frequency for all three beams matched within $\simeq$ 10 kHz. This procedure ensured that the gyroscope was roughly aligned, and final adjustments were made by tweaking up the interference signal. (The vertical alignment was particularly critical.) With the retro AOMs in place, the phase modulated signal gave periodic oscillations that were convenient for optimization.

5.9   Data acquisition and computer control

A 450 MHz Intel Pentium-II computer with 128 MB RAM is used for data acquisition and analysis. Two Hewlett Packard HP3458A multimeters are used to acquire voltage data simultaneously from the North and South atomic beams respectively,

and are read by separate GPIB controllers (National Instruments PCI cards) using asynchronous block read commands. The HP3458A multimeters were used because we needed fast reading rates in real-time, and we required higher precision than the 8 bits provided by our digital oscilloscope. The HPs can stream large blocks of 6.5 digit readings (corresponding to 21 bits precision) over GPIB in real time at over 3000 points per second, which is more than sufficient for our application. This instrument is specified to have < 10 ppm absolute accuracy. For integration times greater than 1/60 sec, integer multiples of powerline cycles were typically used to reject 60 Hz line noise.

For proper common mode rejection, the multimeters must be synchronized, accomplished using an external trigger. The trigger pulses are generated by an SRS-DS345 30 MHz synthesizer that is controlled by the data acquisition computer. The SRS can itself be powerline or externally triggered and then its burst mode can be used to output a pulse train of triggers to the HPs for each trigger it receives. This burst feature is useful if, for example, another synthesizer is used to electronically scan the rotation rate and a fixed number of samples are desired for each scan. Because initiating a block read command ties up the GPIB bus, a third GPIB card (and bus) was used to control the triggering and other instruments. Due to a bug in the SRS synthesizer, reconfiguring it to start generating pulses causes extra glitches to appear on the output, which could cause the HPs to acquire data. This problem was solved by adding external digital logic to disable the trigger pulses to the SRS and the HPs while the SRS was being configured. (The logic gates were switched via GPIB control using a signal from the auxiliary output of a nearby lock-in amplifier.) The program allocates a block of memory to store an entire trigger burst segment, which can contain $> 10^7$ points, limited only by available memory. The program can be also configured to automatically save a number of segments to each of a series of files.

The data acquisition software consists of more than 200 kilobytes of C++ code written using the Microsoft Foundation Class library, which made it convenient to add features and generate a standard graphical user interface. The acquisition software was also used for data analysis; for example, to perform non-linear curvefits of the frequency or phase modulated data. The program can also acquire data from the

slower HP34401A multimeters, or the Tektronix TDS420A digital oscilloscope, which is useful when monitoring additional parameters during a data run, such as beam pointing, room temperature, or the seismometer. The program can also be used to step through discrete frequencies on the HP83711B rf synthesizer to study Raman transitions or to step through different rotation biases with the DS345 synthesizer. A second computer is used for the digital servo of the Raman master laser and Vortex lock.

The timing and frequency synthesizer control system used to generate the rf for the detection and cooling laser AOMs is described in Appendix C.

Chapter 6

Results

6.1 Raman transitions

For aligning and characterizing the apparatus, we frequently studied Raman transitions for a single interaction region. Atoms are initially pumped into the $F = 3$ state with $F = 4 \rightarrow F' = 4$ light before interacting with the Raman pulse. When the Raman detuning δ is varied while plotting the number of atoms in the $F = 4$ state, a series of 7 peaks can be observed in the number distribution, corresponding to allowed Raman transitions from different m_F levels. Because atoms either start or finish in the $F = 3$ state, there is one peak for each m_F level of the $F = 3$ state, or $2F + 1 = 7$ peaks. We apply a large magnetic bias field that removes the degeneracy of the energy levels and separates the peaks such that only $m_F = 0$ atoms are excited, aside from a few percent of $m_F = \pm 1$ atoms from the tails of the neighboring peaks. The Raman detuning is scanned by stepping the HP83711B rf synthesizer through a series of discrete frequency steps, or by continuously sweeping the 80 MHz AOM in the Raman4 injection beam. Because the atomic beam operates continuously, sweeping the AOM allows Raman transitions to be monitored in real time on an oscilloscope.

Fig. 6.1 gives a comparison of Raman transitions in the Doppler-sensitive and Doppler-insensitive geometries. The Doppler-sensitive peaks are broadened by the transverse velocity spread of the beam, since an atom with transverse velocity v_t is in resonance for a Raman detuning of $\delta = k_{\mathrm{eff}} v_t$. The linewidth of the Raman
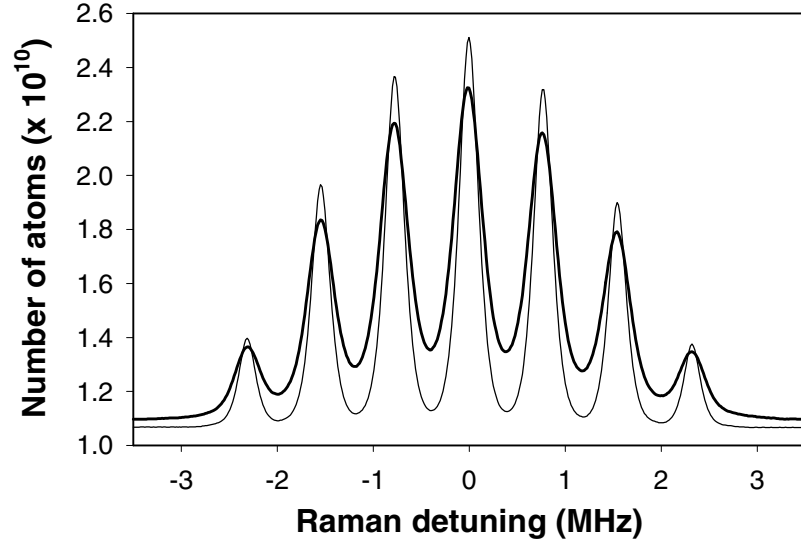
Figure 6.1: Raman transitions in the counterpropagating (Doppler sensitive) excitation geometry shown with a thick line, and Raman transitions in the copropagating (Doppler insensitive) excitation geometry shown with a thin line. The Raman detuning frequency was stepped with the HP83711B synthesizer.

transitions is inversely proportional to the Raman beam waist, which determines the interaction time with the light. By using narrow Raman beam waists, a broad range of transverse velocities can be addressed, increasing the number of atoms that participate in the interferometer. The Doppler-sensitive peak width is given by a convolution of the transverse velocity distribution and the Raman linewidth. For the Doppler-insensitive case, the Doppler shifts of the two beams cancel when taking the difference $\boldsymbol{k}_1 - \boldsymbol{k}_2$, and peak width is just given by the Raman transition linewidth. We used Doppler-sensitive transitions to measure the transverse velocity distribution of the atomic beam, yielding ± 11 cm/sec FWHM. We had originally used circular Gaussian beams with 5.5 mm wide slits to aperture the beam and define a fixed Raman pulse width, but later we reconfigured the optics by adding a cylindrical lens such that the Raman beams had an 0.4 mm waist. This was a great improvement, as it increased the number of atoms that could be addressed by a factor of ~ 5, resulting in a proportional increase in the amplitude of the gyroscope signal. The narrower Raman beams were used to acquire the data in Fig. 6.1.

6.2   Initial interference signals

6.2.1   Phase plate

For the first atom interference signal obtained, the interferometer phase shift was scanned by rotating a 0.5" thick AR-coated optical flat placed at 45° in one of the Raman pulses. The optical path length through the glass varied with the plate angle, shifting the phase of the light. At this time, the Raman beams were spatially filtered separately, which made it convenient to shift the phase of only one laser, as required for this technique. The plate was placed in the final $\pi/2$ beam, but it could have been used in the π pulse for twice the phase sensitivity. It must be placed after the first beamsplitter, since the overall phase of the Raman beams cancels. The plate could be modulated at up to 30 Hz using a piezo-electric with 15 μm maximum extension. The results of sinusoidally modulating the phase plate are shown in Fig. 6.2, and served to explicitly verify the relationship between the interferometer phase shift and the phase of the Raman laser pulses. The phase plate was briefly used as part of a servo loop that controlled the optical phase to maintain a constant gyroscope signal, and the rotation information was then read from the servo error signal.

6.2.2   Table rotation

We initially verified the sensitivity of the interferometer to rotations by mechanically rotating the optical table. This was done using a small low voltage piezo glued to the table and pushing against a heavy pillar of cinder-blocks and lead weights. The pillar had sorbothane rubber pads to isolate the stack against vibrations from the floor, and a ball bearing glued to the free end of the piezo allowed free vertical motion against a slip plate attached to the pillar. The table was floating on pneumatic legs, and a seismometer (Kinemetrics SS1) was used to determine the center of rotation and to calibrate the table motion. We drove the table at 4.5 Hz, near its resonance, and observed interference fringes using a single atomic beam as shown in Fig. 6.3. We measured a signal-to-noise ratio of 400:1 for 800 msec of integration per point, both at the center of the fringe and on the tails. We observed a shift between the rotation

Detected Fluorescence
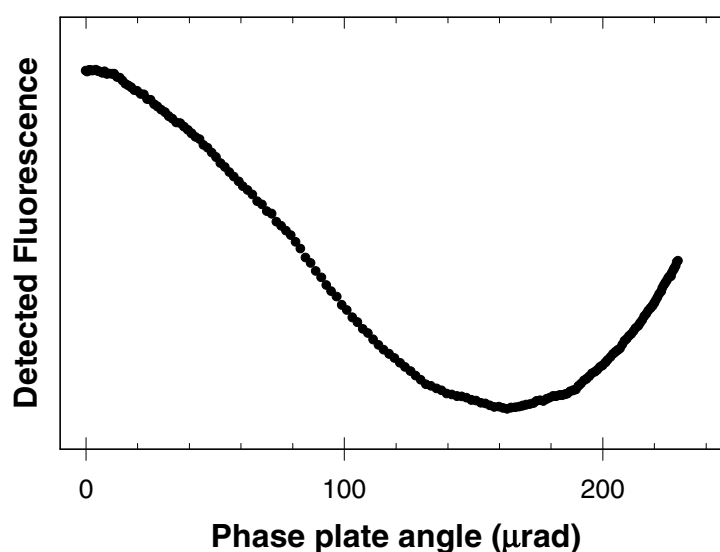
Phase plate angle (μrad)

0   100   200

Figure 6.2: Atom interference phase shift vs. optical phase plate angle. The number of atoms in the $F = 4$ state detected at the exit of the interrogation region is plotted as a function of the Raman $\pi/2$ optical phase. The phase was scanned by rotating a 0.5" plate in the optical path of one Raman beam. The peak-to-peak signal amplitude corresponds to $\sim 10^7$ atoms/sec with 20% contrast. Reprinted with permission from T.L. Gustavson, P. Bouyer, and M.A. Kasevich, *Phys. Rev. Lett.* **78**, pp. 2046, 1997. Copyright 1997 by The American Physical Society.
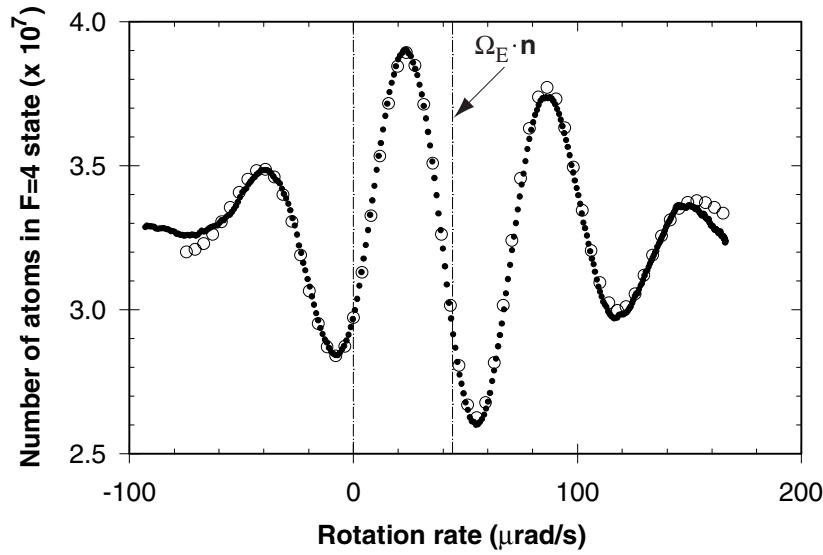
Figure 6.3: Atom interference versus table rotation rate measured by a seismometer. Black dots are experimental data (800 msec/pt integration time), open circles are calculated signal. The shift of the contrast envelope relative to the seismometer zero provides a measurement of Earth's rotation rate, projected onto Stanford's latitude. Reprinted with permission from T.L. Gustavson, P. Bouyer, M.A. Kasevich, *Phys. Rev. Lett.* **78**, pp. 2046, 1997. Copyright 1997 by The American Physical Society.

zero measured by the seismometer and the contrast envelope center, which indicates zero rotation as measured by the atoms. The offset arises because the seismometer is not sensitive to the constant rotation rate of the Earth but the gyroscope is, and measuring the offset gives the Earth rotation rate. To extract the offset more precisely, we used the theoretical model described in Chapter 4 to find the center of the contrast envelope. We found a rotation rate of 45 ± 3 μrad/sec, which is consistent with the expected value of 44.2 μrad/sec for Stanford's latitude. The error is due to the uncertainty in the seismometer calibration. The model was adjusted to account for an arbitrary optical phase (experimentally uncontrolled) that determines the fringe location within the contrast envelope.

This measurement pointed out the need for three major improvements to the apparatus.

1. *Signal-to-noise.* Since this measurement was made, the signal-to-noise has been improved by a factor of 66. This gain mainly came from a 300-fold increase in the atomic flux, improvements to the $|F = 4\rangle$ laser lock (reducing detection and cooling noise) and reconfiguration of the Raman optics. Many of these improvements have already been included in the description of the apparatus in Chapter 5.

2. *Dual atomic beams.* Counterpropagating atomic beams can be used to determine absolute zero rotation rate (without using a seismometer).

3. *Rotation bias.* The offset due to the Earth's rotation shifts the operating point away from the maximum of the contrast envelope, which reduces the signal. Adding an electronic compensating rotation bias improves signal-to-noise, and is essential for measuring rotation rates much larger than Ω_{E}, for which the contrast would otherwise be poor. Also, an electronic method for scanning the fringes improves repeatability and avoids vibrations.

The results of implementing these modifications will be discussed further in the remainder of this chapter.

6.3   Short-term sensitivity

Short-term sensitivity measures the ability to detect small rotations over short time scales for which slow drifts of the apparatus are unimportant, and depends on interferometer area and signal-to-noise. We used a rotation-independent method to determine the signal-to-noise because we have no independent means to characterize the rotational noise of the lab, which we expected to be above the intrinsic sensitivity of the gyroscope. Ideally, we might use a test platform that had extraordinarily low rotational and vibrational noise, with well controlled tilt. Such facilities exist, but the difficulties of transporting our instrument precluded their use. For example, according to Lawrence [3], the Air Force Academy's Seiler Laboratory in Colorado has a pneumatically isolated test pier that weighs 205,000 kg and is stable to $< 10^{-8}$ g and $< 5 \times 10^{-9}$ rad tilt. Instead, we have estimated our short-term sensitivity from a signal-to-noise analysis of data taken using a rotation insensitive configuration. For example, if the electronic rotation compensation frequency δf is offset by 1 kHz, that is equivalent to monitoring a rotation rate larger than the width of the contrast envelope, giving no rotation sensitivity. Using this technique and lock-in amplifier demodulation to get rid of low frequency drifts, we achieved a signal-to-noise level of 33,000. (The signal-to-noise at δf = 1 kHz was divided by the peak-to-peak rotation interference signal measured by electronically scanning the contrast envelope via δf.) The demodulation technique was used because in a rotation-sensitive configuration we would use lock-in detection at a quiet frequency, but outside the contrast envelope, there is nothing to modulate. The rotation-insensitive configuration detects noise due to atomic flux variations, state preparation, cooling, detection, and Raman pulse area, but is insensitive to Raman phase.

To compute rotation sensitivity from signal-to-noise, we express the interference signal S as a function of an acceleration a (rotational or linear) in the form:

$$S(a) = \frac{N}{2} \left[1 - \eta \cos \left(k_{\text{eff}} a T^2 + \frac{\pi}{2} \right) \right] \tag{6.1}$$

where N is the number of atoms contributing to the interferometer signal, the contrast is $\eta \equiv \frac{max - min}{max + min}$, and T is the time between Raman pulses. The peak-to-peak

interference fringe signal is:

$$S_{pp} \equiv \frac{N}{2}\left[(1+\eta)-(1-\eta)\right] = \eta N \,. \tag{6.2}$$

Taking the derivative of the signal with respect to acceleration yields:

$$\left.\frac{dS}{da}\right|_{a=0} = \frac{N}{2}\eta k_{\text{eff}}T^2 = \frac{\Delta S}{\Delta a} \,, \tag{6.3}$$

and rearranging, we get:

$$\Delta a = \frac{\Delta S}{S_{pp}}\frac{2}{k_{\text{eff}}T^2} \,. \tag{6.4}$$

Note that ΔS is the noise, and S_{pp} is the signal, so $\Delta S/S_{pp}$ is the inverse of the signal-to-noise ratio, SNR^{-1} (where SNR is used to avoid confusion with S and N). For rotation measurements, substituting in the Coriolis acceleration gives $|\Delta a| = 2v\Delta\Omega$, and we find:

$$\Delta\Omega = \text{SNR}^{-1}\frac{1}{vk_{\text{eff}}T^2} \,. \tag{6.5}$$

Near $\Omega = 0$, the signal detected is $N/2$, giving shot-noise fluctuations of $\sqrt{N/2}$ and signal-to-noise of:

$$\text{SNR}_{ShotNoise} = \eta\sqrt{2N} \tag{6.6}$$

where we have used Equation 6.2. The above formulas have been written in a form that appears appropriate for a single atomic beam; however, they may be used for dual beams by simply adding the number of atoms in both interferometers. For a beam with $v = 290$ m/sec, $1/vk_{\text{eff}}T^2 = 2 \times 10^{-5}$. Therefore, a signal-to-noise of 33,000 (achieved by combining the two atomic beam signals) corresponds to a short-term sensitivity of 6×10^{-10} (rad/sec)/$\sqrt{\text{Hz}}$. For typical current operating parameters, we have $\eta = 0.3$ (maximum achieved was $\eta = 0.34$) and $S_{pp} = 5 \times 10^9$ atoms/sec per atomic beam, so we can solve for N and use Equation 6.6 to find

$\mathrm{SNR}_{ShotNoise} = 7.7 \times 10^4$. Therefore, this flux corresponds to a shot-noise limited rotation sensitivity of 2.6×10^{-10} (rad/sec)$/\sqrt{\mathrm{Hz}}$.

6.4   Dual atomic beams

The Sagnac phase shift depends on the Coriolis acceleration, $\boldsymbol{a}_{\mathrm{Cor}} = -2\,\boldsymbol{\Omega} \times \boldsymbol{v}$, which is proportional to the vector velocity, $\boldsymbol{v}$, and therefore has opposite sign for the two atomic beams. Our rotation-rate measurement approach depends fundamentally on this phase shift reversal. The gyroscope signals have the form:

$$S_{\mathrm{North}} \quad \sim \quad \cos(\Phi_\Omega + \phi_{\mathrm{arb}}) \tag{6.7}$$

$$S_{\mathrm{South}} \quad \sim \quad \cos(-\Phi_\Omega + \phi_{\mathrm{arb}})\,, \tag{6.8}$$

where S represents the detected signal of the North or South beam. Using standard trigonometric identities, one can rearrange these equations as follows:

$$S_{\mathrm{North}} - S_{\mathrm{South}} \sim \sin(\Phi_\Omega)\cos(\phi_{\mathrm{arb}})\,. \tag{6.9}$$

Due to the sine factor, the difference signal has a zero crossing for zero rotation rate, and the cosine amplitude factor can be maximized by adjusting the arbitrary phase. Therefore, this method allows precise determination of the zero rotation rate relative to the non-rotating inertial frame, and does not depend on knowledge of the gyroscope area or arbitrary phase.

Note that this derivation assumed that the rotation phase shifts have equal magnitudes for the counterpropagating atomic beams, and since the two atomic beams have slightly different velocity distributions, the phase shift magnitudes are not exactly equal. For our atomic beams, the measured velocity distribution parameters differed by $4-7\%$ (see section 5.4.2). Because the contrast envelope is centered at zero rotation regardless of the velocity distribution, the technique of subtracting the counterpropagating interference signals would seem to be insensitive to velocity distributions. However, because the time delay between the atoms passing through the

center of the interferometer until detection varies with velocity, a change in velocity distribution could lead to an apparent rotation phase shift. The size of this effect depends on the detection scheme used, and we are currently studying the extent to which this might affect our long-term stability results.

To implement counterpropagating atomic beams, cesium sources were mounted at each end of the vacuum chamber and aligned to overlap spatially (collisions are negligible) so that the beams would pass through the same magnetic bias field. The atoms from each atomic beam are transversely cooled in two dimensions using red-detuned laser light, and are optically pumped into the $F = 3$ ground state before passing through the detection laser for the opposing atomic beam. Since the detection light is tuned to the $F = 4 \rightarrow F' = 5$ resonance, the only atoms detected are those that end up in the $F = 4$ state after the interferometer interaction pulses. Common-mode rejection is enhanced because the interferometers share all laser sources, namely light for cooling, optical pumping, Raman beams, and detection.

6.5 Raman beam frequency control

In this section, we present a detailed description of the data acquisition and reduction procedure for the frequency and phase modulation detection techniques, and present results achieved with each method. Independent control of the three Raman beam retroreflection frequencies can be used for electronically shifting the effective rotation rate, and for synchronous detection techniques.

6.5.1 Frequency modulation

Section 5.8.3 described how shifting the frequencies of the two $\pi/2$ Raman retrore-flection beams (by $\pm\delta f$, respectively) could be used to offset the effective rotation rate; for example, to compensate Earth's rotation rate, or to electronically scan the interferometer fringes. We also used a frequency modulation technique, for which we applied a triangle-wave modulation to the $\pi/2$ retro offset frequencies to scan over the contrast envelope. For each period of the scan, we computed the rotation-rate

	Theoretical:	Measured:
N	$\cos\left(\dfrac{2\pi}{f_N}(x-r)+\phi_{\text{arb}}\right)$	$\cos\left(\dfrac{2\pi}{f_N}x+\varphi_N\right)$
S	$\cos\left(-\dfrac{2\pi}{f_S}(x-r)+\phi_{\text{arb}}\right)$	$\cos\left(\dfrac{2\pi}{f_S}x+\varphi_S\right)$

Table 6.1: Frequency modulation signal extraction.

and arbitrary phase after fitting the data from the North and South atomic beams using a nonlinear curve-fitting routine (adapted from [117]). The six parameter fitting function had the form:

$$y(x) = c + a\cos\left(2\pi\frac{x}{f}+\varphi\right)\exp\left(-\frac{(x-f_0)^2}{2\sigma^2}\right),\qquad(6.10)$$

where amplitude a and offset c depend on the signal and background levels, x is the frequency scan value δf, f is the oscillation frequency (depends on the atomic beam velocity distribution), φ is a phase (contains rotation, acceleration), and f_0 and σ are the center frequency and width of the contrast envelope, respectively. This fitting function is only an approximation, but it gave a reasonable fit and can be computed quickly. Since we don't know the arbitrary phase and acceleration *a priori*, an additional processing step is required to separate the rotation and arbitrary phase information. Table 6.1 illustrates the discrepancy between the theoretical versus measured forms of the signals. (The exponential envelope factor has been omitted.) Here r is the time varying rotation rate in units of the Doppler shift frequency, δf, that would need to be applied to compensate for the rotation rate. The oscillation frequencies for the North and South beams are denoted f_N and f_S. Solving for the rotation, r, and arbitrary phase plus acceleration, ϕ_a, we find:

$$r = -\frac{(\varphi_N+\varphi_S)}{\dfrac{2\pi}{f_N}+\dfrac{2\pi}{f_S}}\qquad(6.11)$$

$$\phi_a = \varphi_N+\frac{2\pi}{f_N}r,\qquad(6.12)$$

where φ_N, f_N, φ_S, and f_S are the average of the fit values for scanning up and for scanning down within each period. This averaging removes the effect of the delay between the time when atoms pass through the interferometer (encountering a particular δf) and when they are detected. This delay depends on the position of the probe beam and on the velocity distribution of the atoms. To improve convergence, each fit started with an initial guess set to the result of the previous period. Phase was fit first while freezing other parameters, then all parameters were allowed to vary. A data set taken with the frequency modulation technique is shown in Fig. 6.4. With this data set, we learned that the optical table floating on pneumatic legs has a broad resonance at 1.7 Hz, which is difficult to average away. Furthermore, since there is nothing to control the angular position of the table, the floating table is a potential problem for long-term drift. (For this measurement, the table was pinned at one corner by the piezo that had been used previously to drive the table motion.) Results will be given in section 7.6 with the table lowered to the floor.

6.5.2 Phase modulation

By adding a constant offset, ϵ, to the detuning of the middle Raman beam, we observed the number of atoms in the $F = 4$ state oscillating sinusoidally in time, as explained in section 5.8.3. We typically set ϵ for 48 Hz phase modulation. (With our present rf configuration, the oscillations occur at frequency 8ϵ, since the π retro rf frequency is $80 + 2\epsilon$, the AOM is double-passed, and the phase sensitivity to the π pulse, $\phi_1 - 2\phi_2 + \phi_3$, gives another factor of two.) To test our ability to extract rotation information using the phase modulation technique, we added a triangle wave modulation to δf with 200 Hz span at 0.02 Hz. Acquiring data at 480 Hz gave 10 samples per sine wave, and a non-linear curve-fit was performed for each period of the 48 Hz oscillation to extract the phase information from the North and South beam data. The result is shown in Fig. 6.5. The curves were fit to a sine wave with fixed frequency (48 Hz), but arbitrary offset, amplitude, and phase. The curve fitting was substantially faster than the time for acquisition, so it could be implemented in real-time, but instead it was always done as a post-processing step. The phase modulation
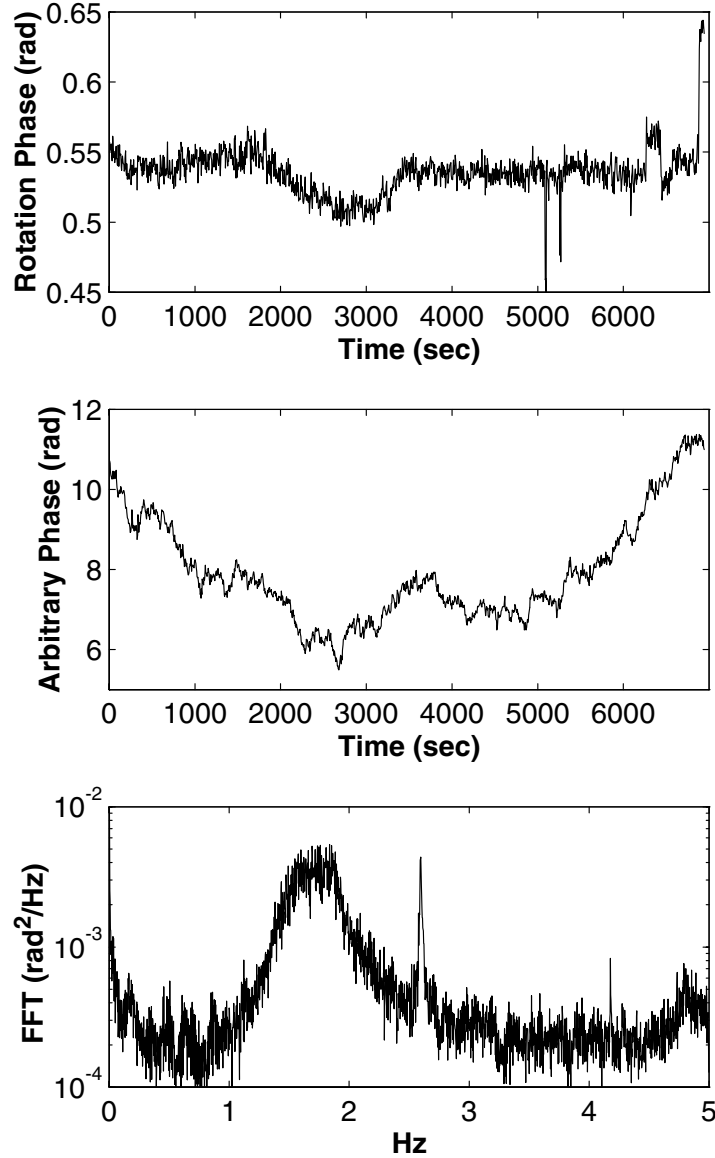
Figure 6.4: Rotational noise with frequency modulation readout. The upper plot is the rotation signal, center plot is arbitrary phase, and the bottom plot is the power spectral density of the rotation signal. The broad peak in the FFT spectrum at 1.7 Hz was due to a rotational resonance of the floating optical table. The sharp peak at 2.6 Hz was due to rf electronics and was later corrected. Data acquisition parameters: the Doppler shift frequency δf was centered at 52 Hz with a 120 Hz span triangle-wave frequency sweep at 10 sweeps/sec. 100 samples were taken per sweep at 0.9 msec integration/point. The phase plots have been averaged to 5 sec/point.
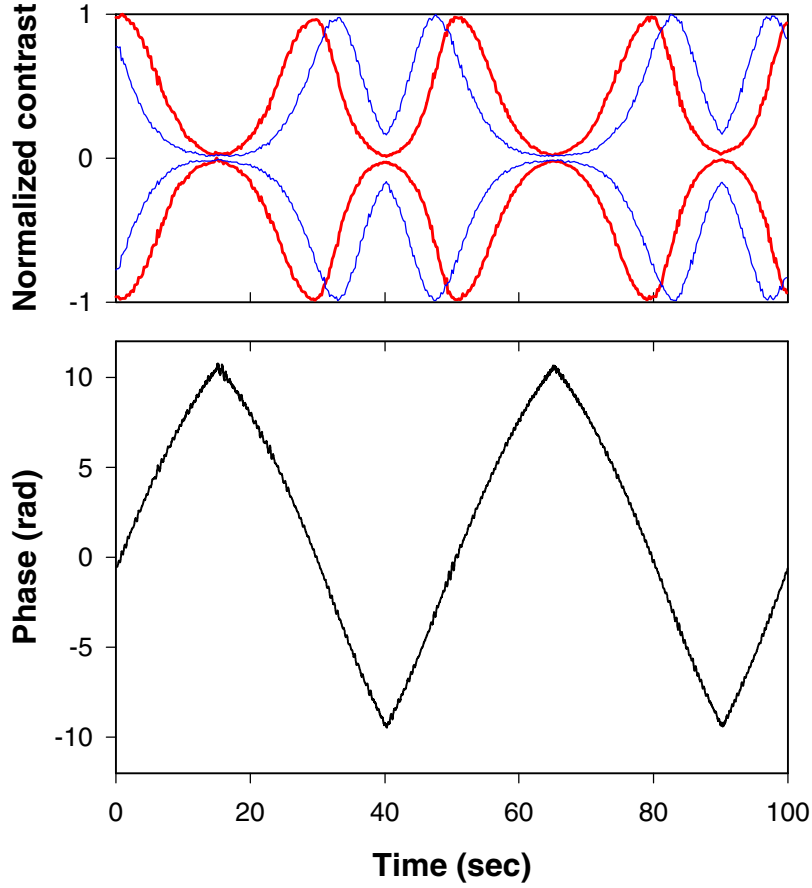
Figure 6.5: Electronic rotation scan with phase modulation readout. The upper box shows the signal before extracting phase information, normalized to unity. Since the 48 Hz oscillations can not be seen at this scale, only the signal envelope is shown. The North atomic beam signal is shown with a heavy line and the South is shown with a thin line. The lower box is the phase data extracted with a nonlinear curve-fit. Note that the departure from linearity at large rotation phase occurs when nearly at the edge of the contrast envelopes of the North and South atomic beams. The vertical offset of the bottom graph is arbitrary. The North and South contrast envelopes have a relative offset because the phase modulation effectively acts like an acceleration (see Equation 5.8).

fitting routine was extremely robust, and had virtually 100% success in fitting the curves. In contrast, for the frequency modulation technique, the six-parameter fits frequently failed to converge at first, and required special care in the code to ascertain the quality of the fit and retry repeatedly with adjusted initial guesses if necessary.

After determining φ_N and φ_S from the fits, the rotation and arbitrary phases were computed as:

$$\Phi_\Omega = (\varphi_N - \varphi_S)/2 \tag{6.13}$$

$$\phi_{\mathrm{arb}} = (\varphi_N + \varphi_S)/2 \tag{6.14}$$

Since the phases from the fit are undefined modulo 2π, the rotation and arbitrary phase are uncertain modulo π. The program added $\pm\pi$ as necessary for maximal continuity with the previous point, which is safe since the phase shifts change more slowly. The modulo π uncertainty means this technique cannot be used for measuring absolute rotation rates, unless an initial calibration is obtained. Since this can easily be done, for example, with the frequency modulation technique of section 6.5.1, this uncertainty is not a problem in practice.

6.6   Earth rotation rate measurement

To test the technique of using the difference between the North and South atomic beams to determine the absolute rotation zero, we measured the Earth rotation rate. We used the frequency modulation technique to electronically scan the effective rotation rate. The Doppler shift correction frequency δf was swept 400 Hz over 10 seconds, and the signal was phase modulated at 48 Hz so lock-in demodulation could be used for detection. The results are shown in Fig. 6.6. The time varying frequency shift δf was converted to an equivalent rotation rate using Equation 4.38. We took the difference of the North and South normalized signals, and fit the center of the curve to a sine wave. The point where the fitting curve crossed $y = 0$ was determined to be the zero rotation rate. (At this point, δf cancelled the Earth rotation rate.) We measured the Earth rotation rate to be $\Omega_{\mathrm{E}} = 7.24 \times 10^{-5}$ rad/sec, after correcting
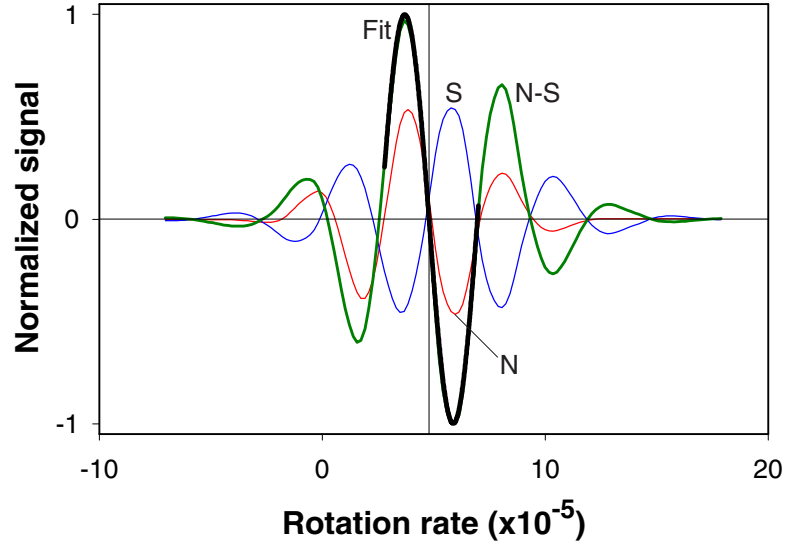
Figure 6.6: Absolute Earth rotation rate measurement (preliminary). The North and South rotation fringes are the symmetric signals shown with thin lines, the difference North−South is labeled N-S, and the fit to the center of the difference curve is shown with a heavy black line. From the fit, we determine $\Omega_{\mathrm{E}} = 7.24 \times 10^{-5}$ rad/sec.

the measured value by the factor of $\sin(\varphi_{\mathrm{lat}}) = 0.6602$ due to Yale's latitude. This is a preliminary measurement, as there were obvious sources of uncertainty we did not attempt to control. The expected value is $\Omega_{\mathrm{E}} = 7.29 \times 10^{-5}$ rad/sec, indicating a 0.7% error. Apart from systematic effects studied in Chapter 7, this measurement approach is sensitive to the following factors:

1. *Longitudinal tilt of the apparatus.* Longitudinal tilt (that is, rotation about the propagation axis of a Raman beam) only affects the signal through a change in the $\boldsymbol{\Omega} \cdot \boldsymbol{A}$ projection factor, whereas the signal is highly sensitive to transverse tilt due to the projection of $\boldsymbol{g}$. The projection factor depends on the atomic beam trajectories, which can only be measured indirectly. As previously described, each Raman beam was aligned to be centered on the atomic beam, and the atomic beams were aligned to counterpropagate. Therefore, one can determine the longitudinal projection factor by measuring the three Raman beam heights

relative to a horizontal plane defined by the tilt sensor, namely the leveled optical table. A 6 mrad (0.34°) tilt is required to explain the discrepancy observed. However, an earlier measurement of the beam heights indicated the beams were coplanar (to 0.1 mm measurement accuracy) with 2.5 mrad longitudinal tilt, in the direction opposite that required to explain the error.

2. *Delays.* The longitudinal velocities for the two beams differ slightly, as do the distances between the $\pi/2$ pulses and detection beams. That means there is a slight time offset between the output signals for the two beams. This effect could be compensated by extracting the data for positive and negative going rotation scans and averaging the two results, and can explain a $\sim 0.2\%$ error. This effect was reduced by using a slow frequency modulation rate.

3. *L.* At the time of this measurement, we had not yet used the digital caliper to measure L (see section 5.8.4). However, we had already achieved better than one part in 10^{-3} accuracy using a tape measure, so this was a minor problem.

This measurement marked the beginning of our exploration of absolute accuracy and stability for the instrument. Before completing a thorough error analysis or compensating for all known effects, we found a variety of factors that could potentially cause the apparent rotation phase to shift by up to $\sim 20\%$ of Ω_{E}. These systematic effects are primarily due to laser alignment issues. Chapter 7 compares the sensitivity to various possible sources of systematic error, and discusses experimental modifications that have dramatically improved immunity to these systematic effects.

Chapter 7

Noise and systematics

7.1 Beam detection noise comparison

To improve the interferometer signal-to-noise, we attempted to isolate the noise due to various individual components of the apparatus. A comparison of the detection noise for various configurations is given in Table 7.1. The values are rms divided by

Item	Configuration	Fractional noise $\times 10^{-5}$ $(\sigma/\mu/\sqrt{\text{Hz}})$
beam	no cooling	0.9
	2D cooling	0.6-3
π	coprop.	2
	counterprop.	3-5
$\pi/2$	coprop.	9
Ramsey	top of fringe	20-27
	side of fringe	40

Table 7.1: Atomic beam detection noise comparison.

the mean for a 1 sec interval.[1] The values or ranges given were fairly typical, yet because they were measured at different times, the ratios between quantities are not

---

[1]The Ramsey fringe values quoted represent rms fluctuations divided by the mean signal, whereas for computing the performance of the device as a clock as in section 7.2, we use rms fluctuations divided by the peak-to-peak Ramsey signal.
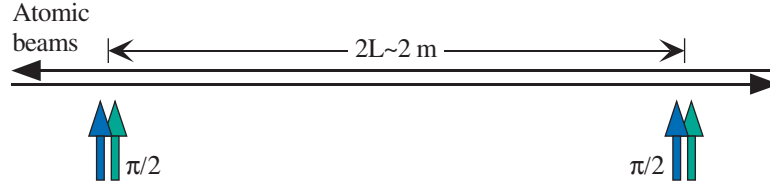
Figure 7.1: Ramsey excitation geometry.

exact. The π counterpropagating transition has more noise than the copropagating transition, which could be due to variations in the transverse velocity distribution of the atoms, or due to Doppler shifts from vibrations of the retroreflection mirror (since only one laser is reflected before driving the counterpropagating transition). The π pulse is quieter than the $\pi/2$ pulse, since ideally the π pulse has second-order sensitivity to pulse area fluctuations whereas the $\pi/2$ pulse has first-order dependence. As a practical matter, the π pulse advantage is reduced, since the pulse area condition can only be met in an average sense due to the longitudinal velocity distribution of the atomic beam.

7.2   Ramsey configuration (atomic clock)

One way to study the phase noise of our apparatus is to configure it as an atomic clock. This can be easily achieved by blocking the center π pulse and switching to copropagating Raman beams[2] using the $\dfrac{\pi}{2} - \dfrac{\pi}{2}$ Ramsey geometry shown in Fig. 7.1. We scanned the Ramsey interference fringe signal by varying the Raman detuning frequency using the 80 MHz AOM in the injection. Modulating the Raman detuning allowed us to synchronously detect the Ramsey signal with a lock-in amplifier. The demodulated signal is the derivative of the Ramsey signal, and is shown in Fig. 7.2. We used the signals from the two atomic beams to discriminate between changes in flux and changes in the rf frequency, which could be caused by drifts in the 10 MHz reference oscillator. This was done by adjusting the arbitrary phase between the

---

[2]The switching between co- and counterpropagating Raman transitions requires changing the frequency of Raman4 by 160 MHz, the shift that would normally occur in the retroreflection. This was done by adjusting the 80 MHz AOM in the injection from a +1 up-shift to a -1 down-shift, and readjusting the injection of Raman4.
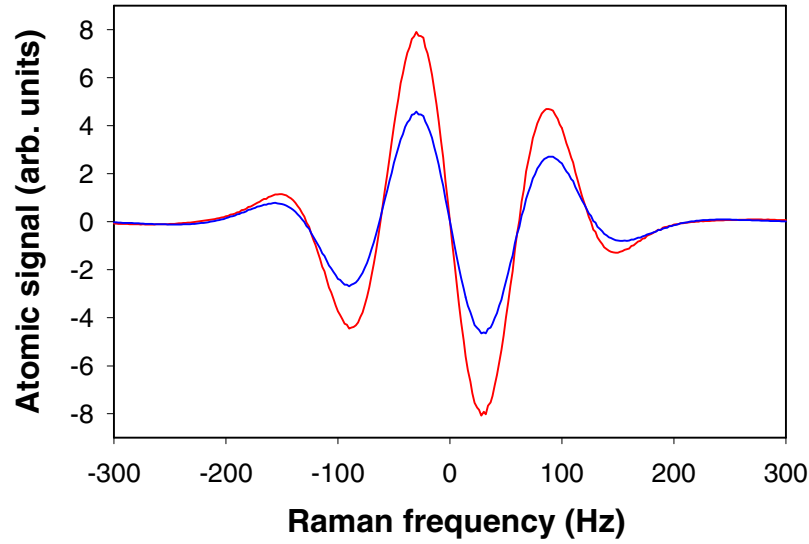
Figure 7.2: Ramsey fringe derivative signal.

interferometers so that the signals were anti-correlated, such that a frequency offset on the reference oscillator would cause both signals to change by opposite amounts. (Or, by adjusting the arbitrary phase, the signals could be made correlated.) Subtracting the two signals determined the degree of correlation and therefore the potential for noise rejection through the use of both signals. The arbitrary phase was adjusted by moving the beamsplitter that divided light between the two $\pi/2$ beams such that the Raman path lengths changed by a sizeable fraction of the ~ 3 cm rf wavelength.

The noise obtained when sitting at the center of the Ramsey fringe is shown in Fig. 7.3. The noise at 1.1 Hz may be due to mechanical vibrations of the beamsplitter translation stage used to adjust the arbitrary phase. To determine the stability, $\Delta\nu/\nu$, we computed the Allan variance of the noise.

The Allan variance (AVAR) is a statistical measure for characterizing the stability of a frequency source. It is convenient because the usual standard deviation diverges over time if the signal drifts. Given a sequence of N frequency measurements $\{f_i\}$
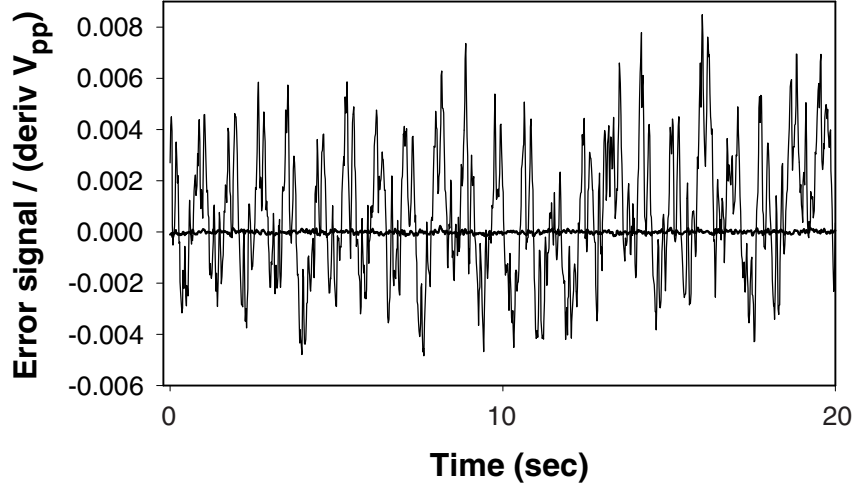
Figure 7.3: Ramsey fringe noise and difference signal. Since the signals were extremely well correlated, only the North beam and the difference North−South are plotted here. A modulation was applied to the Raman detuning at 50 Hz (using the AOM in the injection path of Raman4) and demodulation was done using a lock-in amplifier with a 0.03 sec time constant.

spaced by time interval τ, the AVAR, $\sigma^2(\tau)$, is defined as:

$$\sigma^2(\tau) \equiv \frac{\sum_{i=1}^{N-1}(f_{i+1} - f_i)^2}{2(N-1)(f_0)^2} \,, \tag{7.1}$$

where f_0 is the nominal oscillator frequency. Dividing by $2(N-1)$ makes $\sigma^2(\tau)$ equal the usual variance (that is, the standard deviation squared) if the individual frequency measurements are independent. Due to the subtraction, either frequencies or frequency errors can be used for $\{f_i\}$. The AVAR for various values of τ may be computed from one set of data by downsampling the data into various bin sizes. (This procedure results in the *modified* Allan variance.) We are usually interested in the standard deviation rather than the variance, and hereafter will use Allan variance or AVAR to refer to the square root of the modified Allan variance, namely $\sigma(\tau)$. Several types of Allan variance are discussed in [118, app. A].

The AVAR of the Ramsey difference noise discussed above is shown in Fig. 7.4.
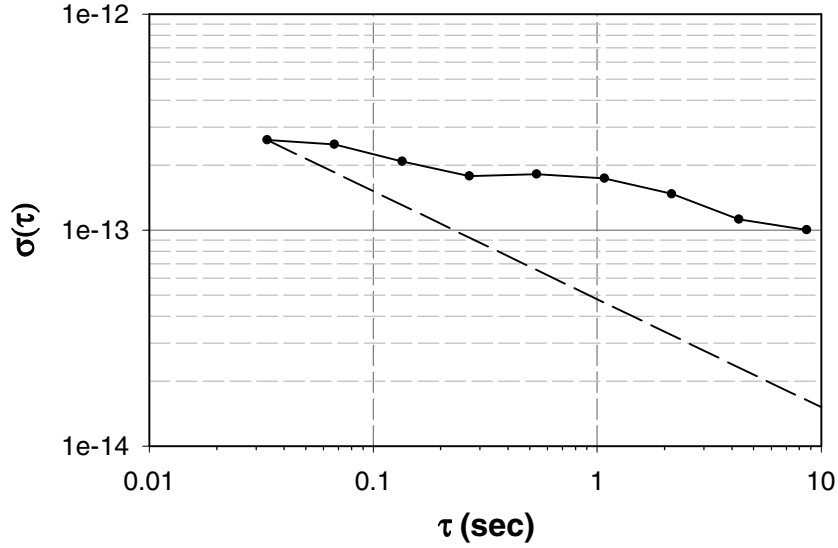
Figure 7.4: Ramsey Allan variance (clock configuration). The dashed line represents the $\sqrt{t}$ improvement expected for integration in the case of a shot-noise-limited signal. Sampling time $= 1/60$ sec, lock-in time constant $= 0.03$ sec.

Scaling the AVAR value from $1/30$ sec to 1 sec by $1/\sqrt{30}$, we find $\Delta f/f_0 = 4.8 \times 10^{-14}/\sqrt{\text{Hz}}$. In fact, the AVAR decreases more slowly than the shot-noise-limit, which indicates non-white spectral noise and may be partly due to residual effects of the ~ 1 Hz noise visible in Fig. 7.3. The stability achieved is competitive with atomic beam frequency standards; however, accuracy is a separate matter from stability, and we have not controlled possible systematic shifts carefully enough to achieve the high absolute accuracy required for a time standard. The Raman beam arbitrary phase dependence for the clock configuration is $\phi_1 - \phi_2$, compared to $\phi_1 - 2\phi_2 + \phi_3$ for the gyroscope. Therefore, the clock configuration is more sensitive to Raman phase noise than the gyroscope is, since there is no cancellation of overall phase at low frequency as for the gyroscope case.

7.3   Null area configuration

To study the performance of the interferometer independently of the rotational noise in our lab, we reconfigured the interferometer to have drastically reduced enclosed
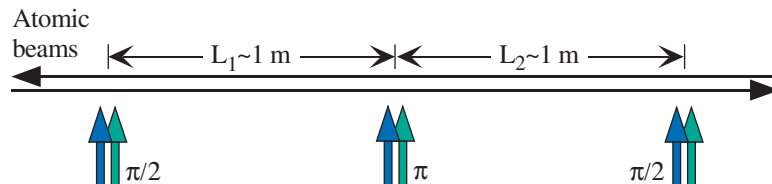
Figure 7.5: Null area interferometer excitation geometry.

area. By using copropagating Raman beams (rather than counterpropagating as in the gyroscope configuration), the interferometer enclosed area and sensitivity to rotation and acceleration are reduced by $k_{\mathrm{eff}}/k_{\mathrm{rf}} \simeq 1.3 \times 10^{-5}$. However, the sensitivity to many other sources of technical noise is unchanged; for example, phase shifts due to Zeeman shifts from changing magnetic fields, Raman pulse area or phase fluctuations, atomic beam flux, and ac Stark shifts. The excitation geometry for this configuration is shown in Fig. 7.5.

The Allan variance measured with this configuration is shown in Fig. 7.6. Demodulating the signal at 30 Hz removed long-term drift that lock-in detection of the signal could have removed in the gyroscope configuration. (In the null area configuration, the usual signal modulation techniques do not work.) We observed that taking the difference of the single atomic beam signals improved the noise by a factor of ~ 10, and yielded a signal-to-noise ratio of $50,000 : 1$ in 1 sec. This is a factor of 2 worse than expected for the shot-noise limit with 1×10^{10} atoms in the gyroscope signal. The signal-to-noise continues to improve like $\sqrt{t}$ to at least 10^4 sec. The null area configuration can also be used to equalize the Raman beam spacing (accurate to less than the Raman beam waist). If the position of the π pulse is adjusted, the sensitivity to Raman detuning is minimized when $L_1 = L_2$. In this case, there is no phase shift because atoms spend equal time in both states.

To study phase noise of the interferometer, we compared the noise of the null area configuration signal with that of a single π pulse (which has no phase sensitivity), as shown in Fig. 7.7. The comparison was made using a single atomic beam. The figure shows excess noise for the interferometer configuration at high frequency that decreases to the level of the π pulse at low frequency. The decrease is due to the phase cancellation between the three Raman beams for frequencies low compared to
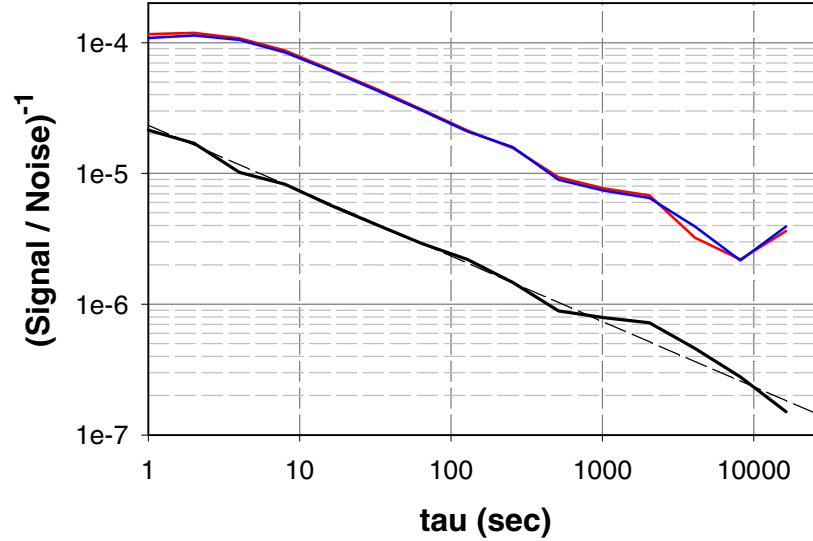
Figure 7.6: Null area configuration. A copropagating $\pi/2 - \pi - \pi/2$ Raman sequence was used to be insensitive to rotation and acceleration, yet sensitive to other technical noise. The top two traces (overlapping) are the AVAR from the North and South atomic beams individually and the bottom trace is the AVAR of their difference. Each trace has been normalized by the peak-to-peak Ramsey signal. The dashed line represents the $\sqrt{t}$ improvement expected upon integrating a shot-noise-limited signal. A lock-in amplifier was used to demodulate the signal at 30 Hz.
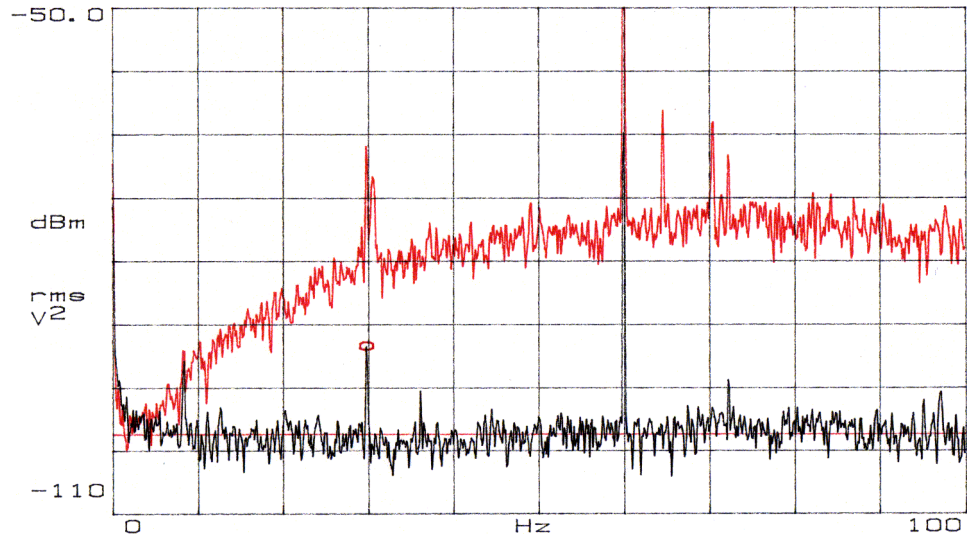

Figure 7.7: Null area interferometer vs. π pulse noise (power spectral density). The upper trace is the noise of the null area copropagating $\pi/2 - \pi - \pi/2$ configuration, and the lower trace corresponds to a single π pulse. (7.5 dB/division.)

v/L. This spectrum indicates that for taking long-term data where low bandwidth is acceptable, a low modulation frequency (i.e. ~ 3 Hz) should be used to reduce phase noise.

7.4   Systematics

We studied the sensitivity of the rotation-rate phase shift to various parameters, including the Raman master laser detuning, magnetic bias fields, Raman beam alignment, and transverse cooling alignment. This was done by continually acquiring data from both atomic beams using the phase modulation technique, and slowly varying the test parameter. Then the data were analyzed to measure the rotation-rate phase shift response.

7.4.1   Raman master laser detuning servo

Preliminary tests established that the detuning of the master Raman laser, which had been free-running, could cause a significant rotation-rate phase shift. Therefore, it was necessary to build a servo to lock the master laser detuning. We formed a beatnote between light from the Vortex laser lock and the Raman slave Raman4 by overlapping the beams on a fiber-coupled high speed photodiode (ThorLabs D400FC) using a connectorized collimating lens to couple the light into the fiber. The beatnote frequency is equal to the global Raman detuning, Δ, which was typically 2.2 GHz. Before adding the lock, we only had an approximate knowledge of the detuning, by measuring relative to cesium lines and assuming linearity of the master laser current. We did not need a high bandwidth locking system, since the unlocked master laser detuning changes slowly, primarily due to room temperature fluctuations and laser controller drifts. The beatnote is monitored on an HP-53181A digital counter with a 3 GHz prescaler. The count value is sent over GPIB to a dedicated servo computer that digitally integrates the count rate error and outputs a correction voltage (through an SR810 lock-in auxiliary output). Because the integration is performed by adding the error to an accumulator variable each time through the servo loop, the gain is
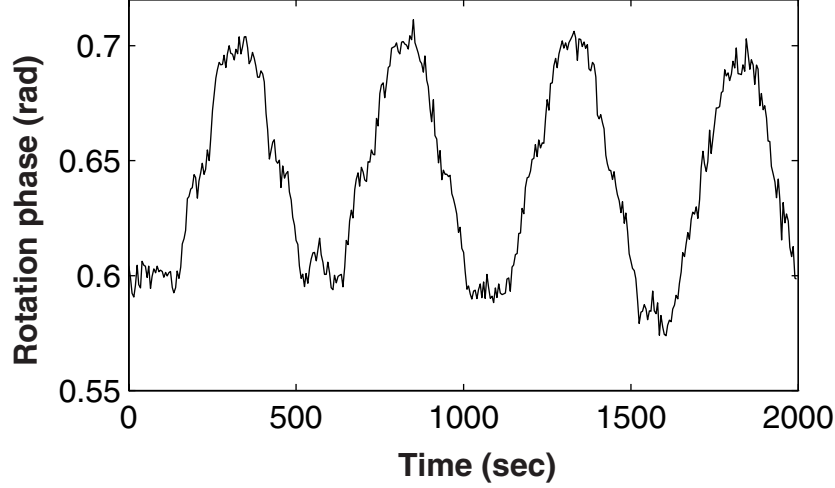
Figure 7.8: Rotation phase shift vs. Raman master laser detuning. This measurement was made by sinusoidally modulating the set-point of the master laser servo. The measured rotation rate sensitivity was $3 \times 10^{-5} \Omega_{\mathrm{E}}/\mathrm{MHz}$.

proportional to the update rate. Therefore, an adjustable gain factor was added to fine-tune performance. The servo loop runs as a separate thread of execution in the software and runs at a maximum rate of about 60 Hz, which is limited by GPIB transfer time.

The lock servo also included a mechanism for sinusoidally modulating the setpoint, which was used to quantify the systematic effect of the master laser detuning on the gyroscope phase, as shown in Fig. 7.8. For this measurement, the master laser was swept 0.5 GHz peak-to-peak with a period of 500 sec. We measured a peak-to-peak phase shift of 0.1 rad, and determined the rotation rate dependence[3] to be $3 \times 10^{-5} \Omega_{\mathrm{E}}/\mathrm{MHz}$. The servo error signal indicates 1.2 MHz rms residual frequency noise, which corresponds to rotation rate noise of $3.5 \times 10^{-5} \Omega_{\mathrm{E}}$. However, the detuning fluctuations are at high frequency and the average is locked precisely, so detuning no longer causes a systematic shift for long-term data acquisition.

---

[3]We have converted an interferometer phase shift to a rotation rate by dividing by the 6.8 rad phase shift corresponding to Ω_{E}.

7.4.2   Raman injection lock

Because the optical power available for injection-locking the Raman lasers is only $< 30~\mu$W, the injection range is limited to ~ 1 GHz. To investigate whether limited injection range was a source of noise, we modulated the slave laser current as much as possible while still staying nominally injected (causing 0.5% power fluctuations). The rotation phase shift was < 0.01 rad.

7.4.3   Magnetic bias fields

We explored the sensitivity of the rotation signal to various magnetic bias fields used in the experiment. We used the phase modulation technique at a 48 Hz oscillation frequency to extract the rotation signal while slowly modulating a particular bias field. The data are shown in Fig. 7.9. All the bias fields in the experiment are controlled by HP-3610A power supplies, including the four-wire Raman bias and the Helmholtz coils for cancelling external magnetic fields in the cooling regions (3 pairs of coils at each end of the chamber). To modulate the bias field, a programmable supply was used (HP-E3614A) that had a voltage controlled current output. The rotation phase shift from varying the 2-D cooling Helmholtz coils is presumably the result of a change in the atomic beam direction because of the interplay between polarization gradient cooling and the magnetic field zero within the cooling region. We varied the current through pairs of Helmholtz bias field coils with a period of 500 sec, chosen to be substantially slower than the time of flight of the atoms through the apparatus. For the transverse Helmholtz coils (that cancel fields originating from and in the same direction as the Raman bias), a triangle-wave modulation from 0.65 to 0.95 A resulted in rotation phase shifts of 0.032 rad, or $1.6 \times 10^{-5}\Omega_{\rm E}$/mA. The vertical Helmholtz coils had the greatest effect, with a modulation from 0.28 to 0.58 A yielding a phase shift of 0.06 rad, or $3 \times 10^{-5}\Omega_{\rm E}$/mA. The Raman bias field had little effect, with a modulation from 2.4 to 3.0 A causing a ~ 0.01 rad shift, or $2 \times 10^{-6}\Omega_{\rm E}$/mA.

To estimate the effect of bias field fluctuations on gyroscope performance, we can compute the change in current required to yield rotation signals comparable to our present short term sensitivity of 6×10^{-10} rad/sec in 1 sec integration. For the worst
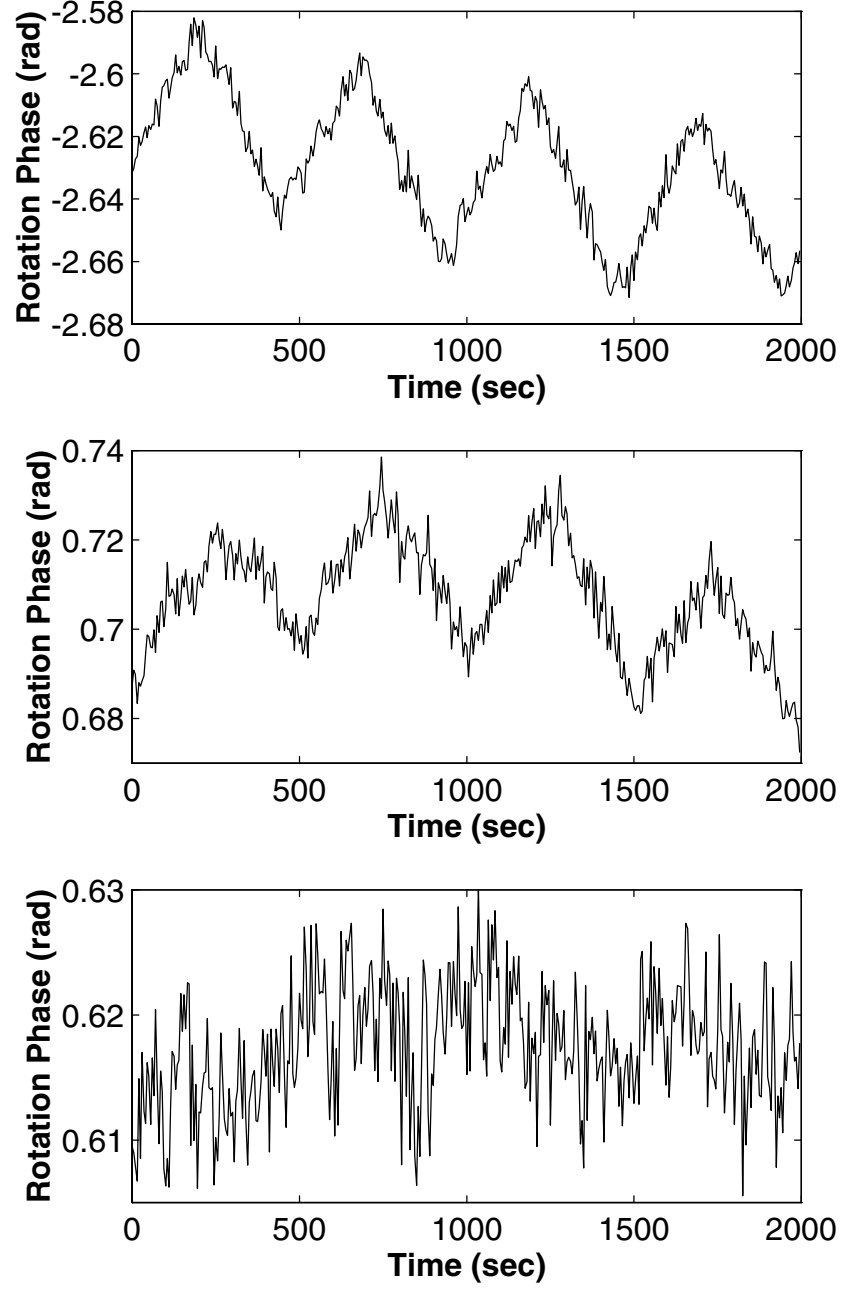
Figure 7.9: Rotation phase shift vs. cooling and Raman bias B fields. Field modulated with 500 sec period for each plot. Top: cooling transverse Helmholtz coil $(1.6 \times 10^{-5} \Omega_{\mathrm{E}}/\mathrm{mA})$. Middle: cooling vertical Helmholtz coil $(3 \times 10^{-5} \Omega_{\mathrm{E}}/\mathrm{mA})$. Bottom: Raman bias field $(\sim 2 \times 10^{-6} \Omega_{\mathrm{E}}/\mathrm{mA})$.

case of the vertical coils, current fluctuations of 0.28 mA in 1 sec would give noise comparable to our rotation sensitivity. However, we measured the HP-3610 power supply noise to be 7×10^{-3} mA rms ripple in 1 sec. Therefore, bias field stability is not presently a limiting factor for short-term or long-term performance.

7.4.4 Temperature

We monitored the temperature inside the top of the enclosure during an overnight run while taking data using the phase modulation technique at 48 Hz. The result is shown in Fig. 7.10. The optical table was still floating on pneumatic legs at this point, and electronic instruments located underneath the table enclosure (HP8770A, etc.) were later discovered to be heating the enclosure, raising its temperature by several degrees. (Improved temperature stability within the enclosure was an unexpected benefit of lowering the optical table to the floor.) The temperature was monitored using a thermistor inside the enclosure. Though inconclusive, the result suggests a correlation between arbitrary phase and temperature. Stainless steel has a thermal expansion coefficient $\alpha = 1.7 \times 10^{-5}$, where $\Delta L / L = \alpha \Delta T$. Therefore, for a characteristic length scale of $L \sim 1$ m, the 25 rad arbitrary phase drift observed could be explained by a $\sim 0.2°$C temperature change. Because the size of the phase shift depends on the details of the temperature gradients, it is difficult to predict how large an effect will be observed. The most likely source of temperature-induced phase shifts is motion of the Raman4 retroreflection mirrors along the axis of $\boldsymbol{k}_{\text{eff}}$ by differing amounts for the three Raman beams due to a temperature gradient.

7.4.5 Raman laser pointing

We studied the rotation phase shift sensitivity to various types of Raman beam misalignments for one of the $\pi/2$ beams. Fig. 7.11 shows the effect of changing the retroreflection angle. At the time of this measurement, only Raman4 was reflected, so changing this angle offset the counterpropagating Raman beams, leading to an ac Stark shift. Adjusting the horizontal direction causes a Doppler shift of the transition and causes atoms to see one Raman beam before the other (reversed for the
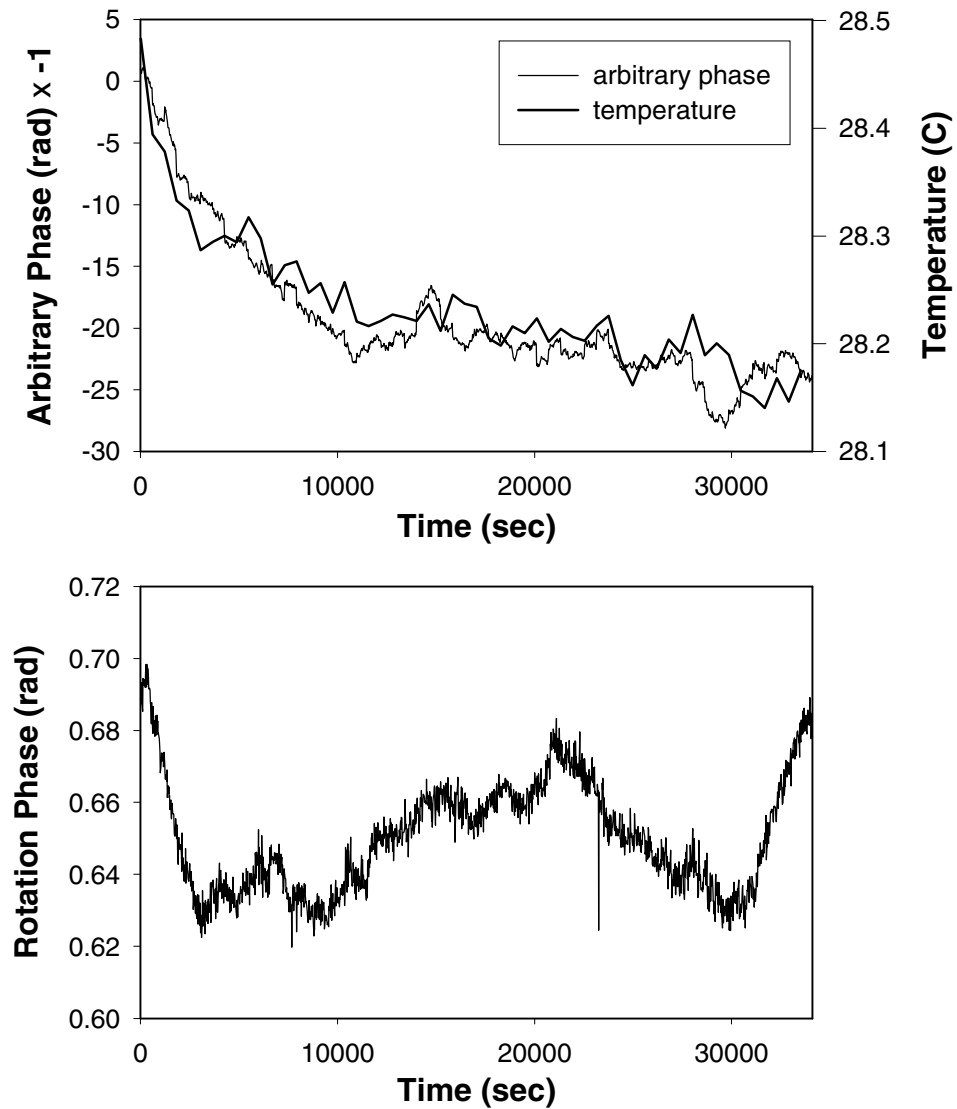
Figure 7.10: Gyroscope response to temperature changes. The temperature was monitored inside the table enclosure while taking data with 48 Hz phase modulation. The arbitrary phase drift appears correlated with temperature, but the rotation signal is independent. The temperature vertical axis has been scaled for overlap with arbitrary phase.
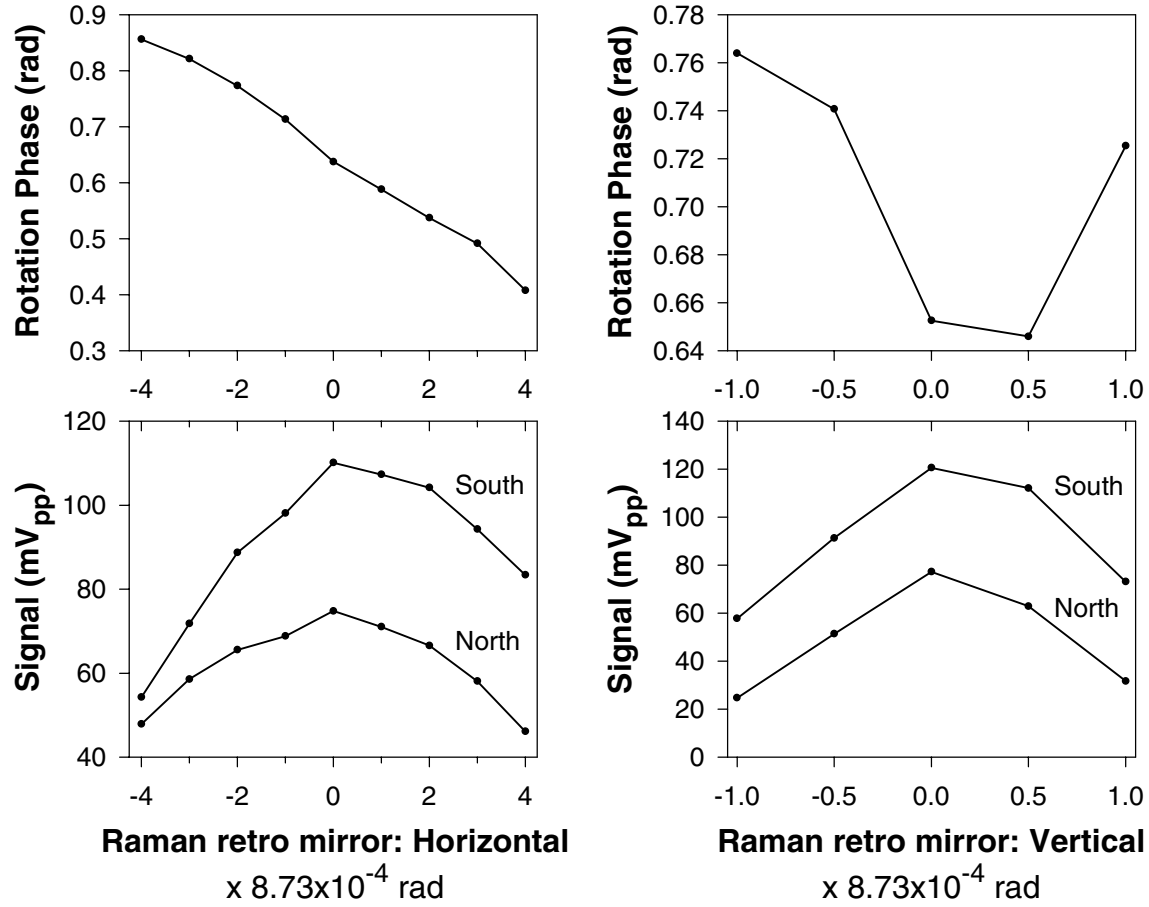
Figure 7.11: Rotation phase sensitivity to Raman retroreflection angle. The two graphs on the left correspond to misaligning the retro mirror horizontally, and the graphs on the right correspond to vertical misalignments. The upper two graphs show the rotation phase shift, and the lower two graphs give the peak-to-peak fringe signal size.
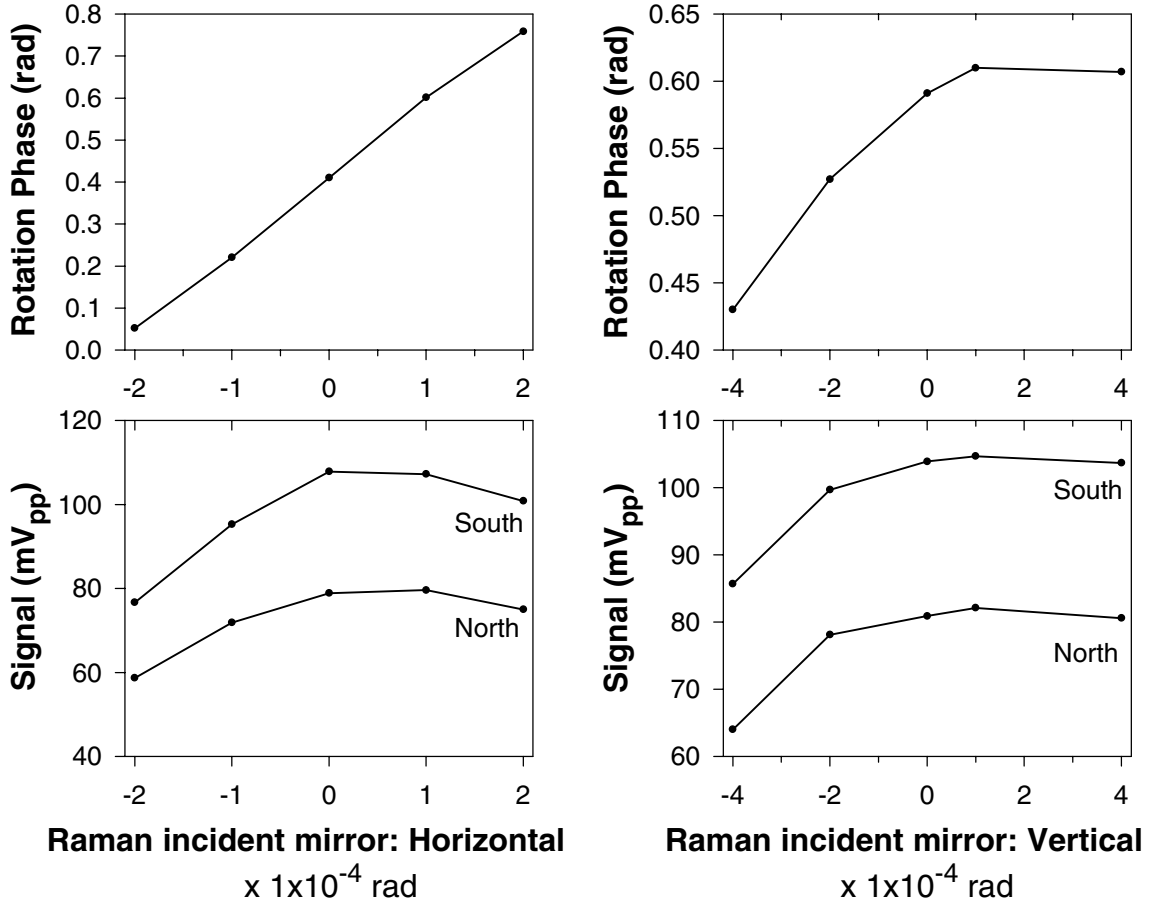
Figure 7.12: Rotation phase sensitivity to Raman angle of incidence.

two atomic beam directions). For horizontal misalignment, the rotation phase shift is approximately linear and changes sign when the beam is nominally aligned correctly. Each rotation phase shift point corresponds to 1 minute of 48 Hz phase modulation data. The lower graphs represent a rough measurement of the peak-to-peak contrast, included to indicate how large a phase shift might occur after optimizing the gyroscope signal.

Similarly, Fig. 7.12 shows the effect of misaligning the final incident Raman mirror that directs both Raman lasers into the chamber (toward the retroreflection mirror moved in the previous figure). In this case, initially the two Raman lasers move together, staying superimposed. However, since only Raman4 was retroreflected at
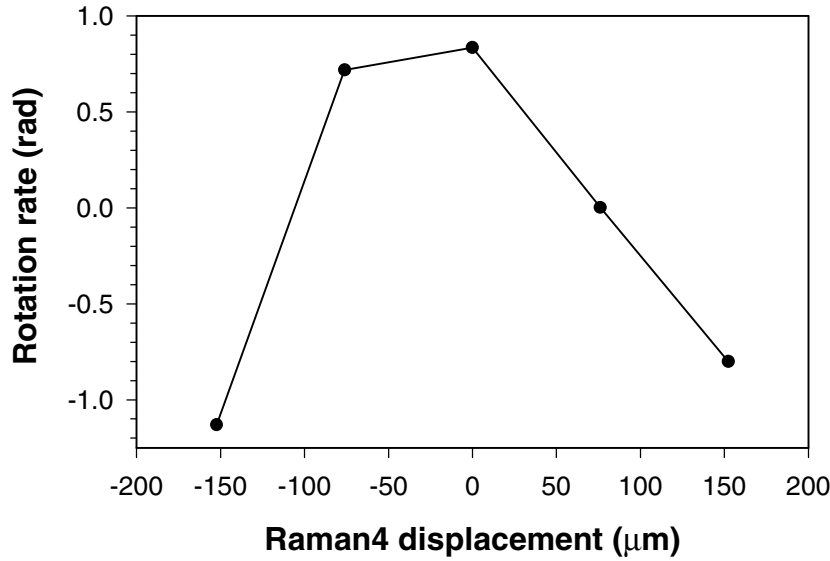
Figure 7.13: Rotation phase sensitivity to Raman beam displacement. The relative alignment of Raman3 and Raman4 was changed by adjusting the angle of Raman4 with the final mirror used to overlap Raman3 and Raman4 on a polarizing beamsplitter cube. Quadrant detectors were used to quantify the position and direction change of Raman4.

the time of this test, there is a relative offset between the counterpropagating beams, causing an ac Stark shift as above. For a given angular misalignment, the phase shift due to the incident mirror is larger than that due to the retroreflection mirror, but because the signal contrast also changes more quickly with incident mirror misalignment, the incident and retroreflection mirror misalignments are likely to cause comparable phase shifts upon optimizing the gyro signal.

Finally, we tested the importance of the relative superposition of the two Raman lasers by changing the alignment of Raman4 alone to vary its position and direction. The result is shown in Fig. 7.13. The horizontal offset was found to cause a large phase shift of ± 1 rad or $\pm 0.15\Omega_{\mathrm{E}}$. This was a major impetus for the Raman fiber-optic coupling scheme that was adopted, described in section 7.5.1.

We studied the pointing stability of the light from the laser diode and collimation system using a quadrant detector. After improving the mounting mechanics, the laser pointing drift was reduced to ~ 10 μrad over 12 hours. Once the lasers were
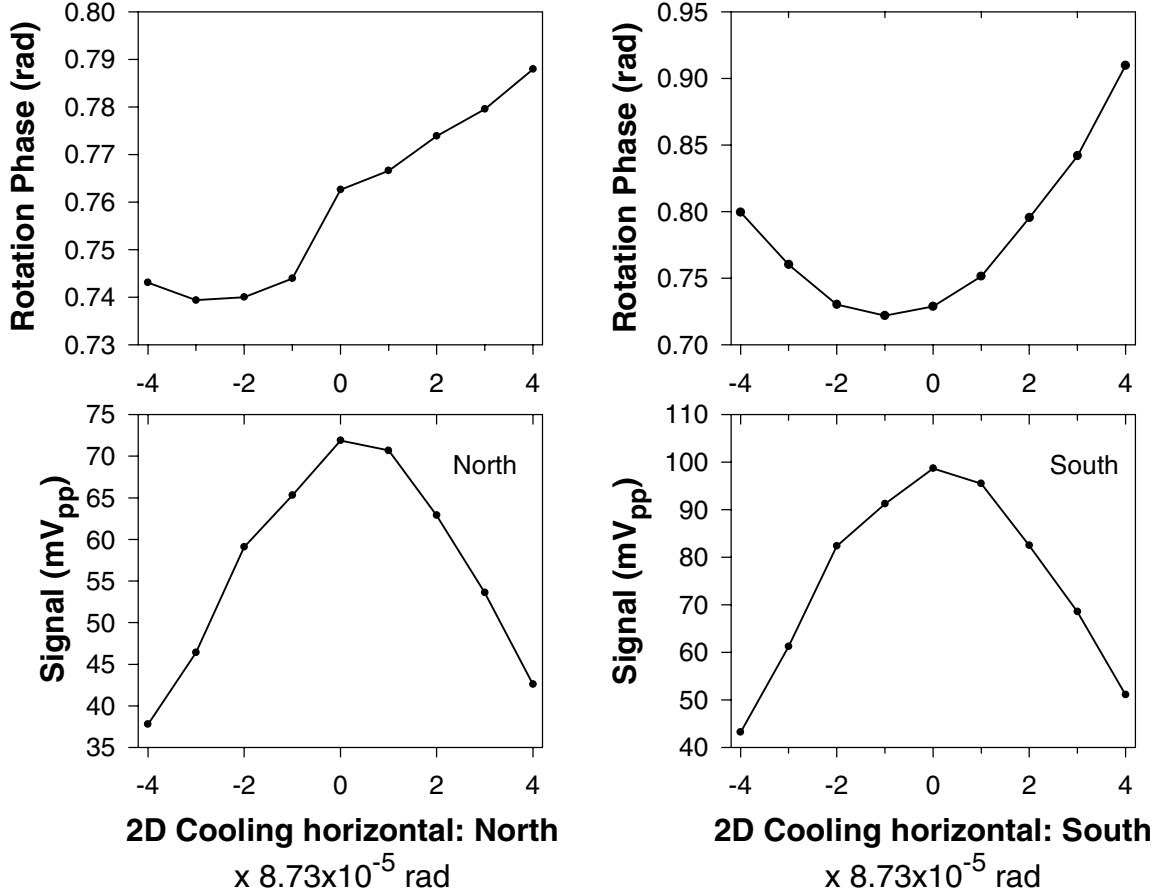
Figure 7.14: Rotation phase sensitivity to atomic beam direction. The horizontal cooling retroreflection mirror for the North and South atomic beams were separately adjusted to steer the atomic beam direction.

fiber-coupled and intensity stabilized, this drift was no longer significant.

7.4.6 Transverse cooling

We studied the effect of the transverse cooling alignment on the rotation phase shift by adjusting the horizontal cooling retroreflection mirrors for the North and South atomic beams. The result is shown in Fig. 7.14. The cooling misalignment caused a phase shift of ~ 0.2 rad, or $3 \times 10^{-2} \Omega_{\mathrm{E}}$. Presumably the shift is due to the resulting alignment change of the atomic beam relative to the Raman lasers, causing an ac Stark shift.

The shift due to the cooling beams should be larger if the Raman lasers are not well superimposed.

7.5 Stability improvements

The most serious systematic shifts we observed were due to Raman beam misalignments, which can cause ac Stark shifts. Section 7.5.1 describes two improvements that greatly reduce this effect. Section 7.5.2 presents a real-time rotation-rate readout technique that avoids the need for post-processing analysis of the data and is convenient for studying systematic effects.

7.5.1 Raman beam stability improvements

Fiber-coupling

To improve the relative beam alignment between the two Raman lasers, we combined the Raman beams in a polarization-maintaining optical fiber to deliver the light to the spatial filter. This guarantees that the two output beams are spatially overlapped and in the same direction. The cross-polarized Raman beams were coupled into the fiber with 75% efficiency, which left enough power to work at $\Delta \simeq 2.0$ GHz detuning. The output of the fiber was mounted on a rigid base using a modified mirror mount attached to a crossed-roller-bearing translation stage, providing angle and 2-D translation for aligning the light through the spatial filter and beam-shaping optics used previously.

Raman retroreflection

In the initial implementation of the Raman retroreflection PLL (described in section 5.8.3), we were retroreflecting only Raman4. In this case, even with the fiber guaranteeing relative alignment of the copropagating beams, a change in the pointing of both Raman beams together would cause Raman4 alone to be offset upon retroreflection, leading to ac Stark shifts and therefore phase shifts. To reduce this effect, the polarizing cube that had been used to split off the Raman3 light before the AOM

(see Fig. 5.18) was removed, so Raman3 would also be frequency shifted by the AOM and be retroreflected.

The frequency shifts were arranged so that only counterpropagating transitions using the retroreflected Raman4 beam were in resonance, and other combinations were off resonance by $\delta_{12} = +160$ MHz. The frequencies of the laser beams when incident (denoted by ν) and retroreflected (denoted by ν^*) are as follows:

$$\nu_3 = \nu_{\mathrm{ML}} + (\nu_{\mathrm{hfs}} + \delta_{\mathrm{synth}})/2 \tag{7.2}$$

$$\nu_4 = \nu_{\mathrm{ML}} - (\nu_{\mathrm{hfs}} + \delta_{\mathrm{synth}})/2 - \delta_{\mathrm{inject}}$$

$$\nu_3^* = \nu_3 + 2\delta_{\mathrm{retro}} \tag{7.3}$$

$$\nu_4^* = \nu_4 + 2\delta_{\mathrm{retro}}$$

where ν_{ML} is the Raman master laser frequency and δ_{synth}, δ_{inject}, δ_{retro} are the frequencies corresponding to the rf synthesizer detuning, the single-pass injection AOM frequency for Raman4, and the retroreflection double-pass AOM rf frequency, respectively. The desired combination is

$$\nu_3 - \nu_4^* = \nu_{\mathrm{hfs}} + \delta_{\mathrm{synth}} + \delta_{\mathrm{inject}} - 2\delta_{\mathrm{retro}} \,. \tag{7.4}$$

This is the only resonant possibility when the detuning frequencies are set as follows:

$$\delta_{\mathrm{inject}} = \delta_{\mathrm{retro}} = 80 \text{ MHz} \tag{7.5}$$

$$\delta_{\mathrm{synth}} = \nu_{\mathrm{rec}} + 80 \text{ MHz} \tag{7.6}$$

where $\nu_{\mathrm{rec}} = 8.265$ kHz is the recoil frequency shift required for energy conservation. In this case, $\nu_3 - \nu_4^* = \nu_{\mathrm{hfs}} + \nu_{\mathrm{rec}}$. (For copropagating transitions, the retroreflection beams were blocked, and the detunings $\delta_{\mathrm{synth}} = -\delta_{\mathrm{inject}} = 80$ MHz were used.)

Reflecting both Raman lasers ensures that they are always overlapped, and therefore the ac Stark shifts are approximately cancelled by the intensity ratio. The cancellation does not work perfectly, since the beams after the AOM have different detunings, which changes the required intensity ratio and makes it impossible

to completely cancel the ac Stark shifts for both the incident and the retroreflected light. Nonetheless, the ac Stark shifts still approximately cancel, as the 160 MHz shift is small compared to the $\Delta \simeq 2$ GHz Raman detuning. We observed a factor of ~ 7 improvement in long-term stability due to the addition of the fiber and the dual beam retroreflection.

Previously, we had used feedback into the laser as a signature for retroreflection when aligning the lasers. After the addition of the fiber, retroreflection was optimized by maximizing the power of Raman4 coupled back into the fiber, measured by adding a $\lambda/2$ plate between the fiber and the combining polarizing beamsplitter cube to divert some power into the other port of the beamsplitter. Then the laser retro mirror vertical was slightly misaligned as needed to avoid feedback.

Raman intensity stabilization

After adding the fiber for the Raman beams, intensity fluctuations were observed at the output of the fiber that were thought to be etalon effects due to reflections from the ends of the fiber, despite the fact that the fiber ends are polished at an angle. The frequency spectra of the intensity noise and rotational noise were similar as well. To observe intensity noise fluctuations while acquiring rotation data, a polarization beamsplitting cube and two photodiodes were added at the position of the quadrant detector shown in Fig. 5.16, allowing both Raman beams to be monitored. A servo loop was added to stabilize the intensity of each Raman beam by driving a piezo to pivot a lever arm that partially blocks the laser beam before it enters the fiber. (The mode of the light is subsequently cleaned up by the fiber and spatial filter.) The servo was implemented using a dedicated computer that reads the intensities using GPIB controlled voltmeters, and outputs the appropriate piezo voltages. The piezos have only 15 μm maximum extension, so a $\sim$5 cm lever arm was used to increase the modulation depth. The servo was typically operated with a 20 Hz update rate while taking long-term data, but can operate at up to 100 Hz.

7.5.2   Real-time rotation readout

A readout mechanism was devised that would allow the rotation signal to be output in real-time, rejecting the acceleration and arbitrary phase. This was a useful diagnostic technique for exploring possible systematic effects. The North and South atomic beam signals were fed into separate digital lock-in amplifiers (SRS-SR810), with both lock-ins set to the same phase. The frequency of the π pulse retro AOM was offset by $\epsilon = 3.2/8$ Hz, so the interferometer outputs were modulated at 3.2 Hz. A separate synthesizer (referenced to the same external 10 MHz timebase) generated a 3.2 Hz reference that was input to both lock-ins. A computer continually monitored the signal output of the lock-in used for the North atomic beam, and adjusted the arbitrary phase of the interferometer to make the lock-in output zero. The arbitrary phase was adjusted through the phase of the π pulse retro AOM, by GPIB control of synthesizer SRS2. Recall that frequency and phase adjustments of the center π pulse are possible with the *independent* configuration listed in Table 5.1. Since the only difference in phase for the North and South signals is due to the Sagnac phase that has opposite sign for the two directions, the South signal is dephased from the reference by the Sagnac phase shift. The South lock-in gives a signal output proportional to this phase, which gives a real-time readout of the rotation rate. Even with the table lowered to the floor, a light touch on the side of the table was easily seen on the lock-in rotation output. (The real-time rotation readout technique was not used to acquire any of the data shown here.)

7.6   Long-term stability

The characterization of the long-term stability of the instrument is still underway, and we believe that major improvements can be made by studying correlations between the drift and various beam parameters. The latest long term stability data are shown in Fig. 7.15, which shows peak-to-peak rotation rate drifts of $3.2 \times 10^{-3}\Omega_{\mathrm{E}}$ over 14 hours. These data were taken using the fiber-optic Raman delivery and intensity stabilization described in the previous section.
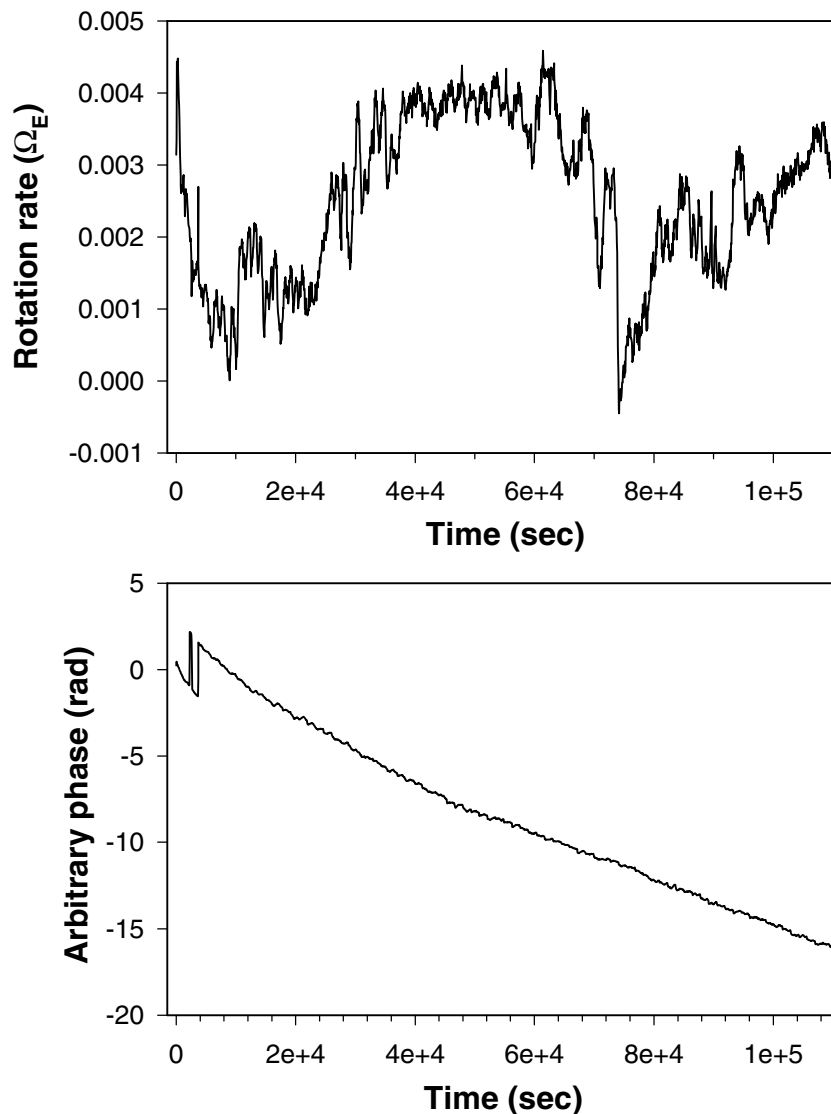
Figure 7.15: Recent long-term stability results. The Raman beams were fiber coupled with active intensity stabilization, and the optical table was resting on the floor. Phase modulation at 3.2 Hz was used with 100 samples per period, and the rotation phase was extracted using non-linear curve-fits. Each point plotted is 60 sec of data. The arbitrary phase data initially had discrete jumps because the measurement was made as a sequence of 20 minute acquisitions that did not start phase-synchronously. These jumps have been removed in post-processing. Note that there is no such effect on the rotation phase data, which is a useful confirmation of the data reduction method.
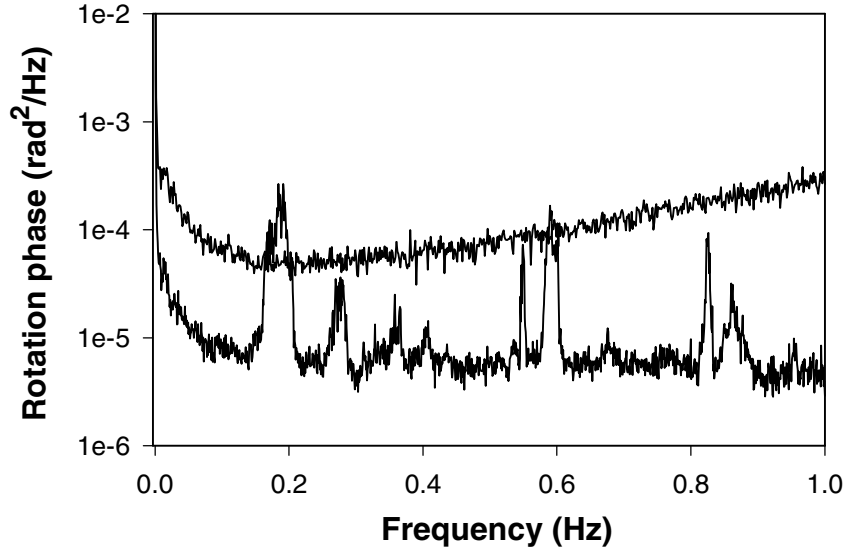
Figure 7.16: Power spectral density of rotation phase data. The bottom trace shows the data of Fig. 7.15, taken with fiber-coupled and intensity stabilized Raman lasers, the optical table resting on the floor, and 3.2 Hz phase modulation for data acquisition, using an FFT filter (described in the main text). The top trace shows a previous result with the optical table floating and without fiber-coupling or intensity stabilization for the Raman beams, using 48 Hz phase modulation for data acquisition. The increasing slope of the top trace is due to the floating table rotational resonance at 1.7 Hz.

The FFT of the data is shown in Fig. 7.16. For the rotation phase data, a filter was applied in the frequency domain as a post-processing step. This was done by taking the FFT of the data, and zeroing all frequency components outside a 6 Hz wide band centered at the modulation frequency. Then the inverse FFT was computed, and the curve-fits were performed in the time domain as usual to extract the rotation information. This filtering technique is discussed in [117]. Before performing the filtering operation on a particular segment of data, the mean of the segment was subtracted and zero-padding was added at the end of the segment to minimize ringing artifacts at the start and finish of each file due to wrap-around effects. (The filtering procedure is equivalent to performing a convolution between the raw data and the filter function, but implicitly assumes periodic data.) The ringing was not perfectly removed in the case of the arbitrary phase, since subtracting the mean does not zero the endpoints well when there is a linear drift. Therefore, the FFT filter technique
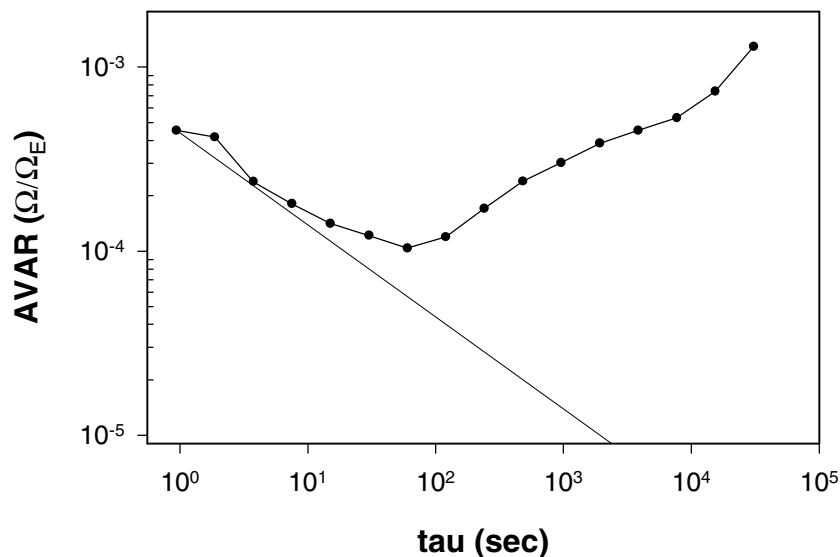
Figure 7.17: Rotation signal Allan variance.

was not used in plotting the arbitrary phase drift shown in Fig. 7.15. Though the FFT filter does do a good job of removing unwanted noise, it should be cautioned that filtering in the frequency domain does reduce the bandwidth of the time domain output, since the phase of the modulated signal cannot change quickly without high frequency spectral content. The curve-fitting procedure already rejects frequencies other than the modulation frequency to a large extent, therefore the FFT filter yielded only modest gains.

The Allan variance of the rotation signal (normalized by the Earth rotation rate) is shown in Fig. 7.17. The Allan variance stops improving at $\sim$ 100 sec, setting a practical limit on integration time. The fractional rotation noise at 1 second is higher than our estimated short-term sensitivity, but the AVAR result is subject to the rotational noise of the lab, which has not been independently characterized.

While examining the long-term performance of the instrument, we observed that the rotation signal was correlated with the phase modulated signal amplitude of the North atomic beam. This amplitude is proportional to the atomic beam flux, and although the curve-fits used to extract the data should be insensitive to this ampli- tude, the changes may correspond to pulse area or longitudinal velocity variations

that would cause a phase shift. The cause of these fluctuations and the resulting phase shift is still being investigated. If the rotation-rate signal is corrected by the North amplitude fluctuations, the drift is significantly reduced, as shown in Fig. 7.18. The correction was made by using a least-squares fit to determine the scaling factor for the amplitude data that gave maximum overlap with the rotation phase data, and subtracting the two curves. This compensated rotation rate signal was integrated to determine the net angular error, which corresponded to $\simeq 4.6 \times 10^{-2}$ degrees peak-to-peak over 30 hours. This is also shown in Fig. 7.18. The result is suggestive of oscillations with 24 hour period but longer acquisition times are needed to explore possible dependence on environmental parameters, such as thermal distortions of the building.

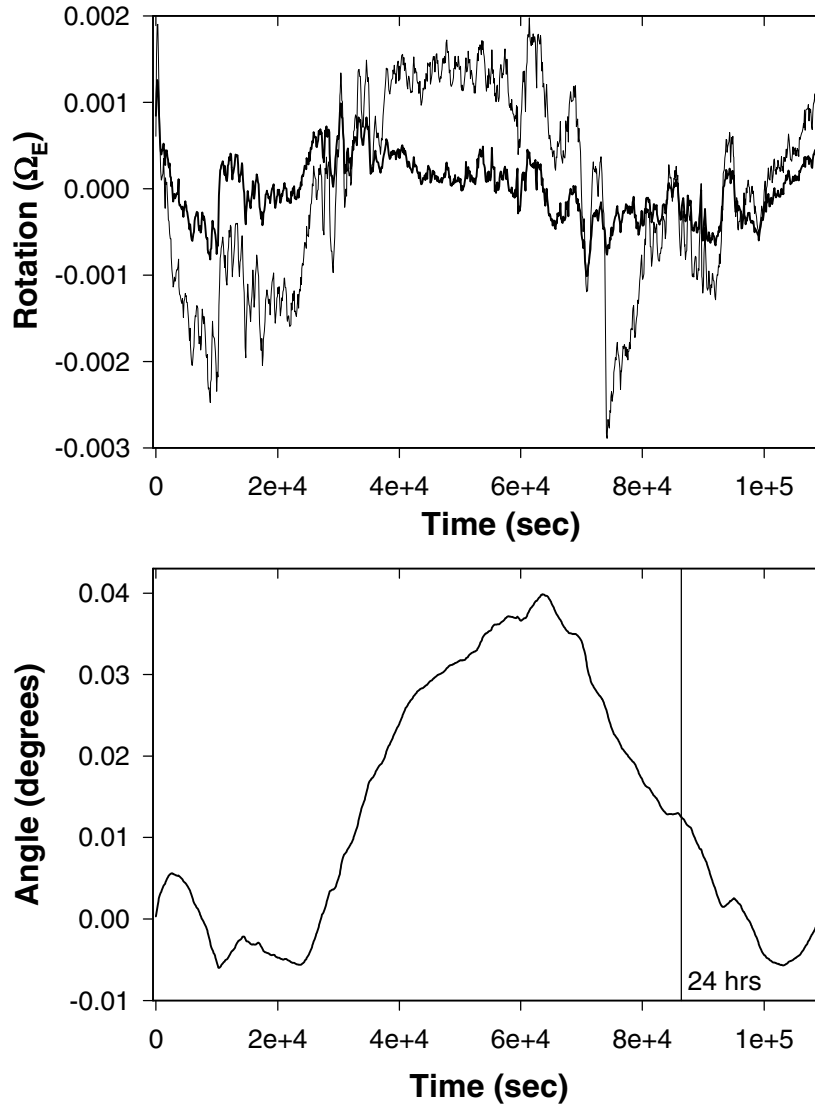Figure 7.18: Compensated drift. The top graph compares the rotation signal of Fig. 7.15 with the same signal after compensating for correlated fluctuations of the phase modulation amplitude of the North atomic beam. The raw data are plotted with a thin line, and the compensated data are plotted with a thick line. The bottom graph shows the integral of the compensated signal, which is a measure of absolute angular error over time.

Chapter 8

Conclusion

8.1 Summary

We have developed a gyroscope based on atom interferometry that currently has a short term sensitivity of 6×10^{-10} (rad/sec)/$\sqrt{\text{Hz}}$, which is the best sensitivity of any gyroscope reported to date. Long term stability requires further study, since we believe significant improvements still can be made with only modest changes to our current apparatus.

8.2 Current status

Our current sensitivity is still a factor of 3 away from the shot-noise limit of 2×10^{-10} (rad/sec)/$\sqrt{\text{Hz}}$ expected for the 10^{10} atoms/sec in the gyroscope signal, but we hope that further technical improvements will enable us to reach this level soon.

We are currently re-examining the factors that may be limiting the long-term performance of the device by looking for correlations between rotation phase shift and parameters such as Raman pulse area, Raman beam alignment drift, oven flux and velocity distributions, stray magnetic fields, etc. Though similar studies were done previously, many such tests must be redone after recent stability improvements such as coupling the Raman beams through a fiber, retroreflecting both Raman beams, and lowering the optical table to floor level.
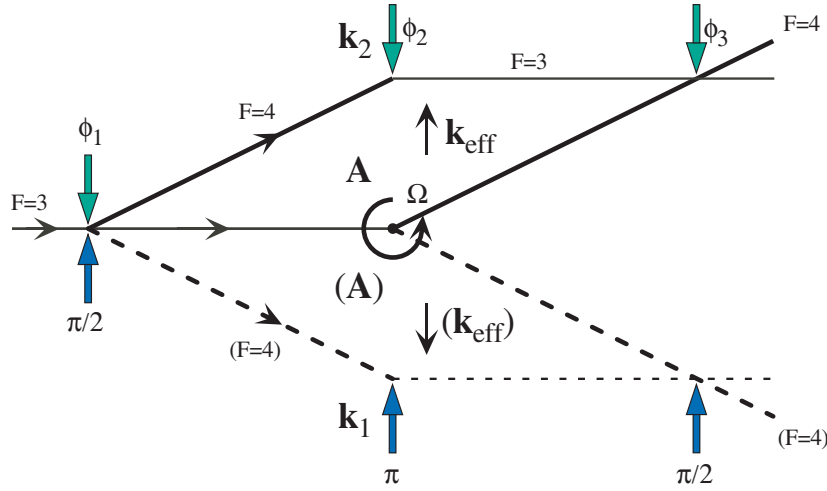
Figure 8.1: Area reversal. The upper loop labeled **A** represents the interferometer loop corresponding to Raman direction $\boldsymbol{k}_\text{eff}$ drawn in the upper loop. If the k-vector is reversed from $\boldsymbol{k}_\text{eff}$ to ($\boldsymbol{k}_\text{eff}$) as shown, the atoms follow the dashed interferometer paths with enclosed area labeled (**A**), instead. For clarity, only one atomic beam has been shown. Segments where the atoms are in the $F = 4$ state are shown with thick lines.

The instrument is still sensitive to Raman beam pointing variations, since the dual beam retroreflection technique does not completely compensate for ac Stark shifts from beam misalignments. Beam pointing can, in theory, be stabilized by adding piezos and servoing beam positions on quadrant detectors. In practice, it would be difficult to actively servo all relevant alignment parameters. Ultimately, distortions of the optical table with temperature fluctuations may be a limiting factor as well. An expensive but likely workable passive solution would be to follow the approach used in large ring lasers and use a monolithic block of Zerodur low thermal expansion glass with optically-contacted Raman beam delivery and retroreflection optics.

We hope to improve long-term performance substantially by repeatedly reversing the interferometer area. By switching the direction of the Raman k-vectors, we reverse the direction of the momentum kick to the atoms and the sign of the vector area associated with the loop. This switch reverses the sign of the Sagnac phase shift, but many other potential sources of systematic shifts remain unchanged. Fig. 8.1 illustrates the area reversal geometry. It should be possible to switch rapidly between standard and

area-reversed configurations, but we can not do this without modifying our current setup. The 4.6 GHz AOM is only efficient over a limited frequency range (for a given alignment angle), or it could be used to reverse the area by shifting the Raman injection frequencies enough that the other retroreflected Raman beam (Raman3) was on resonance. A possible solution is to replace the retroreflection AOMs with electro-optic modulators (EOMs). EOMs can be operated at lower frequencies than AOMs (1 MHz versus 80 MHz), and the smaller frequency offsets would mean that the high frequency AOM could be detuned enough to reverse the area. Preliminary efforts to implement this technique are currently underway.

8.3 Future prospects

8.3.1 Long term integration

A goal for the near future is to observe variations in the Earth's rotation rate that occur at the $10^{-8}\Omega_{\mathrm{E}}$ level. There are two parallel approaches to this problem. One approach is to improve the long-term stability performance of the apparatus to ensure that the signal continues to improve like $\sqrt{t}$ upon integrating for long times, before the signal drift eventually dominates. The other approach is to improve short-term sensitivity. Because a shot-noise-limited measurement improves like $\sqrt{t}$, the integration time required to reach a particular sensitivity scales with the square of the short-term sensitivity. For example, with our current sensitivity, measuring an Earth rotation rate change of $10^{-8}\Omega_{\mathrm{E}}$ would require 400 hours of integration,[1] whereas at the shot-noise limit (only 3 times better sensitivity) we would require only 44 hours. Once shot-noise limited, an additional improvement by at least a factor of 2 in sensitivity (four times more atoms in the gyroscope signal) would allow us to see tidally induced variations in the Earth's rotation rate, on $\sim$ 12-hour time scales.

---

[1]If the apparatus were located near the pole, the time would be shortened to 190 hours.

8.3.2 Interferometry exploration

The present apparatus can be used to test interferometer techniques; for example, different types of beamsplitters, or the use of multiple pulses to increase the area of the interferometer. For multiple pulses, the simplest increase requires adding four extra π pulses to our current setup, and would increase the interferometer area by about a factor of three, but at significant expense in alignment complexity. This pulse scheme (which can be extended to larger numbers of pulses) is shown in Fig. 8.2. Note that the Raman beam propagation axis, $\boldsymbol{k}_{\mathrm{eff}}$, must be reversed for the four additional pulses.
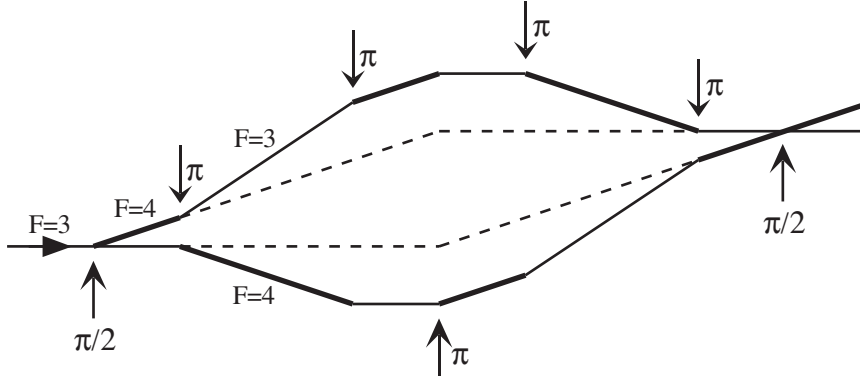

Figure 8.2: Multiple Raman pulse interferometer configuration. The counterpropagating Raman transitions are represented by a single arrow to emphasize the required direction changes for $\boldsymbol{k}_{\mathrm{eff}}$. Segments where the atoms are in the $F = 4$ state are shown with thick lines.

8.3.3 Compact instrument

We are interested in developing a more compact version of this device that would be portable for field testing or navigational use. A continuous slow atomic source such as the 2D-MOT configuration discussed in section 5.2 could be used to reduce the length of the apparatus while maintaining current levels of sensitivity. However, a standard atomic beam would result in higher bandwidth, would be simpler and more robust, and be better able to distinguish rotation from acceleration. Therefore, a standard beam is probably the best choice, at least for the first generation of portable devices.
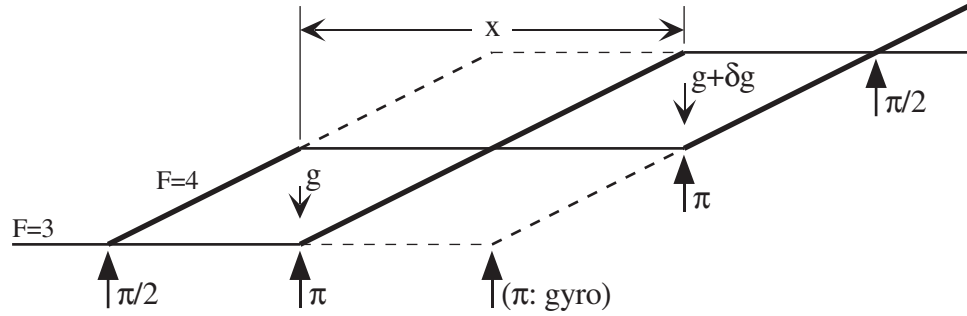
Figure 8.3: A figure-eight gravity gradiometer configuration could be readily implemented with an atomic beam. Each loop of the figure-eight measures g, and because the second loop is inverted from the first, the final signal yields the difference of the two acceleration measurements and determines $\mathrm{d}g/\mathrm{d}x$. A gradiometer could be integrated with a gyroscope and accelerometer by adding two extra π pulses to our existing configuration. Turning on the center beam labeled π:gyro in place of the two other π pulses would allow switching from the gradiometer to the gyroscope configuration. The dashed lines show trajectories used only for the gyroscope configuration.

An inertial navigation package could be made that measures rotations, accelerations, and gravity gradients, with modest modifications to our current design. Sensitivity along two axes could be obtained by adding orthogonal viewports and toggling laser beams between sets of windows, utilizing only one pair of counterpropagating atomic beams. One possible configuration is shown in Fig. 8.3. Unfortunately, our current vacuum chamber does not have viewports at the locations required for the extra π pulses in the gradiometer configuration. A gravity gradiometer based on atom interferometry has been demonstrated previously [30] that uses two MOTs with > 1 m separation. Because the MOT-based gradiometer makes two acceleration measurements simultaneously using shared Raman beams, common mode noise immunity to vibrations should be better than with the figure-eight configuration of Fig. 8.3, for which the acceleration is measured sequentially with the same atoms. Nevertheless, a beam-based device would operate at higher frequency, making it easier to average out vibrational noise. The sensitivity of this gradiometer configuration for a 5 m device could approach 1 $E/\sqrt{\mathrm{Hz}}$, where an Eötvös (E) is the standard unit of measurement for gravity gradients, and 1 $E = 10^{-9}$ sec^{-2}.

8.3.4   Longer instrument

Construction of a longer apparatus could be advantageous, since sensitivity scales as L^2. It should be feasible to increase the length of our interferometer from its present 2 m to $\sim$20 m, though admittedly this would pose difficult engineering challenges. Such a device could achieve more than 100 times our present sensitivity, and might make a ground based test of general relativity feasible. It would then be possible to achieve a sensitivity of $1 \times 10^{-9}\Omega_{\mathrm{E}}$ in less than 2 hours of integration, which would be useful for geophysical studies.

Appendix A

Detection photodiode circuit

This appendix describes the amplifier circuit used for the Hamamatsu S3590-01 Si-PIN detection photodiodes mentioned in section 5.7. The circuit used is shown in Fig. A.1. This circuit is based on a design and accompanying analysis given in an application note by Burr-Brown [119], with slight modifications. The main change is that in our case the photodiode is connected directly across the inputs of the amplifier and in the original design, the lead of the photodiode that we have connected to the inverting input is connected to ground, instead. With our implementation, the photocurrent causes a voltage drop across both 10 MΩ resistors, and the effective gain is twice that of the original design given the same feedback resistors. The resistor thermal noise is the same for equal gains with either circuit, but our configuration should have better immunity to bias currents and input offsets. The gain and bandwidth have also been modified. This appendix will not give a full analysis of the circuit, but will show that the amplifier's spectral response is different for signal and noise inputs, and will explain key aspects of the design.

We have used large feedback resistors (10 MΩ) for high current to voltage gain, since resistor thermal noise spectral density is equal to $\sqrt{4k_BTR}$, but signal gain is proportional to R, so signal-to-noise improves as $\sqrt{R}$ for increased R. The large feedback resistance means that care must be taken to avoid leakage current,[1] since

---

[1]Leakage current may be caused by imperfections in the op-amp, surface conductivity of the packaging, etc. and should not be confused with detector dark current.
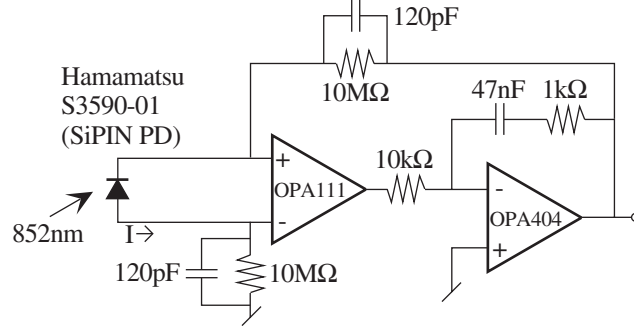
Figure A.1: Low noise detection photodiode circuit. The OPA404 amplifier inside the feedback loop reduces the bandwidth of the noise without reducing the signal bandwidth [119]. The bandwidth of the circuit is 133 Hz.
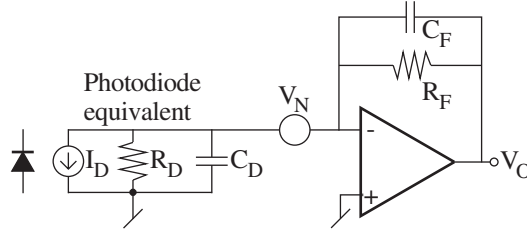

Figure A.2: Photodiode amplifier noise schematic. Here a simple inverting amplifier is used, and the photodiode is drawn as the parallel combination of a current source (I_D), resistor (R_D), and capacitor (C_D). V_N represents an input noise source.

leakage current shot-noise will experience the same large gain as the signal. For this reason, a FET OP amp, Burr-Brown #OPA111, was selected that has a low bias current of 1 pA. Photodiodes are often used with a reverse bias voltage to reduce the capacitance of the detector and increase its response time; however, this was unnecessary for our application, since the bandwidth of interest is sufficiently small.

The gain for the detector signal and the input noise to the op-amp have different spectral characteristics, and the gain for the noise actually increases at high frequency. To illustrate this gain peaking problem, consider the basic photodiode amplifier shown in Fig. A.2, where the photodiode is shown as its functional equivalent of a current source, resistor, and capacitor in parallel. The gain of the input noise source V_N can be computed at dc (capacitors are then open circuits) by a voltage divider argument, since $V_N = \dfrac{R_D}{R_F + R_D} V_O$. For the ac case, one must make the

replacements $R_D \rightarrow R_D||C_D = \dfrac{R_D/j\omega C_D}{R_D + 1/j\omega C_D}$ and similarly $R_F \rightarrow R_F||C_F$, where $j \equiv \sqrt{-1}$. Substituting and simplifying, we find the gain for the noise:

$$G = \frac{1 + j\omega R_F C_D}{1 + j\omega R_F C_F},$$ (A.1)

where $GV_N = V_O$ and we have made the approximations $C_F \ll C_D$ and $R_D \gg R_F$. According to Equation A.1, the noise gain varies from a minimum of 1 to a maximum of $\sim C_D/C_F$ as the frequency ω is increased. This can be quite high, as C_D=75 pF for our detector, and C_F might be simply stray capacitance in some cases. We have explicitly limited the signal bandwidth by using a large capacitance for C_F, since the signal gain rolls off at frequency $1/(2\pi R_F C_F)$. Current flows into a virtual ground at the op-amp input, so signal bandwidth is not limited by C_D or R_D.

The purpose of the OPA404 op-amp in Fig. A.1 is to filter frequencies above the signal cut-off, maintaining the bandwidth of the signal. At low frequencies, the OPA404 gives additional open loop gain and acts as an integrator, resulting in a second order filter. This must be rolled off before reaching unity gain to avoid oscillation, which is achieved by adding a resistor in series in the feedback of the OPA404. At high frequencies, the OPA404 feedback attenuates by a factor of 10. Note that the two op-amps are used with opposite polarities so the two in series give negative feedback. The net effect of using the two op-amps is that the overall voltage noise is reduced by a factor of ~ 3, to the level of the feedback resistor thermal noise.

Appendix B

PLL implementation

This appendix provides implementation details of the Raman laser retroreflection phase-locked loops mentioned in section 5.8.3.

B.1   RF reference generation

To generate the rf frequencies required as specified in Table 5.1, we mixed together the output of four synthesizers in the prescribed combinations. Since the PLL beatnote is at 160 MHz, the rf must be doubled from the values given in the table. Unequal rf values were chosen for the individual synthesizers so that when the synthesizer outputs are mixed together, the undesired combinations of carrier and harmonic frequencies end up outside the PLL bandwidth. We also avoided mixing together sources with shared harmonics, since that was determined to add noise. After each stage of mixing, unwanted harmonics were filtered. In some cases an extra stage of amplification was added for isolation between filtering stages. The particular scheme used is shown in Fig. B.1. Part labels refer to MiniCircuits components. BLP and BHP are low and high pass filters, respectively, and the number designates the nominal cut-off frequency. Triangles denote amplifiers, diamonds labeled 2X are doublers, unlabeled circles with a cross are 50/50 power splitters, circles with a cross labeled R/I/L are mixers, and the resistor symbol denotes an attenuator.
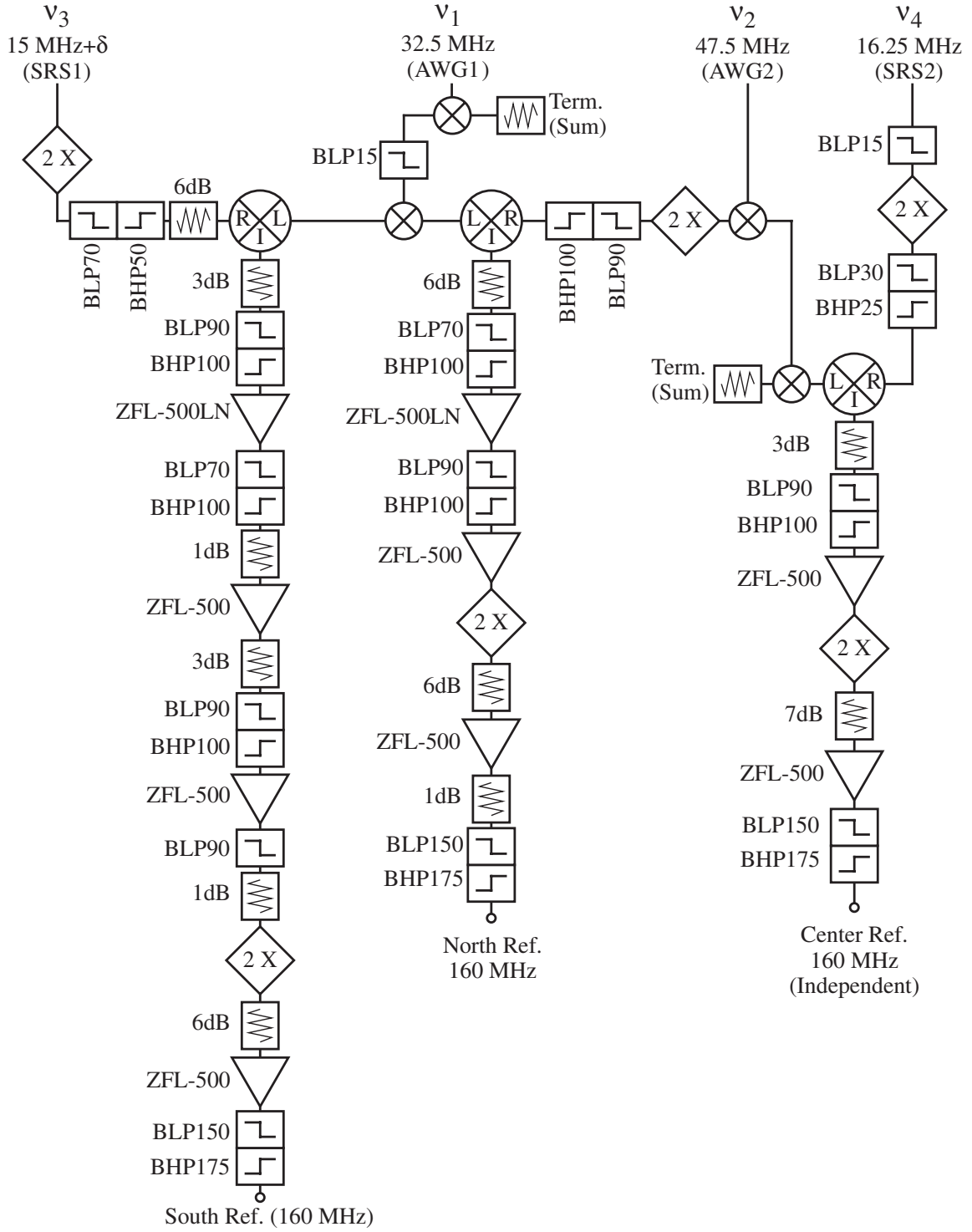
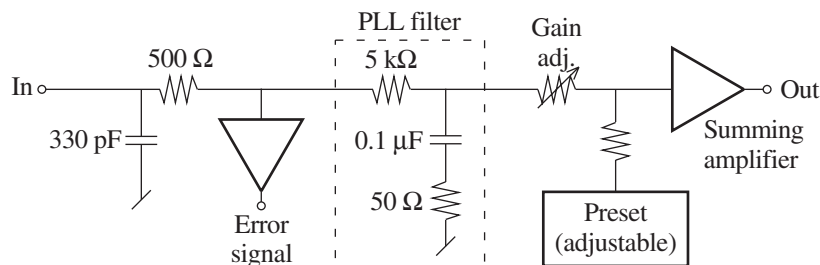Figure B.1: Raman laser PLL rf reference implementation.

Figure B.2: PLL filter circuit.

B.2   PLL filter circuit

This section gives a more detailed explanation of the PLL filter circuit (treated as a black box in Fig. 5.19). The circuit is shown in Fig. B.2. The output of the phase detector is input to this circuit, and the resistor and capacitor before the dashed box containing the main PLL filter are for impedance matching with the phase detector. The main PLL filter consists of a low pass filter that is an integrator. Since going from VCO frequency to the phase output of the phase detector is already one stage of integration ($\phi = \int \omega(t)\,\mathrm{d}t$), the low pass filter response must be rolled off at unity gain to avoid oscillation. This break is achieved by inserting a resistor in series with the capacitor to ground. This stage is followed by an op-amp summing amplifier that adds the signal (with adjustable gain) to a preset voltage. The preset is set before the PLL is locked, to make the VCO operate near the required frequency. The lock error signal was monitored after the phase detector, buffered by an op-amp.

Appendix C

Timing system

Because this experiment was originally intended to be operated in pulsed mode with cold atoms, a versatile timing system was developed to control multiple analog voltage output channels. Since the gyroscope experiment is now operated continuously, this system is only occasionally used to full advantage, for example when measuring longitudinal velocity distributions. Because the timing system has proven to be convenient for a variety of purposes (and in fact, has been adopted by several other research groups), it will be briefly described here. The principal component of the system is the National Instruments AT-AO-10 board which supports 10 analog output channels with 12-bit output from -10 to +10 V. This board has an output buffer, and accepts an external trigger to advance (cyclically) to the next set of analog output values. Multiple boards can be used if more output channels are desired. Several National Instruments PC-TIO-10 timing boards were used to trigger one or two analog boards, all of which were installed in a dedicated computer. The timing boards contain ten 16-bit counters that can be programmed and used as timers with various timebases. To maximize timing resolution, counters are triggered from the previous counter rather than from the beginning of the cycle. The first counter generates a repeating square wave that triggers the entire cycle repeatedly. The timing edge pulses are logically ORed together by external logic chips, and an active low pulse is fed to the trigger input of all the analog boards. Once configured, everything runs independently in the hardware with no further supervision needed from the software.

Two counters are used for video triggering, generating a pulse train at 15.75 kHz for video horizontal synch and a vertical synch pulse at the beginning of each timing cycle. When synchronizing with a CCD, the software quantizes the cycle length in units of video frames. These pulses can be used to synchronize a Philips CCD camera to the cycle, so the shutter opens at a fixed time relative to the beginning of the cycle.

With four timing boards, nearly 40 timing edges could be defined, and each analog output can be changed at each timing edge. The system has 1 μsec time resolution, with a minimum of 10 μsec between timing edges. Software to drive the boards was written in C, and required some low level register manipulation on the timing boards, due to deficiencies in the National Instruments high level routines. The user interface was done in MatLab, which called the C code as needed. One defect in the system is that the timing board square wave function does not behave properly until after completing the first cycle. This means that one needs to wait one cycle before any changes are properly reflected, which is a problem for long cycle times. Using an external GPIB controlled function generator to make the square wave that defines the cycle length would likely solve this problem.

To facilitate changing rf frequencies synchronously with the rest of the timing system, two digitally controlled frequency synthesizers (SCITEQ #VDS1306) are wired to two sets of latches in series, set by digital signals taken directly from the pins of two D/A chips on the analog board. The latches are clocked by the analog external update line and are needed to store the digital values and to add a delay, since the D/A chip inputs are set one trigger ahead. To set the desired frequency, the program asserts the analog voltage output that corresponds to the desired digital outputs. The synthesizers can be driven by an external 10 MHz input, and provide a stable alternative to a voltage controlled oscillator (VCO). The SCITEQ synthesizers were used to generate the rf for the detection and cooling AOMs. They were originally used to control frequencies for a moving molasses, to launch atoms from a MOT.

Appendix D

Selected numerical values

Quantity	Symbol	Value (SI)	
Planck's constant/(2π)	$\hbar$	$1.054\,572\,66(63)$	10^{-34} J sec
Velocity of light	c	$2.997\,924\,58(*)$	10^{8} m/sec
Boltzmann constant	k_B	$1.380\,658(12)$	10^{-23} J/K
Bohr magneton	μ_B	$9.274\,015\,4(31)$	10^{-24} J/T
Atomic mass unit	amu	$1.660\,540\,2(10)$	10^{-27} kg
Electron charge	e	$1.602\,177\,33(49)$	10^{-19} C
Gravitational constant	G	$6.672\,59(85)$	10^{-11} m^{3}kg^{-1}sec^{-2}
Accel. due to gravity on Earth	g	9.8	m/sec^2
Earth mass	M	5.98	10^{24} kg
Earth equatorial radius	R	6.38	10^{6} m
Earth polar moment of inertia	I	$0.331\ MR^2$	
Earth rotation rate	Ω_E	7.292	10^{-5} rad/sec
Sidereal day		$86\,164.1$	sec

Table D.1: Selected numerical values. Numbers within parentheses indicate the 1σ uncertainty in the last digits, and * indicates a defined quantity. The fundamental constant values quoted in the top half of the table are the 1986 CODATA recommended values from Cohen and Taylor [120].

Appendix E

Cesium properties

Quantity	Symbol	Value (SI)	
Atomic number		55	
Atomic weight [121]		132.905 442(4)	amu
Nuclear spin	I	7/2	
Mass	m	2.206 948(2)	10^{-25} kg
Melting point		28	°C
$F = 3 \rightarrow 4'$ D_2 wavelength [122]	λ	852.347	nm
Natural linewidth	Γ	$2\pi \times 5.18$	MHz
Saturation intensity	I_{sat}	1.09	mW/cm^2
Clock transition frequency	ν_{hfs}	9.192 631 770(*)	GHz
Raman rf wavelength	λ_{rf}	3.24	cm
Recoil frequency	$\omega_{\mathrm{rec}} = \hbar k_{\mathrm{eff}}^2/2m$	$2\pi \times 8.265$	kHz
Two-photon recoil velocity	v_r	7.04	mm/sec

Table E.1: Cesium properties. Numbers within parentheses indicate the uncertainty in the last digits, and * indicates a defined quantity.

$$T < 302 \text{ K (solid)}: \quad \log_{10} P_{\mathrm{sol.}} = 10.5460 - 1.00 \log_{10} T - 4150/T$$
$$T > 302 \text{ K (liquid)}: \quad \log_{10} P_{\mathrm{liq.}} = 11.0531 - 1.35 \log_{10} T - 4041/T$$

Table E.2: Cesium vapor pressure [123], with pressure P in torr, and temperature T in Kelvin.

Bibliography

[1] J. Lense and H. Thirring, *Phys. Zeits.* **19**, 156 (1918).

[2] B. Mashhoon, F. W. Hehl and D. S. Theiss, "On the gravitational effects of rotating masses: The Thirring-Lense papers," *Gen. Relativ. Gravitation* **16**, 711–50 (1984). Translation from German and commentary.

[3] A. Lawrence, *Modern Inertial Technology: Navigation, Guidance, and Control* (Springer-Verlag, New York, 1998).

[4] M. Sagnac, *C. R. Acad. Sci.* **157**, 708 (1913).

[5] P. Storey and C. Cohen-Tannoudji, "The Feynman path integral approach to atomic interferometry," *J. Phys. II (France)* **4**, 1999–2027 (1994).

[6] D. Kleppner, "A short history of atomic physics in the Twentieth Century," *Rev. Mod. Phys.* **71**, S78–S84 (1999).

[7] D. Wineland and H. Dehmelt, *Bull. Am. Phys. Soc.* **20**, 637 (1975).

[8] T. W. Hänsch and A. L. Schawlow, "Cooling of gases by laser radiation," *Opt. Commun.* **13**, 68 (1975).

[9] S. Chu, L. Hollberg, J. E. Bjorkholm, A. Cable and A. Ashkin, "3-Dimensional viscous confinement and cooling of atoms by resonance radiation pressure," *Phys. Rev. Lett.* **55**, 48–51 (1985).

[10] P. D. Lett, R. N. Watts, C. I. Westbrook, W. D. Phillips, P. L. Gould and H. J. Metcalf, "Observation of atoms laser cooled below the Doppler limit," *Phys. Rev. Lett.* **61**, 169–72 (1988).

[11] J. Dalibard and C. Cohen-Tannoudji, "Laser cooling below the Doppler limit by polarization gradients: Simple theoretical models," *J. Opt. Soc. Am. B* **6**, 2023–45 (1989).

[12] P. J. Ungar, D. S. Weiss, E. Riis and S. Chu, "Optical molasses and multilevel atoms: Theory," *J. Opt. Soc. Am. B* **6**, 2058–71 (1989).

[13] E. L. Raab, M. Prentiss, A. Cable, S. Chu and D. E. Pritchard, "Trapping of neutral sodium atoms with radiation pressure," *Phys. Rev. Lett.* **59**, 2631–4 (1987).

[14] N. F. Ramsey, *Phys. Rev.* **78**, 695–9 (1950).

[15] R. Colella, A. W. Overhauser and S. A. Werner, "Observation of gravitationally induced quantum interference," *Phys. Rev. Lett.* **34**, 1472–4 (1975).

[16] S. A. Werner, J.-L. Staudenmann and R. Colella, "Effect of Earth's rotation on the quantum mechanical phase of the neutron," *Phys. Rev. Lett.* **42**, 1103–6 (1979).

[17] S. Altshuler and L. M. Frantz, "Matter wave interferometric apparatus," U.S. Patent 3761721 (1973).

[18] J. F. Clauser, "Ultra-high sensitivity accelerometers and gyroscopes using neutral atom matter-wave interferometry," *Physica B* **151**, 262–72 (1988).

[19] P. J. Martin, B. G. Oldaker, A. H. Miklich and D. E. Pritchard, "Bragg scattering of atoms from a standing light wave," *Phys. Rev. Lett.* **60**, 515–8 (1988).

[20] O. Carnal and J. Mlynek, "Young's double-slit experiment with atoms: a simple atom interferometer," *Phys. Rev. Lett.* **66**, 2689–92 (1991).

[21] D. W. Keith, C. R. Ekstrom, Q. A. Turchette and D. E. Pritchard, "An interferometer for atoms," *Phys. Rev. Lett.* **66**, 2693–6 (1991).

[22] F. Riehle, T. Kisters, A. Witte, J. Helmcke and C. J. Bordé, "Optical Ramsey spectroscopy in a rotating frame: Sagnac effect in a matter-wave interferometer," *Phys. Rev. Lett.* **67**, 177–80 (1991).

[23] M. Kasevich and S. Chu, "Atomic interferometry using stimulated Raman transitions," *Phys. Rev. Lett.* **67**, 181–4 (1991).

[24] M. Kasevich and S. Chu, "Measurement of the gravitational acceleration of an atom with a light-pulse atom interferometer," *Appl. Phys. B* **54**, 321–32 (1992).

[25] P. R. Berman (ed.), *Atom Interferometry* (Academic Press, San Diego, CA, 1997).

[26] D. S. Weiss, B. C. Young and S. Chu, "Precision measurement of $\hbar/m_{cs}$ based on photon recoil using laser-cooled atoms and atomic interferometry," *Appl. Phys. B* **59**, 217–56 (1994).

[27] B. Young, M. Kasevich and S. Chu, "Precision atom interferometry with light pulses," in Berman [25], pp. 363–406.

[28] A. Peters, *High Precision Gravity Measurements using Atom Interferometry*, Ph.D. thesis, Stanford University (1998).

[29] A. Peters, K. Y. Chung and S. Chu, "Measurement of gravitational acceleration by dropping atoms," *Nature* **400**, 849–52 (1999).

[30] M. J. Snadden, J. M. McGuirk, P. Bouyer, K. G. Haritos and M. A. Kasevich, "Measurement of the Earth's gravity gradient with an atom interferometer-based gravity gradiometer," *Phys. Rev. Lett.* **81**, 971–4 (1998).

[31] M. H. Anderson, J. R. Ensher, M. R. Matthews, C. E. Wieman and E. A. Cornell, "Observation of Bose-Einstein condensation in a dilute atomic vapor," *Science* **269**, 198–201 (1995).

[32] C. C. Bradley, C. A. Sackett, J. J. Tollett and R. G. Hulet, "Evidence of Bose-Einstein condensation in an atomic gas with attractive interactions," *Phys. Rev. Lett.* **75**, 1687–90 (1995).

[33] C. C. Bradley, C. A. Sackett and R. G. Hulet, "Bose-Einstein condensation of lithium: Observation of limited condensate number," *Phys. Rev. Lett.* **78**, 985–9 (1997).

[34] K. B. Davis, M. O. Mewes, M. A. Joffe, M. R. Andrews and W. Ketterle, "Evaporative cooling of sodium atoms," *Phys. Rev. Lett.* **74**, 5202–5 (1995).

[35] F. Dalfovo, S. Giorgini, L. P. Pitaevskii and S. Stringari, "Theory of Bose-Einstein condensation in trapped gases," *Rev. Mod. Phys.* **71**, 463–512 (1999).

[36] M. O. Mewes, M. R. Andrews, D. M. Kurn, D. S. Durfee, C. G. Townsend and W. Ketterle, "Output coupler for Bose-Einstein condensed atoms," *Phys. Rev. Lett.* **78**, 582–5 (1997).

[37] B. P. Anderson and M. A. Kasevich, "Macroscopic quantum interference from atomic tunnel arrays," *Science* **282**, 1686–9 (1998).

[38] I. Bloch, T. W. Hänsch and T. Esslinger, "Atom laser with a cw output coupler," *Phys. Rev. Lett.* **82**, 3008–11 (1999).

[39] B. F. Chao and R. D. Ray, "Oceanic tidal angular momentum and Earth's rotation variations," *Prog. Oceanog.* **40**, 399–421 (1997).

[40] P. Brosche and H. Schuh, "Tides and Earth rotation," *Surveys in Geophysics* **19**, 417–30 (1998).

[41] K. Lambeck, *The Earth's Variable Rotation: Geophysical Causes and Consequences* (Cambridge Univ. Press, 1980).

[42] P. Brosche and J. Sündermann (eds.), *Earth's Rotation from Eons to Days* (Springer-Verlag, 1990).

[43] G. E. Stedman, "Ring-laser tests of fundamental physics and geophysics," *Rep. Prog. Phys.* **60**, 615–87 (1997).

[44] P. Boynton and R. Newman (1999). Symposium on Experimental Gravitation, Uzbekistan.

[45] L. I. Schiff, "Motion of a gyroscope according to Einstein's theory of gravitation," *Proc. Nat. Acad. Sci.* **46**, 871–82 (1960).

[46] H. C. Ohanian and R. Ruffini, *Gravitation and Spacetime* (W. W. Norton, New York, 1994), second edition.

[47] C. W. Misner, K. S. Thorne and J. A. Wheeler, *Gravitation* (W. H. Freeman, New York, 1973).

[48] C. J. Bordé, A. Karasiewicz and P. Tourrenc, "General relativistic framework for atom interferometry," *Int. J. Mod. Phys. D* **3**, 157–61 (1994).

[49] C. W. F. Everitt, "The Stanford relativity gyroscope experiment (a): History and overview," in *Near Zero: New Frontiers of Physics* (W. H. Freeman, 1987), p. 570.

[50] I. Ciufolini, E. Pavlis, F. Chieppa, E. Fernandes-Vieira and J. Pérez-Mercader, "Test of general relativity and measurement of the Lense-Thirring effect with two Earth satellites," *Science* **279**, 2100–3 (1998).

[51] I. Ciufolini (1999). Symposium on Experimental Gravitation, Uzbekistan.

[52] C. M. Will, *Theory and Experiment in Gravitational Physics* (Cambridge Univ. Press, 1993).

[53] M. Cerdonio, G. A. Prodi and S. Vitale, "Dragging of inertial frames by the rotating Earth: Proposal and feasibility for a ground-based detection," *Gen. Relativ. Gravitation* **20**, 83–7 (1988).

[54] Y. Aharonov and D. Bohm, *Phys. Rev.* **115**, 485 (1959).

[55] C. H. Rowe, U. K. Schreiber, S. J. Cooper, B. T. King, M. Poulton and G. E. Stedman, "Design and operation of a very large ring laser gyroscope," *Appl. Opt.* **38**, 2516–23 (1999).

[56] K. Schwab, N. Bruckner and R. E. Packard, "Detection of the Earth's rotation using superfluid phase coherence," *Nature* **386**, 585–7 (1997).

[57] O. Avenel, P. Hakonen and E. Varoquaux, "Detection of the rotation of the Earth with a superfluid gyrometer," *Phys. Rev. Lett.* **78**, 3602–5 (1997).

[58] A. Lenef, T. D. Hammond, E. T. Smith, M. S. Chapman, R. A. Rubenstein and D. E. Pritchard, "Rotation sensing with an atom interferometer," *Phys. Rev. Lett.* **78**, 760–3 (1997).

[59] M. K. Oberthaler, S. Bernet, E. M. Rasel, J. Schmiedmayer and A. Zeilinger, "Inertial sensing with classical atomic beams," *Phys. Rev. A* **54**, 3165–76 (1996).

[60] A. Peters, K. Y. Chung, B. Young, J. Hensley and S. Chu, "Precision atom interferometry," *Philos. Trans. Roy. Soc. A* **355**, 2223–33 (1997).

[61] W. W. Chow, J. Gea-Banacloche, L. M. Pedrotti, V. E. Sanders, W. Schleich and M. O. Scully, "The ring laser gyro," *Rev. Mod. Phys.* **57**, 61–104 (1985).

[62] F. Hasselbach and M. Nicklaus, "Sagnac experiment with electrons: Observation of the rotational phase shift of electron waves in vacuum," *Phys. Rev. A* **48**, 143–51 (1993).

[63] S. Buchman, F. Everitt, B. Parkinson, J. Turneaure *et al.*, "Experimental techniques for gyroscope performance enhancement for the Gravity Probe B relativity mission," *Classical Quant. Grav.* **13**, A185–91 Suppl. S (1996).

[64] H. J. Metcalf and P. van der Straten, *Laser Cooling and Trapping* (Springer-Verlag, New York, 1999).

[65] G. K. Woodgate, *Elementary Atomic Structure* (Oxford, 1980).

[66] L. Allen and J. H. Eberly, *Optical Resonance and Two-Level Atoms* (Dover, New York, 1987).

[67] C. Cohen-Tannoudji, J. Dupont-Roc and G. Grynberg, *Atom-Photon Interactions: Basic Processes and Applications* (Wiley-Interscience, 1992).

[68] P. Meystre and M. Sargent III, *Elements of Quantum Optics* (Springer-Verlag, 1991), second edition.

[69] J. P. Gordon and A. Ashkin, "Motion of atoms in a radiation trap," *Phys. Rev. A* **21**, 1606–17 (1980).

[70] D. Wineland and W. Itano, *Phys. Rev. A* **20**, 1521 (1979).

[71] P. Tremblay and C. Jacques, "Optical pumping with two finite linewidth lasers," *Phys. Rev. A* **41**, 4989–99 (1990).

[72] B. Masterson, C. Tanner, H. Patrick and C. Wieman, "High-brightness, high-purity spin-polarized cesium beam," *Phys. Rev. A* **47**, 2139–45 (1993).

[73] M. Kasevich, D. S. Weiss, E. Riis, K. Moler, S. Kasapi and S. Chu, "Atomic velocity selection using stimulated Raman transitions," *Phys. Rev. Lett.* **66**, 2297–300 (1991).

[74] K. Moler, D. S. Weiss, M. Kasevich and S. Chu, "Theoretical analysis of velocity-selective Raman transitions," *Phys. Rev. A* **45**, 342–8 (1992).

[75] M. A. Kasevich, *Atom Interferometry in an Atomic Fountain*, Ph.D. thesis, Stanford University (1992).

[76] C. J. Bordé, "Atomic interferometry with internal state labeling," *Phys. Lett. A* **140**, 10–2 (1989).

[77] C. J. Bordé, "Atomic interferometry and laser spectroscopy," in *Laser Spectroscopy X*, edited by M. Ducloy, E. Giacobino and G. Camy (World Scientific, Singapore, 1992), pp. 239–45.

[78] R. P. Feynman and A. R. Hibbs, *Quantum mechanics and path integrals* (McGraw-Hill, New York, 1965).

[79] J. J. Sakurai, *Modern Quantum Mechanics* (Addison Wesley, 1985).

[80] H. Goldstein, *Classical Mechanics* (Addison Wesley, 1980), second edition.

[81] A. L. Fetter and J. D. Walecka, *Theoretical Mechanics of Particles and Continua* (Addison Wesley, 1980).

[82] R. Friedberg and S. R. Hartmann, "Billiard balls and matter-wave interferometry," *Phys. Rev. A* **48**, 1446–72 (1993).

[83] J. Ishikawa, F. Riehle, J. Helmcke and C. J. Bordé, "Strong-field effects in coherent saturation spectroscopy of atomic beams," *Phys. Rev. A* **49**, 4794–825 (1994).

[84] U. Sterr, K. Sengstock, W. Ertmer, F. Riehle and J. Helmcke, "Atom interferometry based on separated light fields," in Berman [25], pp. 293–362.

[85] C. J. Bordé, "Matter-wave interferometers: A synthetic approach," in Berman [25], pp. 257–92.

[86] G. I. Opat, "Interferometry with particles of non-zero rest mass: Topological experiments," in *Advances in Quantum Phenomena*, edited by E. G. Beltrametti and J.-M. Levy-Leblond (Plenum Press, New York, 1995), pp. 89–112.

[87] D. E. Pritchard, R. A. Rubenstein, A. Dhirani *et al.*, "Longitudinal atom optics using localized oscillating fields: A fully quantum-mechanical treatment," *Phys. Rev. A* **59**, 4641–52 (1999).

[88] P. L. Gould, G. A. Ruff and D. E. Pritchard, "Diffraction of atoms by light: The near-resonant Kapitza-Dirac effect," *Phys. Rev. Lett.* **56**, 827–30 (1986).

[89] R. Neutze and F. Hasselbach, "Sagnac experiment with electrons: Reanalysis of a rotationally induced phase shift for charged particles," *Phys. Rev. A* **58**, 557–565 (1998).

[90] C. J. Bordé, N. Courtier, F. du Burck, A. N. Goncharov and M. Gorlicki, "Molecular interferometry experiments," *Phys. Lett. A* **188**, 187–97 (1994).

[91] C. J. Bordé and C. Lämmerzahl, "Atomic interferometry as two-level particle scattering by a periodic potential," *Annalen der Physik (Leipzig)* **8**, 83–110 (1999).

[92] C. Lämmerzahl and C. J. Bordé, "Atomic interferometry in gravitational fields: Influence of gravitation on the beam splitter," *Gen. Relativ. Gravitation* **31**, 635–52 (1999).

[93] M. A. Kasevich, E. Riis, S. Chu and R. G. Devoe, "RF spectroscopy in an atomic fountain," *Phys. Rev. Lett.* **63**, 612–6 (1989).

[94] Z. T. Lu, K. L. Corwin, M. J. Renn, M. H. Anderson, E. A. Cornell and C. E. Wieman, "Low-velocity intense source of atoms from a magneto-optical trap," *Phys. Rev. Lett.* **77**, 3331–4 (1996).

[95] K. Dieckmann, R. J. C. Spreeuw, M. Weidemüller and J. T. M. Walraven, "Two-dimensional magneto-optical trap as a source of slow atoms," *Phys. Rev. A* **58**, 3891–5 (1998).

[96] M. Zhu, C. W. Oates and J. L. Hall, "Continuous high-flux monovelocity atomic beam based on a broadband laser-cooling technique," *Phys. Rev. Lett.* **67**, 46–9 (1991).

[97] A. Noble and M. Kasevich, "UHV optical window seal to conflat knife edge," *Rev. Sci. Instrum.* **65**, 3042–3 (1994).

[98] P. Bouyer (1998). Personal communication.

[99] T. L. Gustavson, P. Bouyer and M. A. Kasevich, "A dual atomic beam matter-wave gyroscope," in *Methods for Ultrasensitive Detection*, edited by B. L. Fearey (1998), volume 3270 of *Proceedings of SPIE*, pp. 62–9.

[100] R. E. Drullinger, D. J. Glaze and D. B. Sullivan, "A recirculating oven for atomic beam frequency standards," in *Proc. 39th Annual Frequency Control Symposium* (IEEE, Piscataway NY, 1985), pp. 13–7.

[101] L. V. Hau and J. A. Golovchenko, "A new atomic beam source: The 'candlestick'," *Rev. Sci. Instrum.* **65**, 3746–50 (1994).

[102] R. D. Swenumson and U. Even, "Continuous flow reflux oven as the source of an effusive molecular Cs beam," *Rev. Sci. Instrum.* **52**, 559–61 (1981).

[103] P. D. Lett, W. D. Phillips, S. L. Rolston, C. E. Tanner, R. N. Watts and C. I. Westbrook, "Optical molasses," *J. Opt. Soc. Am. B* **6**, 2084–107 (1989).

[104] A. Aspect, N. Vansteenkiste, R. Kaiser, H. Haberland and M. Karrais, "Preparation of a pure intense beam of metastable helium by laser cooling," *Chem. Phys.* **145**, 307–15 (1990).

[105] N. Ramsey, *Molecular Beams* (Clarendon Press, Oxford, 1956).

[106] S. L. Gilbert and C. E. Wieman, "Atomic-beam measurement of parity nonconservation in cesium," *Phys. Rev. A* **34**, 792–803 (1986).

[107] D. Morris, "Shielded four-conductor magnetic field assembly," *Rev. Sci. Instrum.* **55**, 1483–5 (1984).

[108] J. T. Crow, "A method for producing highly uniform field characteristic with line currents," *Rev. Sci. Instrum.* **67**, 761–8 (1996).

[109] K. G. Libbrecht and J. L. Hall, "A low-noise high-speed diode-laser current controller," *Rev. Sci. Instrum.* **64**, 2133–5 (1993).

[110] O. Schmidt, K.-M. Knaak, R. Wynands and D. Meschede, "Cesium saturation spectroscopy revisited: How to reverse peaks and observe narrow resonances," *Appl. Phys. B* **59**, 167–78 (1994).

[111] L. Golberg, H. F. Taylor, J. F. Weller and D. M. Bloom, *Electron. Lett.* **19**, 491 (1983).

[112] S. Kobayashi and T. Kimura, "Injection locking in AlGaAs semiconductor laser," *IEEE J. Quantum Elect.* **17**, 681–8 (1981).

[113] J.-P. Bouyer, C. Bréant and P. Schanne, "Injection-locking mechanisms in semiconductor lasers," in *Proceedings of SPIE* (1992), volume 1837, pp. 324–35.

[114] K. Gibble (1998). Personal communication.

[115] P. Bouyer, T. L. Gustavson, K. G. Haritos and M. A. Kasevich, "Microwave signal generation with optical injection locking," *Opt. Lett.* **21**, 1502–4 (1996).

[116] P. Horowitz and W. Hill, *The Art of Electronics* (Cambridge Univ. Press, 1989), second edition.

[117] W. H. Press, S. A. Teukolsky, W. T. Vetterling and B. P. Flannery, *The Art of Scientific Computing* (Cambridge Univ. Press, 1992), second edition.

[118] D. W. Allan, N. Ashby and C. C. Hodge, "The science of timekeeping," Application Note 1289, Hewlett-Packard (1997).

[119] "Photodiode monitoring with op amps," Technical report, Burr-Brown, Tucson, AZ (1995).

[120] E. R. Cohen and B. N. Taylor, "The 1986 adjustment of the fundamental physical constants," *Rev. Mod. Phys.* **59**, 1121–48 (1987).

[121] H. Stolzenberg, S. Becker, G. Bollen *et al.*, "Accurate mass determination of short-lived isotopes by a tandem Penning-trap mass spectrometer," *Phys. Rev. Lett.* **65**, 3104–7 (1990).

[122] T. Hänsch *et al.* (1998). Personal communication to Achim Peters [28].

[123] J. Vanier and C. Audoin, *Quantum Physics of Atomic Frequency Standards*, volume 2 (A. Hilger, Bristol Philadelphia, 1989).